REPORT DOCUMENTATION PAGE

Form Approved
OMB No. 0704-0188

1. AGENCY USE ONLY *(Leave blank)*	2. REPORT DATE	3. REPORT TYPE AND DATES COVERED
	10 Sep 95	

4. TITLE AND SUBTITLE
The Role of Vertical Buoyancy Distributions In Simulated Low-Topped Supercells

5. FUNDING NUMBERS

6. AUTHOR(S)
Louis Edward Cantrell, Jr.

7. PERFORMING ORGANIZATION NAME(S) AND ADDRESS(ES)
AFIT Students Attending:

Tesas A&M University

8. PERFORMING ORGANIZATION REPORT NUMBER
95-114

9. SPONSORING/MONITORING AGENCY NAME(S) AND ADDRESS(ES)
DEPARTMENT OF THE AIR FORCE
AFIT/CI
2950 P STREET, BLDG 125
WRIGHT-PATTERSON AFB OH 45433-7765

10. SPONSORING/MONITORING AGENCY REPORT NUMBER

11. SUPPLEMENTARY NOTES

12a. DISTRIBUTION/AVAILABILITY STATEMENT
Approved for Public Release IAW AFR 190-1
Distribution Unlimited
BRIAN D. GAUTHIER, MSgt, USAF
Chief of Administration

12b. DISTRIBUTION CODE

13. ABSTRACT *(Maximum 200 words)*

14. SUBJECT TERMS	15. NUMBER OF PAGES 135
	16. PRICE CODE

17. SECURITY CLASSIFICATION OF REPORT	18. SECURITY CLASSIFICATION OF THIS PAGE	19. SECURITY CLASSIFICATION OF ABSTRACT	20. LIMITATION OF ABSTRACT

THE ROLE OF VERTICAL BUOYANCY DISTRIBUTIONS IN SIMULATED LOW-TOPPED SUPERCELLS

A Thesis

by

LOUIS EDWARD CANTRELL, JR.

Submitted to Texas A&M University
in partial fulfillment of the requirements
for the degree of

MASTER OF SCIENCE

Approved as to style and content by:

Louis J. Wicker
(Chair of Committee)

Benjamin S. Giese
(Member)

R. Lee Panetta
(Member)

Edward J. Zipser
(Head of Department)

August 1995

Major Subject: Meteorology

THE ROLE OF VERTICAL BUOYANCY DISTRIBUTIONS IN SIMULATED LOW-TOPPED SUPERCELLS

A Thesis

by

LOUIS EDWARD CANTRELL, JR.

Submitted to the Office of Graduate Studies of
Texas A&M University
in partial fulfillment of the requirements for the degree of

MASTER OF SCIENCE

August 1995

Major Subject: Meteorology

ABSTRACT

The Role of Vertical Buoyancy Distributions in Simulated Low-Topped Supercells.

(August 1995)

Louis Edward Cantrell, Jr., B.S., Texas A&M University

Chair of Advisory Committee: Dr. Louis J. Wicker

Tornadic potential in low-topped convection is difficult to forecast and to detect on radar. Observations of tornadic low-topped supercell environments allude to low-to-moderate CAPE and at least moderate low-level lapse rates in temperature. This study examines the role of low-level vertical buoyancy distributions in influencing supercell updraft intensity and persistence, and on mid-level and low-level mesocyclone development. The emphasis is to examine wind, temperature, and moisture profiles that are conducive to the development of low-topped supercells with tornadic potential. COMMAS, a non-hydrostatic 3-dimensional numerical cloud model, was used to simulate supercell development for nine idealized environments having a range of wind shears and total CAPE predictive of supercell type storms, and all having moderate vertical lapse rates in temperature. Supercell updraft forcing characteristics and low-level mesocyclone development in the models were similar for environments with adequate shear and buoyancy distributions in the low levels regardless of the environment's total CAPE. Model results suggest the vertical distribution of buoyancy over the sheared depth of the environment is a better indicator of an environment's potential to produce tornadic supercells than total CAPE.

ACKNOWLEDGEMENTS

I wish to express my gratitude to my thesis committee chairman, Dr. Louis Wicker, and to my associate committee members, Dr. Lee Panetta and Dr. Ben Giese. I greatly appreciate the opportunity to participate in VORTEX '94 at Dr. Wicker's invitation. My time storm chasing with Dr. Wicker will be forever the hallmark of my graduate experience at Texas A&M. I would also like to extend a special thanks to Matt Gilmore for his invaluable computing support and inspiration. For their insight, guidance, and genuine interest in my graduate program, my thanks goes to Dr.'s Ed Zipser, John Nielson-Gammon, James McGuirk, and Randy Lefever. Finally, I want to extend my warmest appreciation to my wife, Cynthia, and to my daughters, Jennifer and Diane. This would not have been possible without them. This work was supported in great part by the USAF Civilian Institution Graduate Program, and by Dr. Wicker in making available to me his research computer resources.

TABLE OF CONTENTS

Page

LIST OF TABLES

LIST OF FIGURES

FIGURE Page

1. INTRODUCTION

*Tornado-like events range in type and strength categorically from dust devils, gustnadoes (cf. Vickers 1990), landspouts (cf. Brady and Szoke 1988), waterspouts (cf. Golden 1978) and the tornado. A few studies have been conducted on tornadoes spawned from low-topped convection. They occur along or behind an occluded front that extends through a surface low (cf. Vickers 1990), beneath cold-core lows aloft (cf. Goetsch 1988, Cooley 1978), as a result of topography (cf. Hales 1993), land-falling hurricanes (cf. McCaul 1989), thermal moisture boundaries (cf. Maddox et al. 1980, Vescio et al. 1993), or forcing from other local maxima of convergence such as drylines (cf. Burgess and Davies-Jones 1979).

Some of these studies indicate that the convection was supercellular in nature. Typically, a supercell is an isolated convective cell with a steady updraft lasting on the order of several tens of minutes to hours and having strong vertical rotation through a significant depth of the storm. Supercells generally propagate right of the mean wind vector and have weak echo regions in their radar observed rain reflectivity fields. Supercells can produce locally heavy rain, large hail, damaging winds and tornadoes (Browning 1964, Wallace and Hobbs 1977). Previous research on the dynamics of tornadic supercells has concentrated on the environmental characteristics associated with deep Great Plains supercells. However, little research has focused on the dynamics associated with severe *low-topped* supercells which makes forecasting these storms difficult. This study seeks to examine the dynamics that encourages low-topped convection to acquire supercell characteristics, such as a persistent updraft and deep vertical rotation, and ultimately tornadic potential.

---

* Style and format follows the *Monthly Weather Review*

a. Observations of low-topped supercells

Low-topped supercells are somewhat unusual, but not uncommon, as noted from the many reports of these storms in the literature. Davies (1993a) defines low-topped supercells as supercells with storm tops less than 30,000 ft. For the purpose of this study, this height has been adopted as the upper height limit for defining low-topped supercells. Large convective available potential energies (CAPE) associated with tornadic supercells having greater vertical extent are not always found in low-topped supercells. CAPE (Moncrieff and Green 1972) is defined as the vertically integrated positive buoyancy of a parcel rising from the surface. The theoretical maximum updraft strength is related to CAPE by the following expression:

$$w_{\max} \approx \sqrt{2 \bullet CAPE} \tag{1}$$

Low-topped supercells also have lower equilibrium levels (EL). The EL is the maximum height positive buoyant energy is available to a parcel rising from the surface. According to parcel theory, a buoyant parcel reaches its maximum vertical velocity at the EL. McCaul's (1989) observations of tornadoes from low CAPE, highly sheared hurricane environments support Droegemeier et al.'s (1993) conclusion that large buoyant energy is not always necessary for developing severe thunderstorms. Low buoyancy storms can produce significant damage and can be difficult to forecast (Moller and Ely 1985); therefore, low buoyancy environments need to be carefully considered as potential severe weather producers.

Some of these storm tops are far below the tropopause and produce no cirrus cloud shield. These storms may also exhibit lower amounts of electrical activity. Cases of F1 and F2 tornadoes from low-topped supercells with no lightning or thunder and with CAPE's less than 1000 J kg^{-1} have been documented by Davies (1993a). These storms have

environments characterized by low-to-moderate CAPE, a low EL, and strong low-level inflow and helicity.

Another problem is that some cases have no observable mid-level mesocyclone. A mesocyclone is a mesoscale region (5-10 km across) with locally high vertical vorticity (Ray 1976). Forecasters using radar normally rely on detecting mid-level mesocyclones generated by the vertically rotating wind field of supercells to identify the potential for tornadoes (Burgess 1976). Detecting the mesocyclone on radar can provide forecasters with warning lead times sometimes greater than a half hour. Many tornadic low-topped supercell (TLTS) storms, however, do not have a clearly identifiable mesocyclone observed on radar. This may be due to the storm being under-sampled by the radar beam, or not having sufficient height to be observed by distant radar. Burgess and Davies-Jones (1979) observed three TLTS storms in Texas with low EL's, no indication of mesocyclone development, low radar reflectivities, and with tops overshooting the EL by as much as 4 km. Kennedy et al. (1990) observed a TLTS storm in Illinois that had no radar reflectivity above 6 km, and winds veering more than 100° from the surface to 500 mb. Other recent observations of ill-forecasted tornadic low-topped supercells have also appeared in the literature (cf. Guerrero and Reed 1993, Murphy and Woods 1992, Thompson et al. 1994, Vescio et al. 1993, and Vickers 1990).

The small appearance of these storms, virtually no lightning, no clear radar signatures of tornadic potential, and only low-to-moderate values of CAPE appear typical for tornadic events associated with low-topped supercells. A preliminary overview of environmental data from these storms suggests that factors other than CAPE could play a role in defining the buoyancy and wind shear conditions predictive of an environment's potential to produce TLTS storms. Additionally, some observations of the nearby environments of these storms indicate low-topped supercells may have small CAPE's with vertical distributions of buoyancy heavily weighted in the lower layers of the troposphere. As an example, the thermodynamic profile in Fig. 1 was representative of the nearby environment of a TLTS

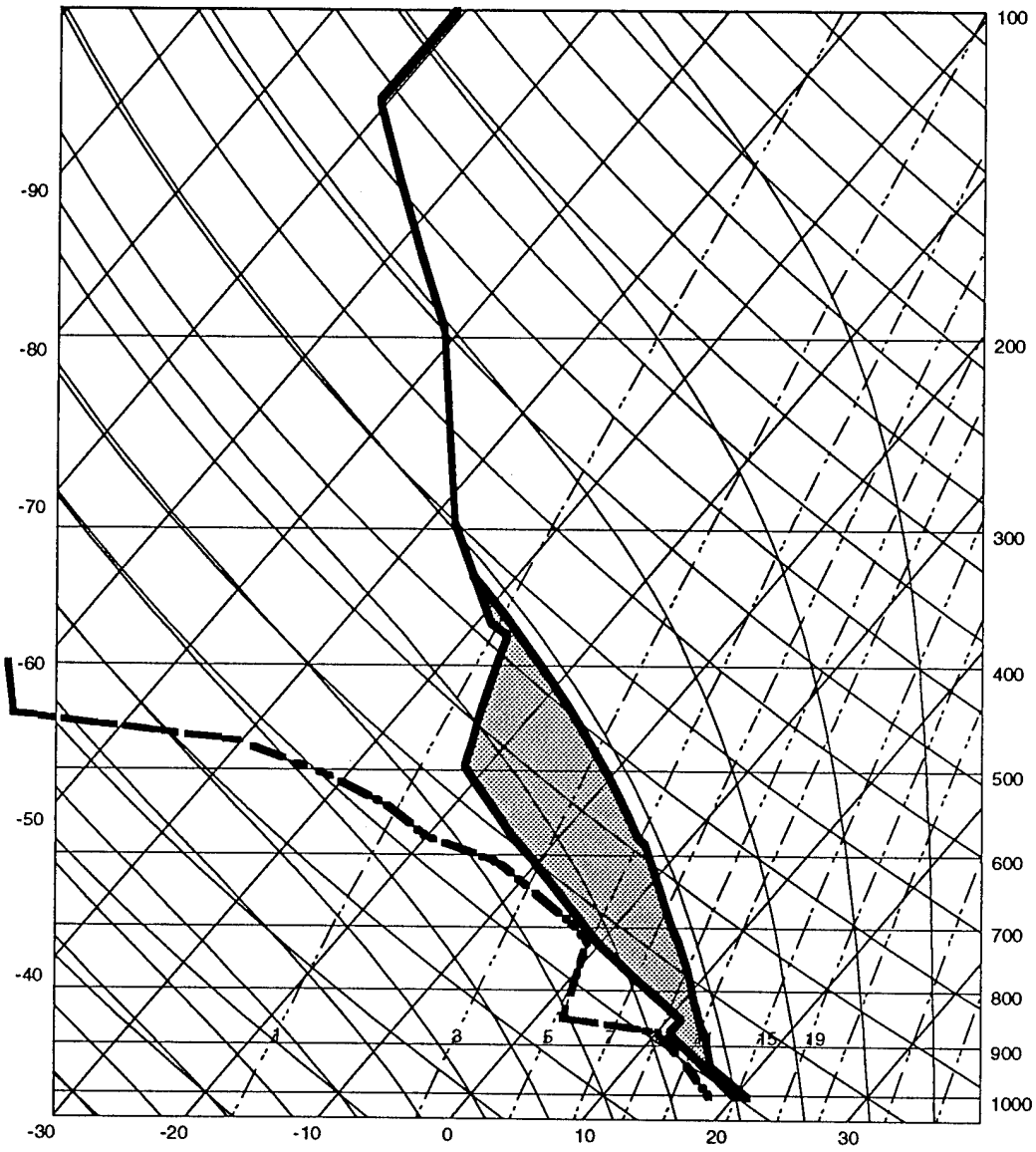

FIG. 1. Composite skew T diagram constructed from the nearby soundings of a tornadic low-topped supercell environment in Kansas, 1991. Horizontal lines are isobars. Solid lines extending from lower left to upper right of diagram are isotherms. Lines curving upward are dry adiabats, and lines curving downward are saturated adiabats. Chained lines are water vapor mixing ratios. Thick solid line represents ambient temperature profile and thick dashed lines represent ambient dew point temperature profile. This sounding has a CAPE of < 1000 J kg^{-1}, and an EL of only 24,000 ft. Shaded area represents CAPE. (Adapted from Davies 1993a)

observed in Kansas (Davies 1993a). This sounding has a CAPE of less than 1000 J kg^{-1} and an EL of only 24,000 ft.

A few observational studies have been published that call attention to tornadic low-topped convection so that methods can be developed to better detect and forecast them. Appendix B outlines some observations of ill-forecasted tornadic low-topped supercells. Some observations of tornadic non-supercellular low-topped convection are also contained in appendix B.

b. Objectives

An examination of the case literature above and in appendix B indicates that several aspects of atypical supercell environments should be studied in order to improve our ability to track and forecast the wide variety of supercell storms. Much of the current understanding about supercells has been derived through numerical cloud modeling, especially when numerical cloud modeling has been combined with observed supercells. In order to study the parameters which may be associated with TLTS's, this study will use a numerical cloud model to understand their behavior.

Two research objectives form the basis of this study. The first objective is to determine if these storms are fundamentally different than their deeper classic Great Plains "cousins". Supercells possess specific updraft and mid-level mesocyclone characteristics. Tornadic supercells possess specific low-level mesocyclone characteristics. We seek to determine if these same characteristics occur in low-topped supercells. The second objective is to examine whether the vertical distribution of buoyancy may be an important factor in the development of supercells. It is important to learn if the buoyancy distribution in the lowest 5 km has more meaning in defining supercell potential than total CAPE. In these respects, this study parallels the study of land-falling hurricane environments by McCaul and Weisman (1995). Collectively, studies like this may clarify the region of parameter

space (with dimensions in shear magnitude, and vertical buoyancy distribution) where tornadoes are likely.

Ultimately, simulations of low-topped supercells may reveal unique features of these severe storms that can be offered to forecasters dealing with them. Modifications to environmental parameters (such as the Bulk Richardson Number) that can take into account the vertical distribution of buoyancy may also help forecasters identify severe weather potential even in low-topped thunderstorms.

c. Review of supercell development

Excellent conceptual models of tornadic supercells and their dynamics are presented by Klemp (1987), Klemp and Rotunno (1983), and Rotunno (1993). It has been hypothesized that the spectrum of storm types ranging from the short-lived single cell storm through the long-lived single cell storm (supercell) to the discretely propagating multicell storm may be strongly dependent on two readily observable parameters defining the environment in which the storms develop. These two parameters are CAPE and vertical wind shear. Weisman and Klemp (1982) tested this hypothesis using a 3-dimensional numerical cloud model developed by Klemp and Wilhelmson (1978). They found supercells occur in moderate-to-high shear environments. A comparison of their model results with observed environments and storm behaviors showed that the ratio of CAPE to vertical wind shear was a good discriminator between various storm types. Summarized next are some of the readily observed supercell characteristics that may be affected by the variation of shear and buoyancy.

1) UPDRAFT PERSISTENCE AND INTENSITY

Supercell updrafts have been observed to initially propagate with the 0-6 km density weighted mean wind. After initial development, they deviate from this direction, moving to the left or right of the mean wind. Rotunno and Klemp (1982) found that deviate propagation was due to the horizontal gradients of pressure dynamically (shear) induced across the updraft (see appendix D). Updrafts within a sheared environment produce a mid-level cyclonic/anti-cyclonic vertical vortex couplet on the right and left flanks of the updraft respectively through tilting of the environmental vortex lines. A cyclostrophicly induced low pressure occurs in the center of each vortex. This produces a non-hydrostatic upward-directed vertical pressure gradient below each mid-level vortex. The vertical pressure gradients act to split the updraft and cause it to diverge to the left and right of the mean wind vector. A conceptual model of this splitting process devised by Rotunno (1981) is given in Fig. 2. The updraft deviating from the shear vector results in a storm-relative wind profile that rotates with height (Fig. 3). The direction of rotation varies with the direction the updraft deviates from the environment's mean wind vector.

Rotunno and Klemp (1982) additionally proposed that these vertical pressure gradients are dynamically favorable to one region over another in a rotating wind field. The varying orientation of horizontal pressure gradients with height also produces non-hydrostatic vertical pressure gradients. Qualitatively, a pressure perturbation high will occur aloft and upshear of the updraft, and a pressure perturbation low will occur downshear and aloft of the updraft (Fig. 4). For example, if the storm-relative horizontal wind rotates counter-clockwise with height (veering), the two mechanisms that produce vertical pressure gradients act to encourage updraft development beneath the cyclonic vortex on the right flank of the updraft while discouraging updraft development beneath the anti-cyclonic vortex on the left flank of the updraft. If the shear vector veers with height, an upward-directed vertical pressure gradient is located upshear of the updraft at low levels and the

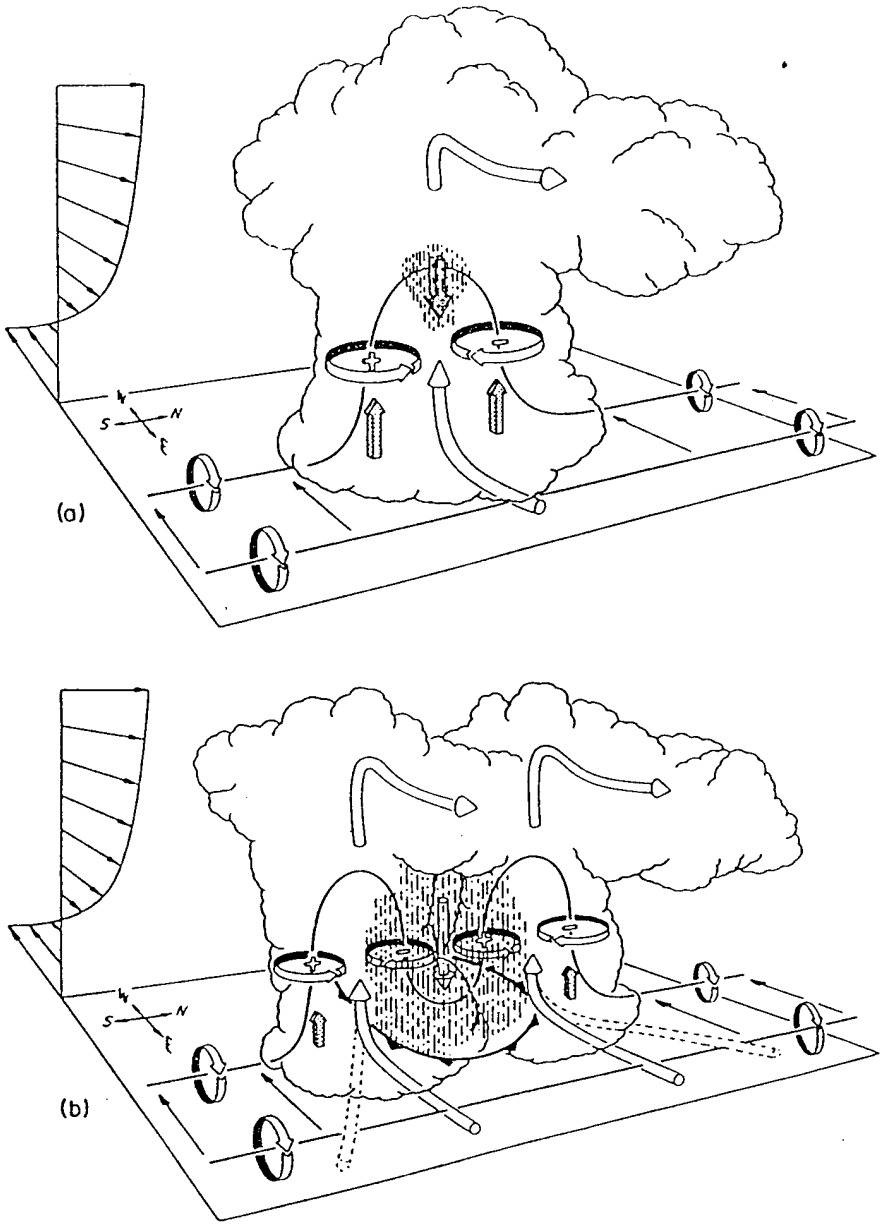

FIG. 2. Schematic depicting how a typical vortex tube contained within (westerly) environmental shear is deformed as it interacts with a convective cell (viewed from the southeast). Cylindrical arrows show the direction of cloud-relative airflow, and heavy solid lines represent the forcing influences that promote new updraft and downdraft growth. Vertical dashed lines denote regions of precipitation. (a) Initial stage: Vortex tube loops into the vertical as it is swept into the updraft. (b) Splitting stage: Downdraft forming between the splitting updraft cells tilts the vortex tubes downward, producing two vortex pairs. The barbed line at the surface marks the boundary of the cold air spreading out beneath the storm. (Reprinted from Rotunno 1981)

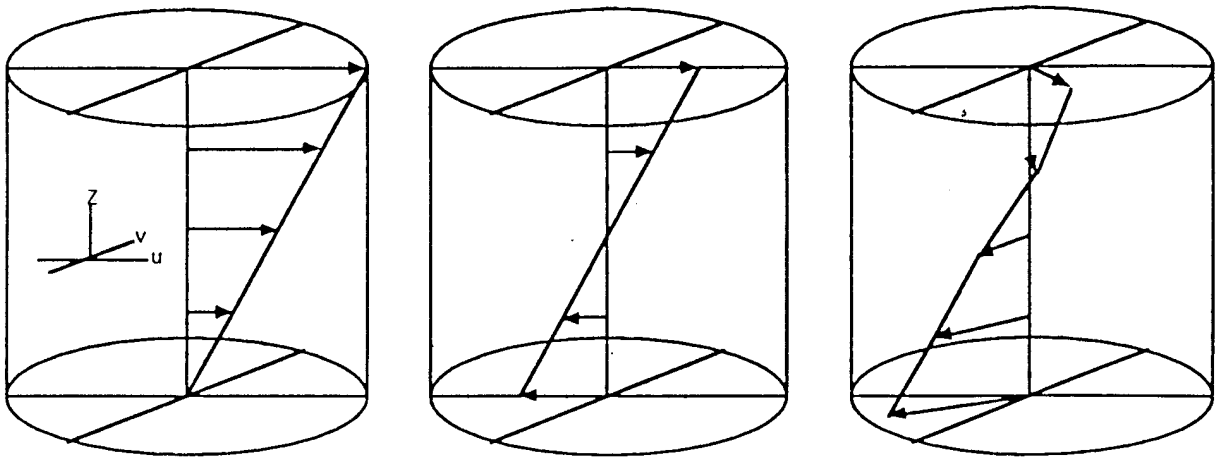

FIG. 3. Schematic of environmental and storm-relative wind profiles. Arrows represent horizontal wind speeds for a given height. The left profile is an environmental, linear, unidirectional wind distribution such as that used in these simulations. The middle profile is a storm-relative wind distribution for a storm initially propagating with the mean wind. The right profile is a storm-relative wind distribution for a storm propagating to the left of the mean wind. A storm propagating to the right would have a mirror image profile that rotates in the opposite direction with height. Deviate propagation in a unidirectional wind profile environment results in a storm relative wind profile that rotates with height.

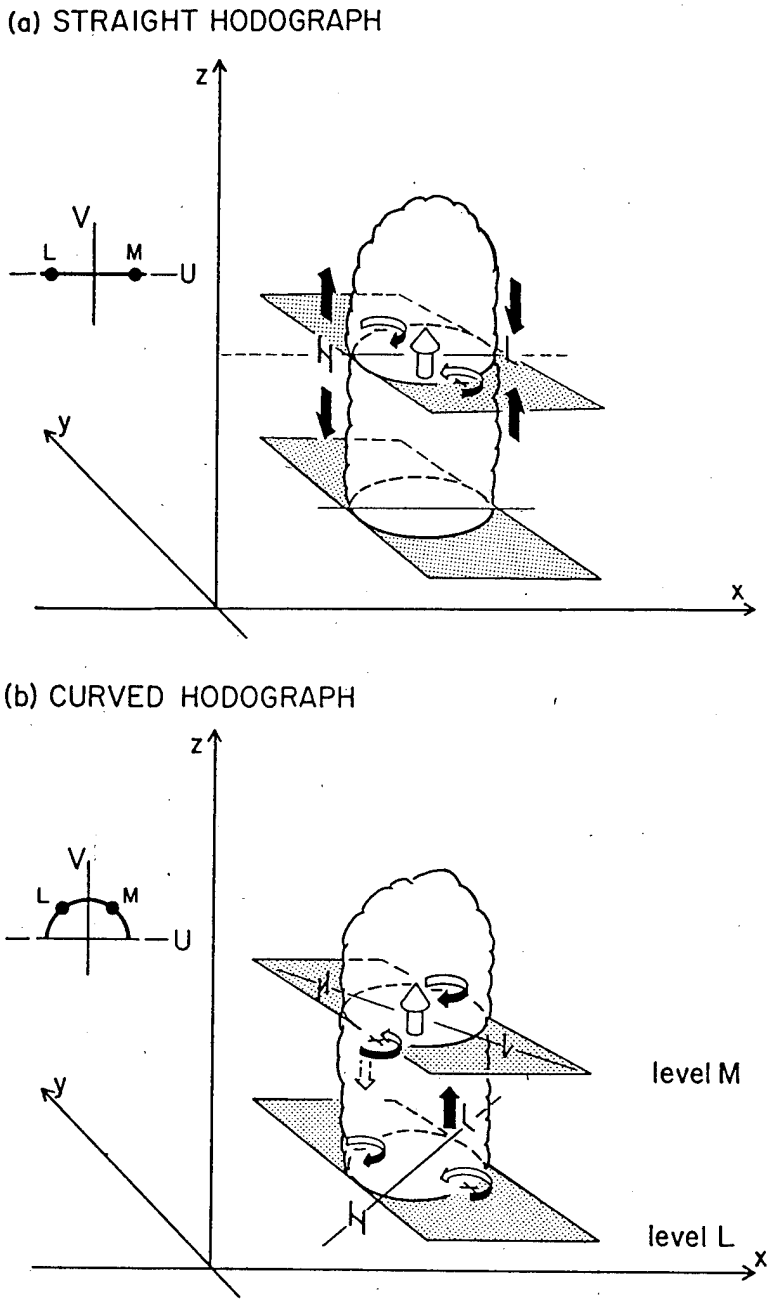

FIG. 4. Schematic which illustrates the behavior of pressure and vorticity for (a) a case where the wind shear vector does not change with height and (b) a case where the wind shear vector veers with height. The corresponding hodographs for environmental flow at low (L) to mid (M) levels are inset to the left. Horizontal pressure gradients parallel to the shear vector are labeled at each level along the preferred locations of positive (+) and negative (-) vorticity. The orientations of the resulting vertical pressure gradient forces between low and mid-levels are indicated by the black arrows. (Reprinted from Rotunno and Klemp 1982)

storm propagates to the right. The most commonly observed supercell producing environments have low-level wind profiles that veer; therefore, the most commonly observed supercells are those that propagate to the right of the mean wind vector.

Updrafts grow more vigorously in the absence of deep ambient shear (Droegemeier et al. 1993). This is due to the increased entrainment caused by the shear. Entrainment is the mixing of environmental air into an organized updraft (Huschke 1959). For convection to become supercellular, storm-relative low-level winds must be sufficiently sheared to inhibit the rapid propagation of the gust front created from the evaporatively cooled downdraft air. In strong shear environments, storm-relative low-level inflow prevents outflow air from moving ahead of the storm. This keeps the mid-level updraft from being cut off by the outflow gust front. If the gust front propagates too rapidly, it becomes decoupled from the mid-level updraft and the storm gusts out or becomes a discretely propagating multicell system (Wilhelmson and Klemp 1978). Droegemeier et al. (1993) observed that storm-relative inflow of at least 10 m s^{-1} in the 0-3 km layer is a necessary condition for supercell development. They conclude that the storm-relative wind profile plays a greater role in maintaining the updraft at the low levels than buoyancy does.

2) VERTICAL ROTATION

Supercells have strong vertical rotation through a significant depth of the storm. In supercells, the development of the mid-level mesocyclone is a result of the buoyancy driven updraft's interaction with a vertically sheared environment. The development of strong vertical rotation in the mid-level mesocyclone results primarily from two sources. First, the gradient of the vertical wind between the updraft and downdraft tilts the ambient shear vorticity into the vertical. Second, because buoyant accelerations induce a vertical gradient in vertical velocity within the updraft, vertical vorticity is further increased by stretching.

Davies (1993b) noted that updrafts with strong upward acceleration and stretching are associated with environments exhibiting steep lapse rates. Doswell et al. (1990) suggested that steep lapse rates contribute significantly to the development of severe thunderstorms in the Great Plains. Thus, the production of low to mid-level vertical vorticity in low-topped convection may be enhanced for environments with large low-level buoyancy. The strength of the vertical vorticity tendency for the mid-levels is proportional to the vertical and horizontal gradients of vertical velocity (Klemp 1987). It is hypothesized here that low-topped supercell storms can have sufficiently large updraft velocities to produce strong mid-level mesocyclones. This means environments with moderate lapse rates in temperature at low levels and with low EL heights may produce strong mid-level mesocyclones given sufficient shear.

Tilting and stretching baroclinically generated horizontal vorticity within the surface cold pool contributes more to the production of vertical vorticity in the low-level mesocyclone than tilting and stretching ambient shear vorticity (Lemon and Doswell 1979). Low-level mesocyclones are more sensitive to the horizontal gradients of buoyancy and to the low-level wind field than to the depth of the storm or to the maximum updraft magnitude attained near the EL. This implies that even storms of diminutive scale can produce tornadoes given a sufficiently strong cold pool beneath the rainy downdraft and sufficient tilting by the horizontal gradient of the vertical wind between the updraft and downdraft.

McCaul (1989) notes that the comparative vertical distribution of shear and buoyancy may be important indicators of severe weather potential particularly with the greatest enhancement occurring when an entire layer of vertically sheared flow is also positively buoyant. He also suggests that "*...a systematic study of the effects on storm evolution of variations in the heights of maximum buoyancy and maximum wind in the starting environment would be of value in helping establish the limiting conditions for supercell development.*"

The following section describes nine numerical simulations designed to test the effect of varying shear strength and total buoyancy on low-topped supercell development. The results of those simulations are presented in section three. In section four, the model data are interrogated to determine what factors contribute to the persistence of the updraft and to the development of strong low-level rotation in the simulated low-topped supercells.

2. METHODOLOGY

Using the 3-dimensional numerical cloud model developed by Klemp and Wilhelmson (1978), Weisman and Klemp (1982, 1984) modeled isolated convective storms with various thermodynamic and wind profiles in order to better understand how environmental vertical wind shear and buoyancy influence the structure and evolution of convection. To control the thermodynamic and wind profiles used in their experiments, Weisman and Klemp developed analytic functions for temperature, relative humidity, and wind speed that produce environments qualitative of those observed near convection. This study will modify these analytic functions to create environments resembling those observed near TLTS storms.

a. Idealized environments

To carry out these objectives from a modeling standpoint, nine idealized environments are specifically designed to span the parameter space of total CAPE's and wind shears predictive of supercell type storms. The nine environments are constructed from combinations of three different temperature/dew point profiles and three different wind profiles. Six of the idealized environments are expected to produce low-topped convection because of their EL heights. The temperature and moisture profiles are modeled using Weisman and Klemp's (1982) analytic functions with slight modifications to the equations to adjust the EL without varying the vertically integrated buoyancy computed below a given pressure level. The thermodynamic profiles are designed so that the updraft parcel's equivalent potential temperature is invariant among the cases. Maintaining a constant equivalent potential temperature constrains the latent heat released during the surface parcel's ascent and condensation to be consistent among the cases. The profiles of relative humidity are also identical throughout the entire depth of the environments. See appendix

C for a detailed description of the analytic functions used. The wind and thermodynamic profiles tested are idealized and used to isolate the general effects of the vertical distribution of buoyancy on storm morphology and are not used to reproduce a particular observed storm.

The three thermodynamic profiles used are given in Figs. 5a-c. Figure 5a is a skew-T/log-p diagram of the highest total CAPE and EL cases. This sounding produces a moderate low-level vertical lapse rate, has a level of free convection (LFC) at about 1500 meters, an EL at 12 km, and a total CAPE of 2100 J kg^{-1}. The 12 km EL sounding is nearly identical to the 14 g kg^{-1} surface water vapor mixing ratio case used by Weisman and Klemp in their 1982 study. The second thermodynamic profile, shown in Fig. 5b, is designed to be identical to the previous sounding below 500 mb. The EL height, however, is forced to be 8 km. The total CAPE is about 1040 J kg^{-1}. The third sounding (Fig. 5c) is also identical to the other two soundings but only below 600 mb. The EL here is constrained to be 7 km. The total CAPE is about 690 J kg^{-1}; less than one third of the 12 km EL sounding. The idealized 7 km EL sounding is similar in many respects to the nearby environment of a TLTS reported by Davies (1993a, see Fig. 1). The LFC is constant at 1500 m for all three soundings.

In order to model supercells, sufficient vertical wind shear must exist. Following Wilhelmson and Klemp (1978) and Weisman and Klemp (1982), shear magnitudes of 0.004 s^{-1}, 0.006 s^{-1}, and 0.008 s^{-1} were chosen to cover the range of shears documented by Marwitz (1972) which were found in observed supercell environments. Droegemeier et al. (1993) concluded that storm-relative inflow of at least 10 m s^{-1} in the 0-3 km layer is a necessary condition for supercell storms. The tests must therefore have a low-level wind profile with sufficient shear to encourage strong inflow at low levels. The lower limit of shear considered (0.004 s^{-1}) is the minimum necessary to meet this requirement. The shear depth is selected to be 6 km as in previous modeling studies (cf. Wilhelmson and Klemp 1978, and Weisman and Klemp 1982). The three wind profiles used have unidirectional

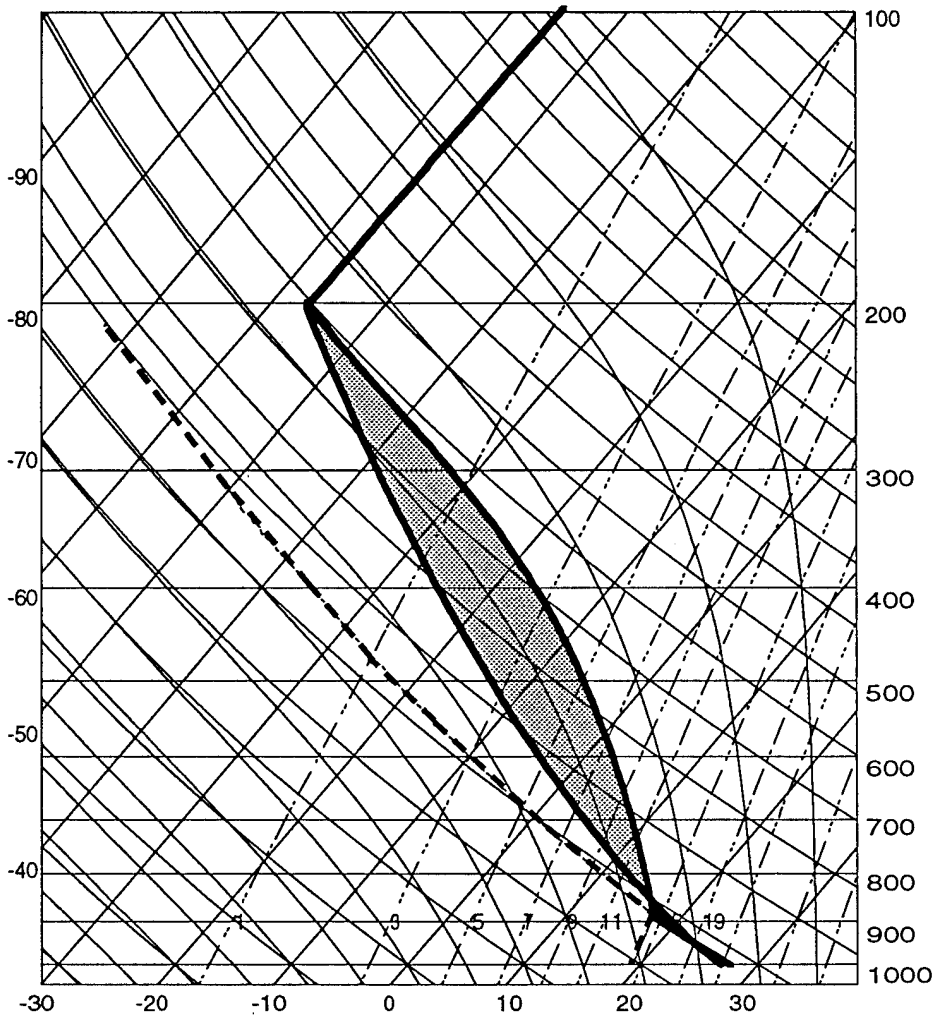

FIG. 5a. Skew T diagram depicting the idealized 12 km EL sounding with a CAPE (shaded region) of 2100 J kg^{-1}. The level of free convection (LFC, located at the base of the shaded region) is at 1500 m for all three soundings shown in Figs. 5a-c. All three soundings also have the same convective inhibition (represented by the area bounded by the temperature and dew point temperature lines below the LFC), surface temperature of 300 K and surface relative humidity of 85%.

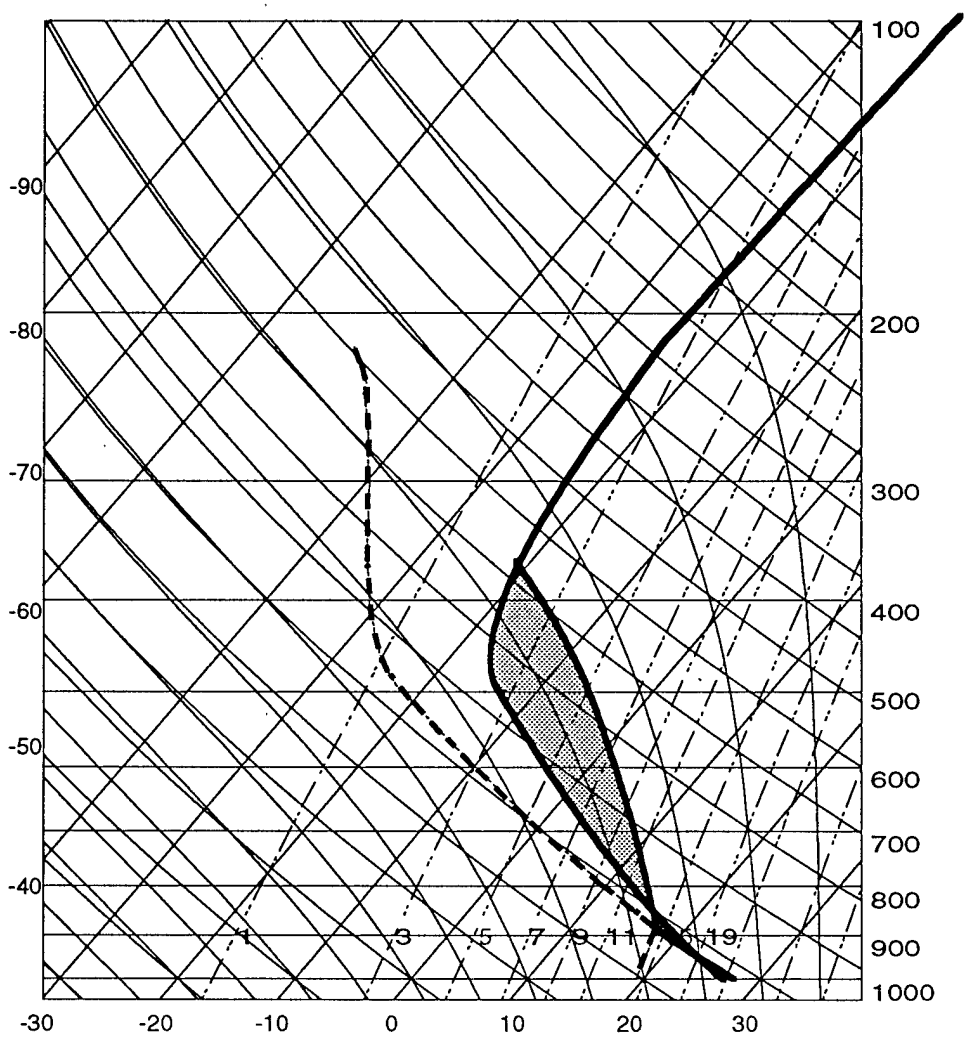

FIG. 5b. Same as FIG. 5a except skew T diagram depicts the idealized 08 km EL sounding with a CAPE of 1040 J kg^{-1}.

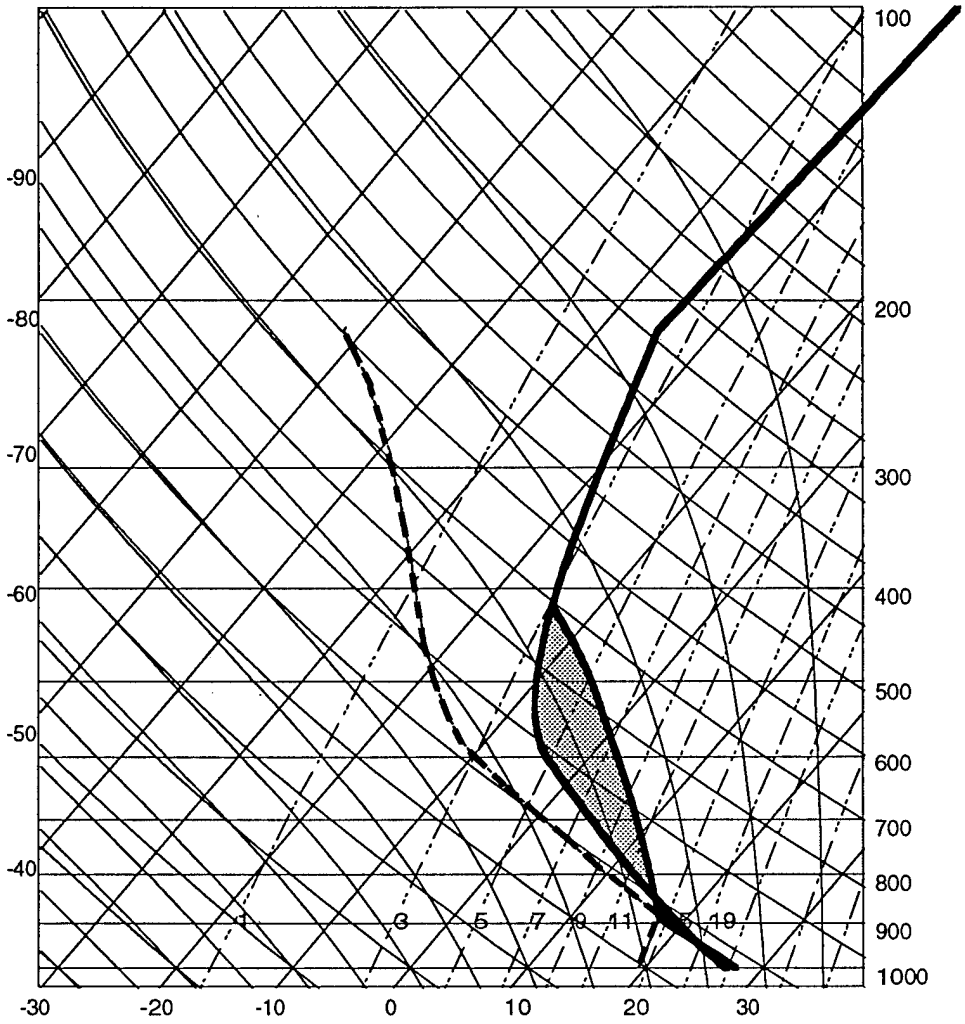

FIG. 5c. Same as FIG. 5a except skew T diagram depicts the idealized 07 km EL sounding with a CAPE of 690 J kg^{-1}.

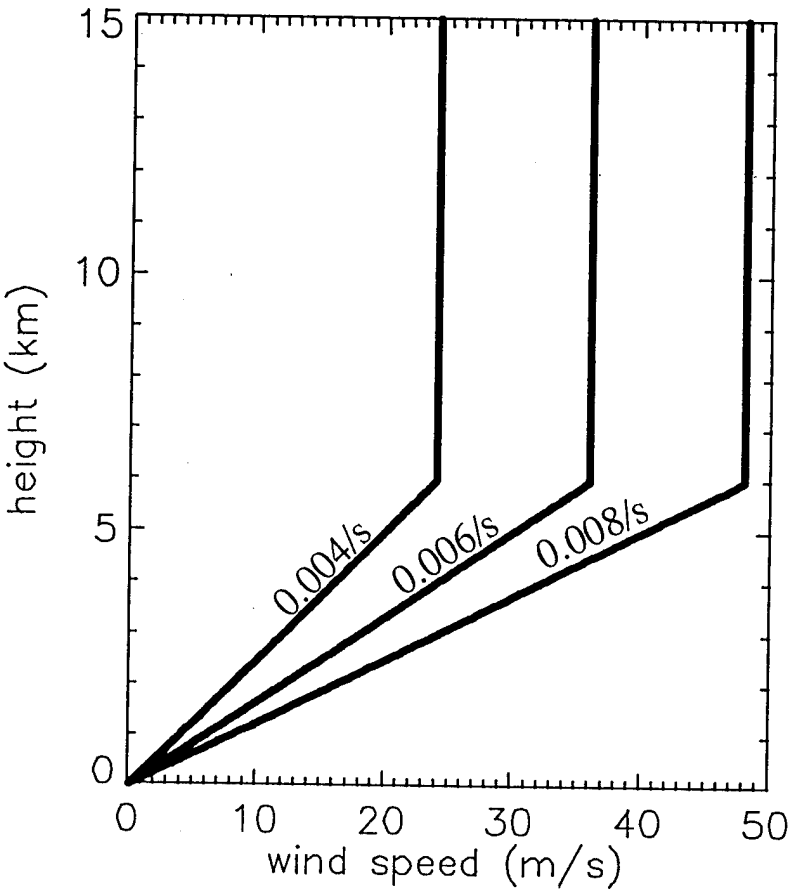

FIG. 6. Idealized wind profiles used in the model simulations. Winds are west-to-east unidirectional and have constant shear magnitudes of 0.004 s^{-1}, 0.006 s^{-1}, and 0.008 s^{-1} over the 0-6 km layer. Winds are constant above 6 km.

west to east flow with constant vertical shear from the surface the 6 km. This is to permit various magnitudes of wind shear while maintaining the depth of the sheared layer. Maximum environmental wind speeds are 24 m s^{-1}, 36 m s^{-1}, and 48 m s^{-1}. Winds above 6 km are constant. The wind profiles in Fig. 6 are capable of generating all of the observed features of supercell storms while simplifying the analysis.

One measure of an environment's potential to produce supercell storms is the Bulk Richardson Number (BRN) as formulated by Weisman and Klemp (1982). The BRN is the ratio of the storm's total CAPE to its estimated inflow kinetic energy, and is used as a measure of the "steadiness" of convection. Generally, environments with BRN values less than 50 have the potential to produce supercells. BRN values greater than 35 have the potential to produce multicell type convection (see Fig 7). While there is some overlap in the range of values expected to produce supercells, it is never-the-less considered a useful tool for forecasting the storm type an environment is capable of producing. Table 1 gives the BRN calculated for each of the nine storms. The environments used here had BRN's ranging from 4 to 47 which are indicative of an environment's potential to produce supercell storms.

TABLE 1. Bulk Richardson Numbers computed for the nine idealized soundings used in the model simulations.

	0.004 s^{-1}	0.006 s^{-1}	0.008 s^{-1}
12 km EL	47.1	21.0	11.8
08 km EL	23.3	10.4	5.8
07 km EL	15.6	7.0	3.9

b. Cloud model

The primary tool used to conduct the individual tests was the COllaborative Model for Multiscale Atmospheric Simulation (COMMAS) cloud model (Wicker and Wilhelmson 1993). COMMAS is based upon the design of the non-hydrostatic 3-d numerical cloud

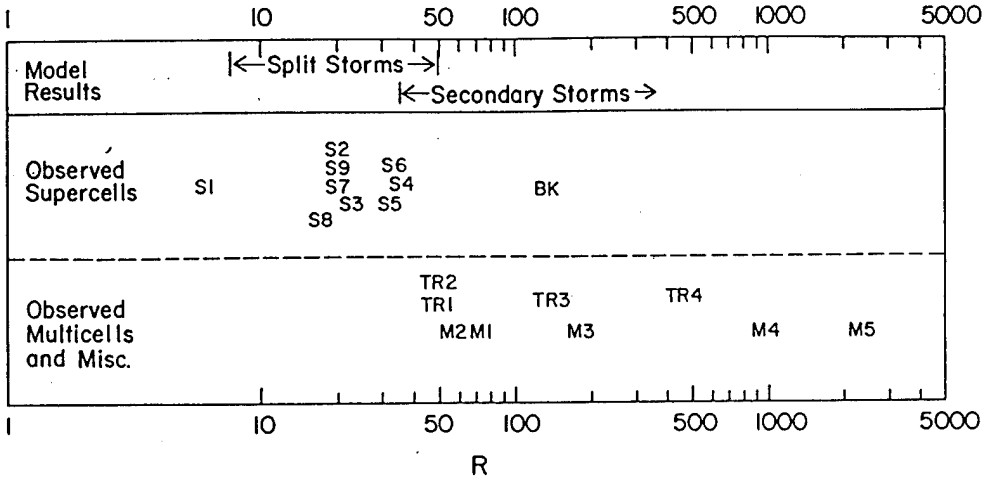

FIG. 7. Bulk Richardson Numbers calculated for documented storms tabulated by Weisman and Klemp (1982) (See their Table 1). "S*" represents observed supercell type storms, "M*" represents observed multi-cell storm type, "TR*" represents tropical cloud clusters and squall lines, and BK represents an unknown storm type. (Adapted from Weisman and Klemp 1982)

model of Klemp and Wilhelmson (1978). The model solves the fully compressible Reynolds averaged Navier-Stokes equations of motion. The primary variables solved are the three Cartesian wind components u, v, w, non-hydrostatic pressure perturbation π, potential temperature θ, and the mixing ratios of water vapor q_v, cloud water q_c, and rainwater q_r. Subgrid turbulent mixing K_m is parameterized using a turbulence energy equation in order to include subgrid scale motion effects. To achieve numerical efficiency, a smaller time step used to treat sound wave modes in the compressible equations separately from other processes that can be computed using a larger time step.

Because the tests will be conducted to differentiate the potential for severe storm development from among a variety of environmental conditions, a moderately high grid resolution is used in order to resolve the smaller scale features associated with TLTS's. The model domain is 60 x 60 x 15 km with a horizontal grid resolution of 750 m. Vertical grid stretching is used to resolve the low-level storm environment at a high resolution while maintaining numerical efficiency. The lowest grid resolution is 250 m, which is stretched to 692 m at the top of the domain over 35 grid points.

The cloud model includes parameterizations for water microphysics but does not include ice microphysics. Water processes such as condensation to cloud droplets and accretion to rain droplets with an appropriate distribution in size are parameterized using the method developed by Kessler (1969). Because the duration of the model simulations is small compared to planetary time scales, Coriolis force was also omitted from the model calculations. The model has rigid, free-slip surface and top boundary conditions, and open boundaries at the lateral faces of the domain. Vertical gravity waves are damped in the highest quarter of the domain. A detailed list of model parameters is contained in Table 2.

Each idealized wind and buoyancy profile is used to initialize the COMMAS model. Initiation for the tests is similar to that conducted by Klemp and Wilhelmson (1978) and others. Convection is initiated with a symmetric thermal perturbation of +4° C in

hydrostatic equilibrium within an otherwise horizontally homogeneous environment. Initially the vertical wind and non-hydrostatic pressure perturbation are zero in the domain.

All simulations are carried out to at least 2.5 hours. After one hour of simulation time, all model fields are saved at 5 minute intervals for the purpose of analysis. The model domain is set to move in the direction of the rightward propagating maximum updraft in order to keep the primary region of convection near the center of the domain. Animations of the primary data fields are also composed at the surface, 1 km, 5 km, and 8 km AGL with a temporal resolution of 2 minutes beginning at the 1 hour point in each simulation.

TABLE 2. COMMAS model input parameters.

STRETCH FAC = 1.030978

No. OF INT = 34

HEIGHT OF MODEL = 15399.98

TIME = 0.0

GRID = 0

NX = 80 NY = 80 NZ = 35

EAST-WEST GRID POSITIONS: 0.00 60000.00

NORTH-SOUTH GRID POSITIONS: 0.00 60000.00

TIME STEP: 5.0 # OF SMALL TIME STEPS: 4

DX: 750.00 DY: 750.00 DZ: 440. DZBOT: 250.

X BOUNDARY CONDITION: OPEN

Y BOUNDARY CONDITION: OPEN

Z BOUNDARY CONDITION: FREE-SLIP

LATERAL BOUNDARY CONDITION FOR SCALAR INFLOW=0 (KW BC)

SCALAR ADVECTION SCHEME IS MODIFIED SWEBY

MIXING SCHEME IS DIAGNOSTIC KM

MIXING LENGTH COMPUTED USING (GRID VOL)**1/3

MAXIMUM SQRT(TKE) = 5. LMAX = 300.

NON-DIMENSIONAL COEFF (Cm) = 0.21 PRANDTL NUMBER = 1.00

UM = 15.00 VM = 0.00

SURFACE PRESSURE = 1000.

SOUND SPEED MAX = 300. CORIOLIS VALUE = 0.0000000E+00

FILTER COEFF: 2ND ORDER VERTICAL = 0.0025

4TH ORDER HORIZONTAL = 0.0500

OUTFLOW GRAVITY WAVE SPEED = 40.

RAYLEIGH DAMPING SPONGE: INITIAL HEIGHT = 12000.

MAG = 0.1000000E-02

VERTICAL SOUND WAVE IMPLICIT COEFFICIENT = 0.10

ASSELIN TIME FILTER VALUE = 0.10

DIVERGENCE DAMPER COEFFICIENT = 0.05

CDM = 0.1000000E-02 CDH = 0.3000000E-02 CDQ = 0.2100000E-02

INITIAL CONDITIONS FOR MODEL RUN

BBLE #: 1 XPOS: 30000.0 YPOS: 30000.0 ZPOS: 1500.0

XRAD: 10000.0 YRAD: 10000.0 ZRAD: 1500.0

3. RESULTS

a. General behavior

The nine idealized environments are used to evaluate buoyancy and shear interactions in the simulated supercell storms. As mentioned earlier, the parameter space evaluated is simply a 2-dimensional matrix with variations in total CAPE and in constant shear magnitude over the lowest 6 km. CAPE's tested are 2100 J kg^{-1}, 1040 J kg^{-1}, and 690 J kg^{-1}. Shear values used are 0.008 s^{-1}, 0.006 s^{-1}, and 0.004 s^{-1}. The nine storms in this experiment all evolve similarly to the unidirectional shear experiments of Wilhelmson and Klemp (1978), and Weisman and Klemp (1982). The storms split into mirror image leftward and rightward moving storms. The split storms developed a quasi-persistent updraft and strong vertical circulation over a significant depth relative to the heights of the EL's. To obtain information relevant to the most commonly observed supercell storms, the analysis herein will follow the rightward propagating storm.

At 30 minutes, the rain water mixing ratio fields show nearly symmetric splitting of the main rain region which is elongated in the direction of the environmental shear vector (see Fig. 8). Updrafts of equal intensity also form on the north and south flanks of the original convective cell. The magnitudes of the surface rain mixing ratios and updrafts are similar among the nine cases as well. The distances separating the updraft maxima across the precipitation region are also roughly equal.

At 60 minutes, the region of precipitation is completely split for most cases and the updraft has reached its maximum magnitude (see Fig. 9). The primary difference noted is the extent to which the precipitation region extends in front of an axis drawn between the two flanking updraft maxima. As the EL increases, precipitation from higher levels within the storm takes longer to fall and is therefore transported further downwind of the storm's updraft. In a similar manner, simulations having stronger environmental shear have

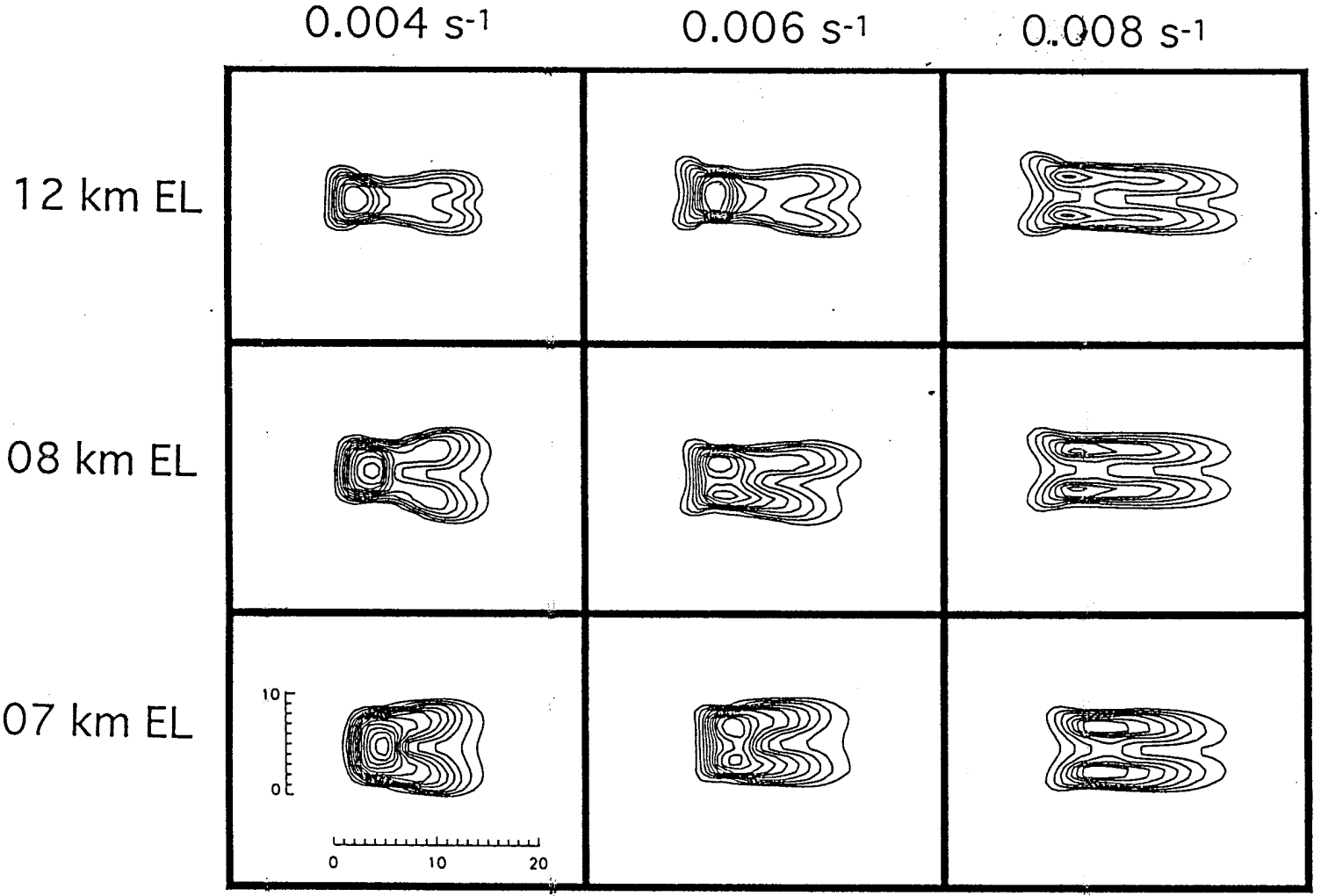

FIG. 8. Surface contours of q_r at interval of 0.5 g kg^{-1} for the nine cases at 30 minutes into each simulation. Scale dimensions in km are located in the lower left of the plot.

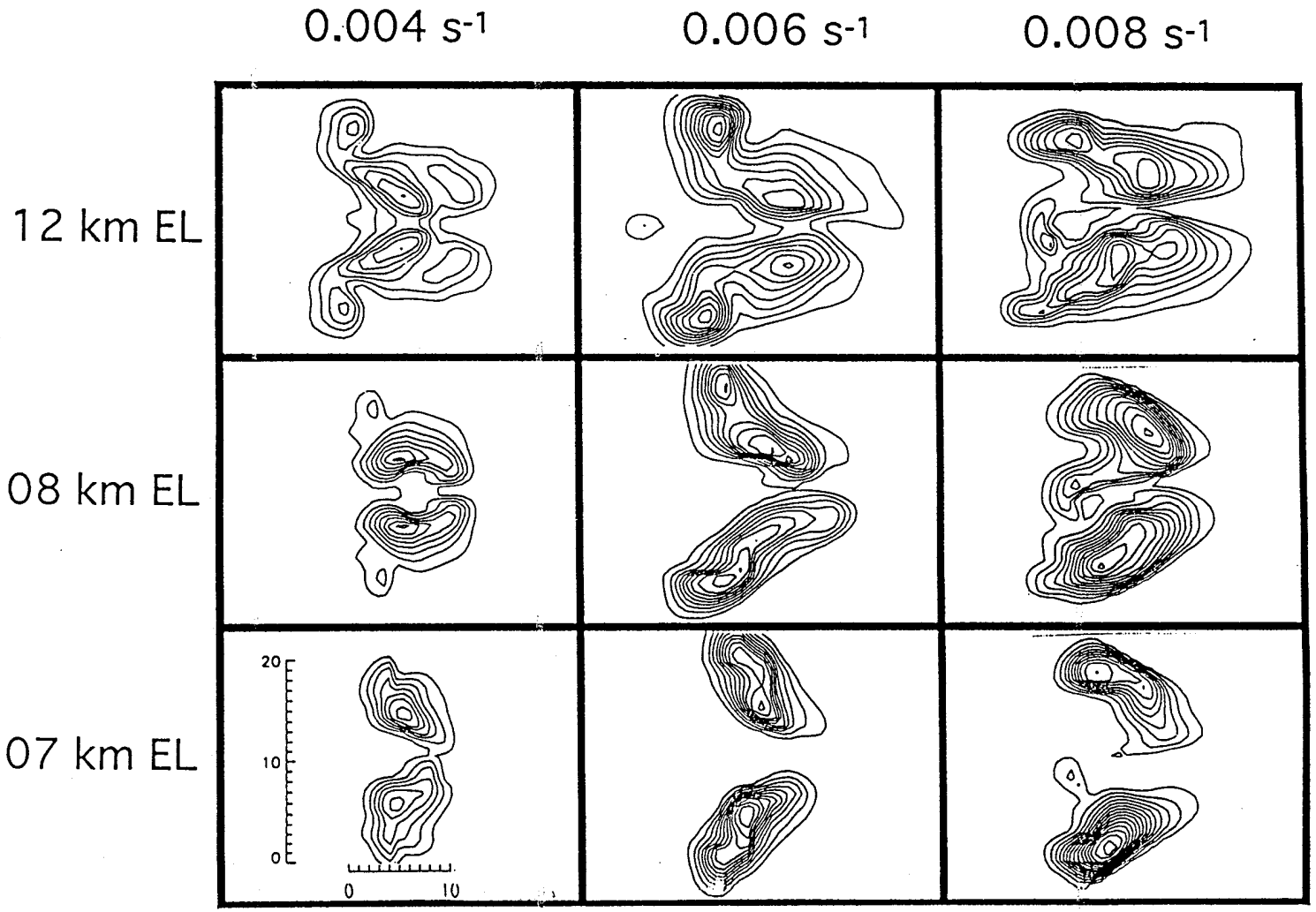

FIG. 9. Surface contours of q_r at interval of 0.5 g kg^{-1} for the nine cases at 60 minutes into each simulation. Scale dimensions in km are located in the lower left of the plot.

stronger storm-relative winds aloft which project precipitation falling further east of the updraft.

Contours of surface rain water mixing ratios do not all appear symmetric in Fig. 9. This is due to the propagation of the domain which is following the rightward moving storm. This results in boundary conditions no longer being symmetric with respect to the split storms.

b. Domain maximum updraft

Fig. 10 is a plot of the evolution of the domain maximum vertical wind speed for the three lowest shear (0.004 s^{-1}) simulations. In these simulations, the updraft strengthens rapidly within the first 10 minutes and becomes quasi-steady over the next 50-60 minutes. The maximum magnitudes are stratified by CAPE, with higher CAPE environments producing stronger domain maximum updrafts. Initially, these updraft magnitudes are stronger than those in higher shear environments having the same CAPE. This is due to weaker mixing of environmental air into the updraft. By 70-75 minutes, however, all three updraft magnitudes show a rapid decrease and then larger variability. Shears were strong enough to produce a splitting updraft that diverged to produce mirror image convection cells deviating left and right of the mean shear vector; however, the rapidly propagating gust front, unhindered by strong surface inflow winds, moved too far ahead of the initial storm and cut off the source of moist boundary layer air necessary for persistent updrafts. These three storms have "gusted out." By 75 minutes, all three low shear storms produce discretely propagating convective cells along the gust front. Because these storms evolved similarly to observed discretely propagating multicells, they were subsequently not analyzed in great detail. This was not to ignore the importance of mechanisms that preclude the formation of long lived supercells but merely to shift the focus of this study to identify possible mechanisms for low-topped supercells reaching tornadic potential. The

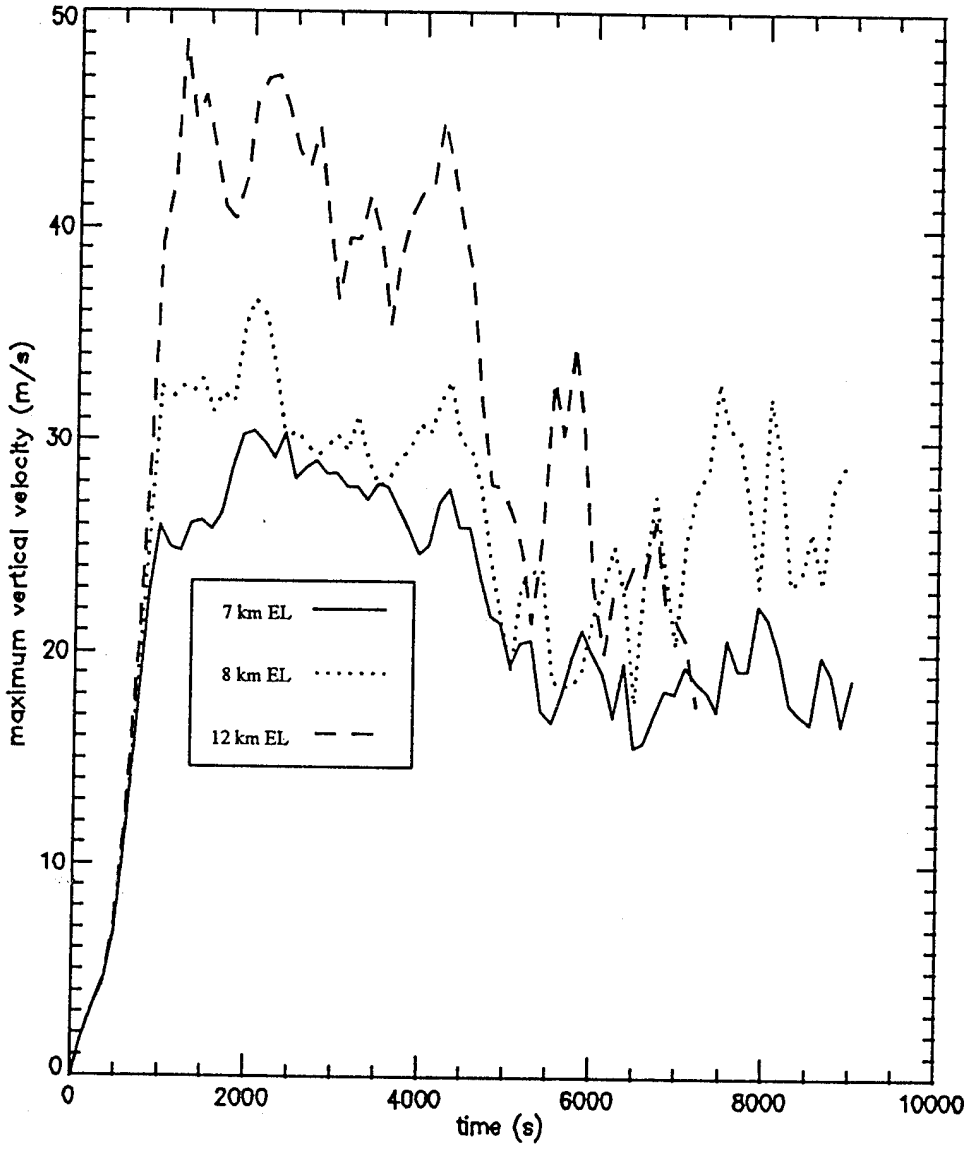

FIG. 10. Evolution of domain maximum updraft for the three 0.004 s^{-1} shear cases. Updraft magnitude is in m s^{-1}.

short duration of these storms is a reflection of Weisman and Klemp's (1982) findings that there are optimum shear and buoyancy magnitudes for the production of a long-lasting convective cell. This low end of the shear spectrum did produce supercells, they were simply not very long lasting.

Figures 11a-c are plots of the domain maximum updraft over the lifetime of the 0.006 s^{-1} and 0.008 s^{-1} shear storms for each EL height. As expected, the strength of the domain maximum updraft is clearly stratified by CAPE. More CAPE means stronger maximum updrafts. The effect of shear magnitude is also seen here. Generally, 0.008 s^{-1} shear storms (dashed lines) have weaker maxima than the 0.006 s^{-1} shear storms (solid lines). The 0.008 s^{-1} shear environments appear to entrain more dry air into the updrafts. Maximum updraft magnitudes are about 5 to 10 m s^{-1} less than the 0.006 s^{-1} shear cases. By one hour, all 6 storms have matured and are producing quasi-steady updrafts. The strength of the updraft in the 0.008 s^{-1} shear cases shows greater variability than in the 0.006 s^{-1} shear cases. The 0.006 s^{-1} shear environments produce supercells with stronger and steadier updrafts than the 0.008 s^{-1} shear environments.

Looking at the BRN values in Table 1 and comparing the general behavior of the nine storms to that which was expected reveals that BRN calculations performed poorly for these simulations. BRN values greater than 35 are found for observed environments producing multicell type storms. It is not surprising then that the 0.004 s^{-1} shear, 12 km EL case produced multicells. It is surprising though, that the 0.004 s^{-1}, 7 km and 8 km EL cases did produce multicells, particularly since these BRN values overlap those of the 0.006 s^{-1} shear cases which produced the most steady supercells. The Bulk Richardson Number as it is currently formulated may not be capable of distinguishing an environment's potential to produce low-topped supercells instead of other storm types. Our ability to distinguish an environment's potential to produce supercells may be enhanced if the vertical distribution of the buoyancy is considered in the formulation of the BRN in place of using only the total CAPE. This is discussed further in Section 4.

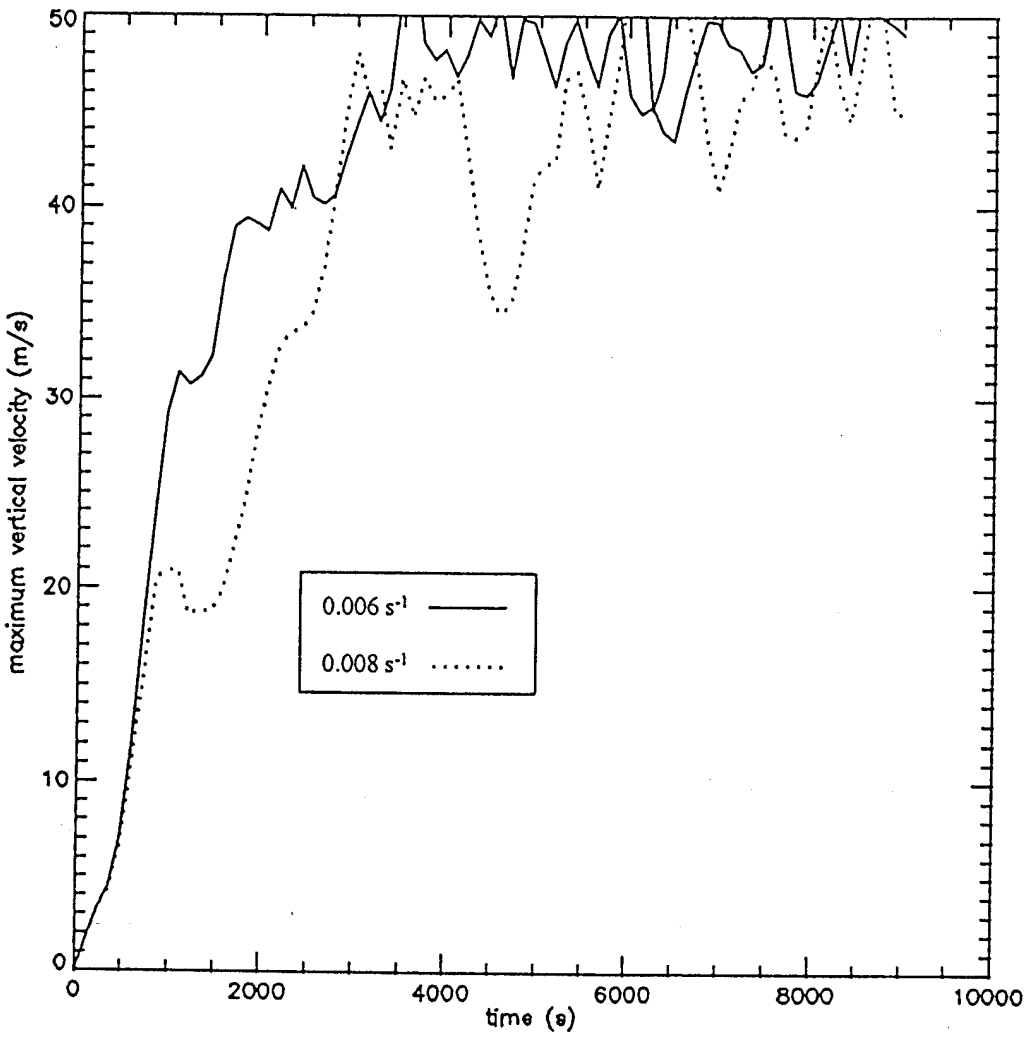

FIG. 11a. Evolution of domain maximum updraft for the 12 km EL, 0.006 s^{-1} and 0.008 s^{-1} shear cases. Updraft magnitude is in m s^{-1}.

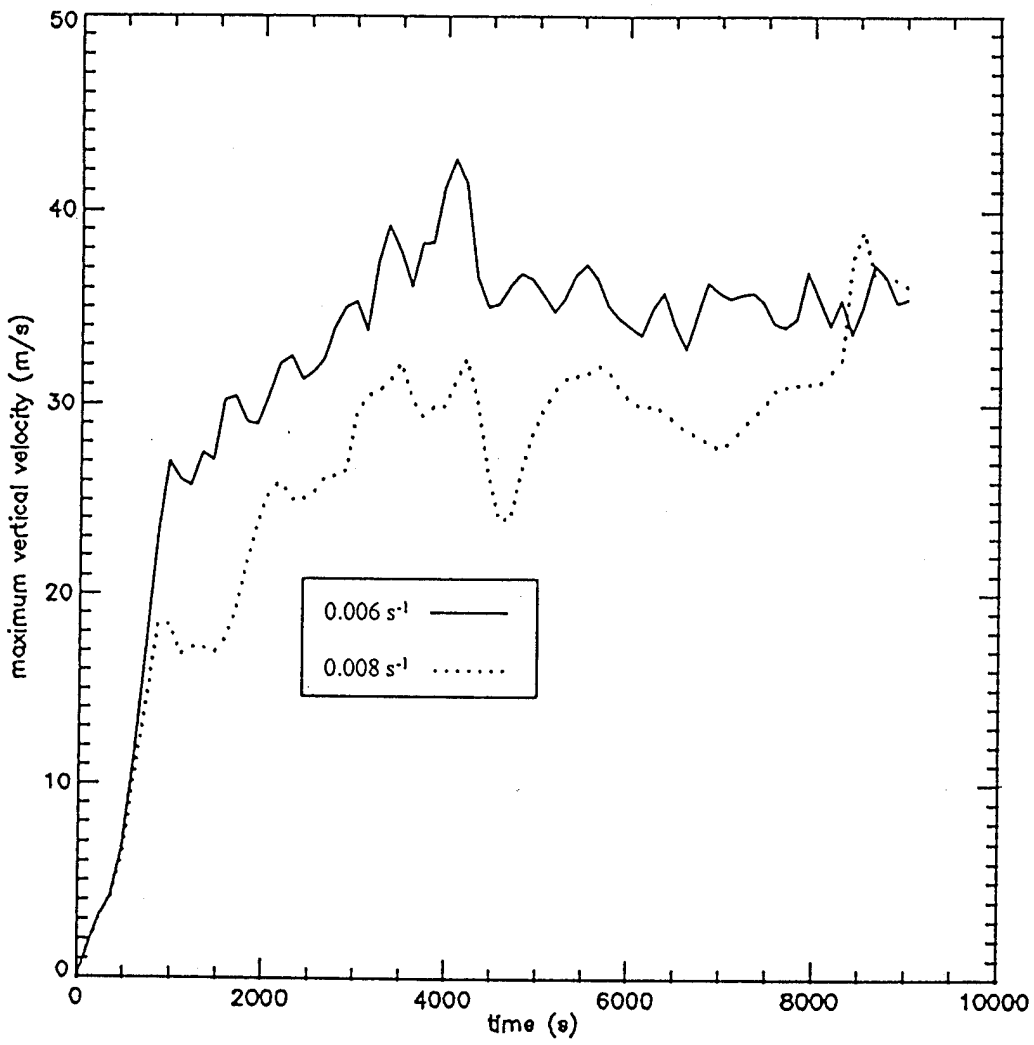

FIG. 11b. Same as FIG. 11a for the 08 km EL, 0.006 s^{-1} and 0.008 s^{-1} shear cases.

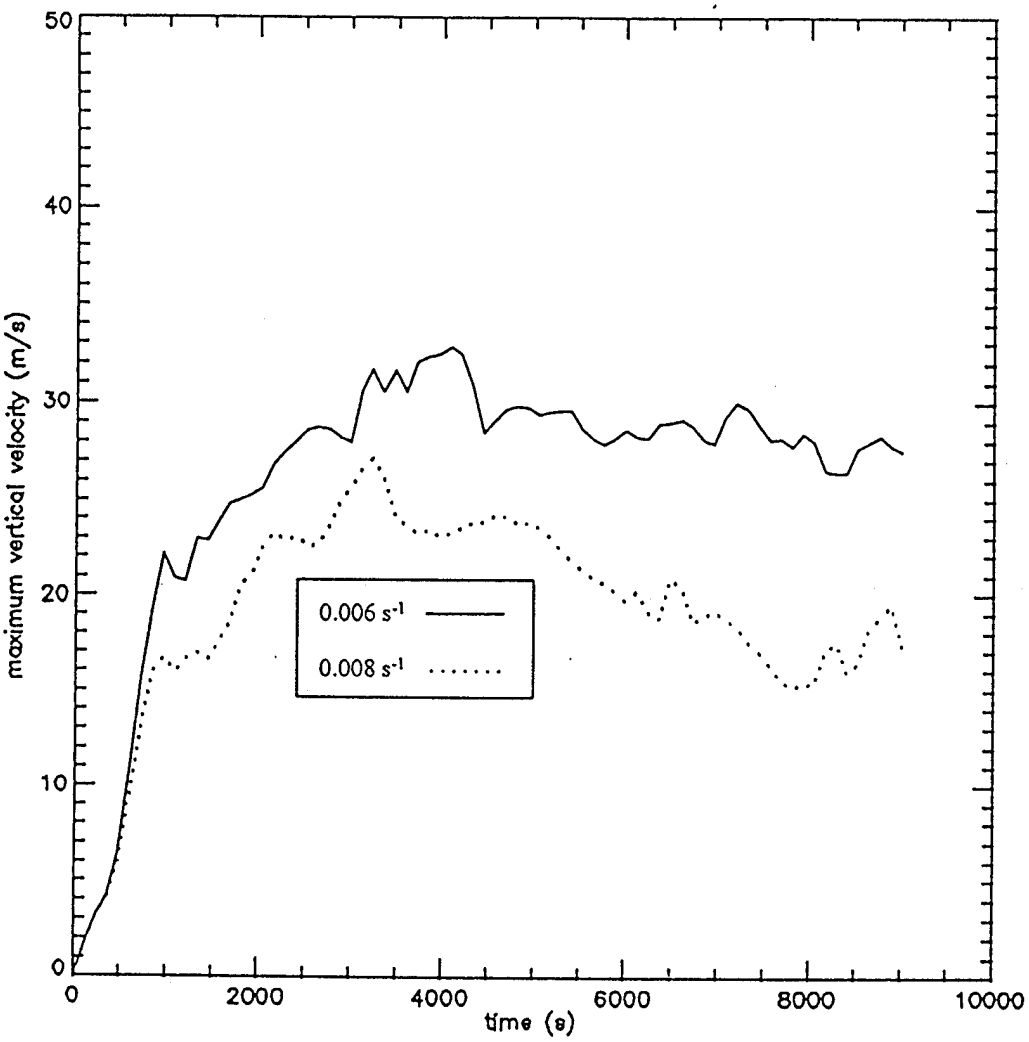

FIG. 11c. Same as FIG. 11a for the 07 km EL, 0.006 s^{-1} and 0.008 s^{-1} shear cases.

c. Water loading

An interesting feature noted on Figs. 11a-b is the sudden dip in the domain maximum updraft magnitude for the 8 km and 12 km EL, 0.008 s^{-1} shear cases. The reason for the dip in updraft magnitude appears to be an imbalance between the water loading of the updraft and the strength of the updraft itself. At 70 minutes into the simulation, water loading has become high enough to begin intruding downward into the updraft inflow region.

As an example, this is depicted in vertical cross sections of the 0.25 g kg^{-1} rainwater mixing ratio contour and wind vectors taken every 5 minutes for the 8 km EL case (Figs. 12a-f). As shown on the domain maximum updraft trend for these cases, the magnitudes of the updraft decreases rapidly between 70 and 80 minutes. Increased rainwater concentrations decrease the ambient temperature of the inflow by cooling the air to the saturation point. Rainwater within unsaturated air will evaporate and absorb latent heat which results in cooling. This cooling reduces the potential temperature of the inflowing parcels resulting in decreased buoyancy and a slowing of the updraft. Between 80 and 90 minutes, the updraft magnitude increases again as rainwater concentrations decrease in response to decreased updraft velocities minutes earlier. Decreasing the updraft strength results in decreased rainwater production. Once rain concentrations are decreased, the inflowing air is cooled less thus retaining more of its original potential instability. By 90 minutes, the updraft has returned to a magnitude sufficient for persistent convection and the rainwater has decreased its downward penetration into the updraft of the storm. The process may then be repeated until an equilibrium is reached or until the updraft is finally cut off, suffocating the storm. The 12 km, 0.008 s^{-1} shear case behaves similarly.

This behavior does not occur in the 8 km and 12 km, 0.006 s^{-1} shear cases. One possible explanation is that the balance between updraft mixing and updraft strength develops an equilibrium. Updraft strength is limited due to mixing by the ambient shear. This same mixing can reduce rainwater production aloft by drying the moist buoyant

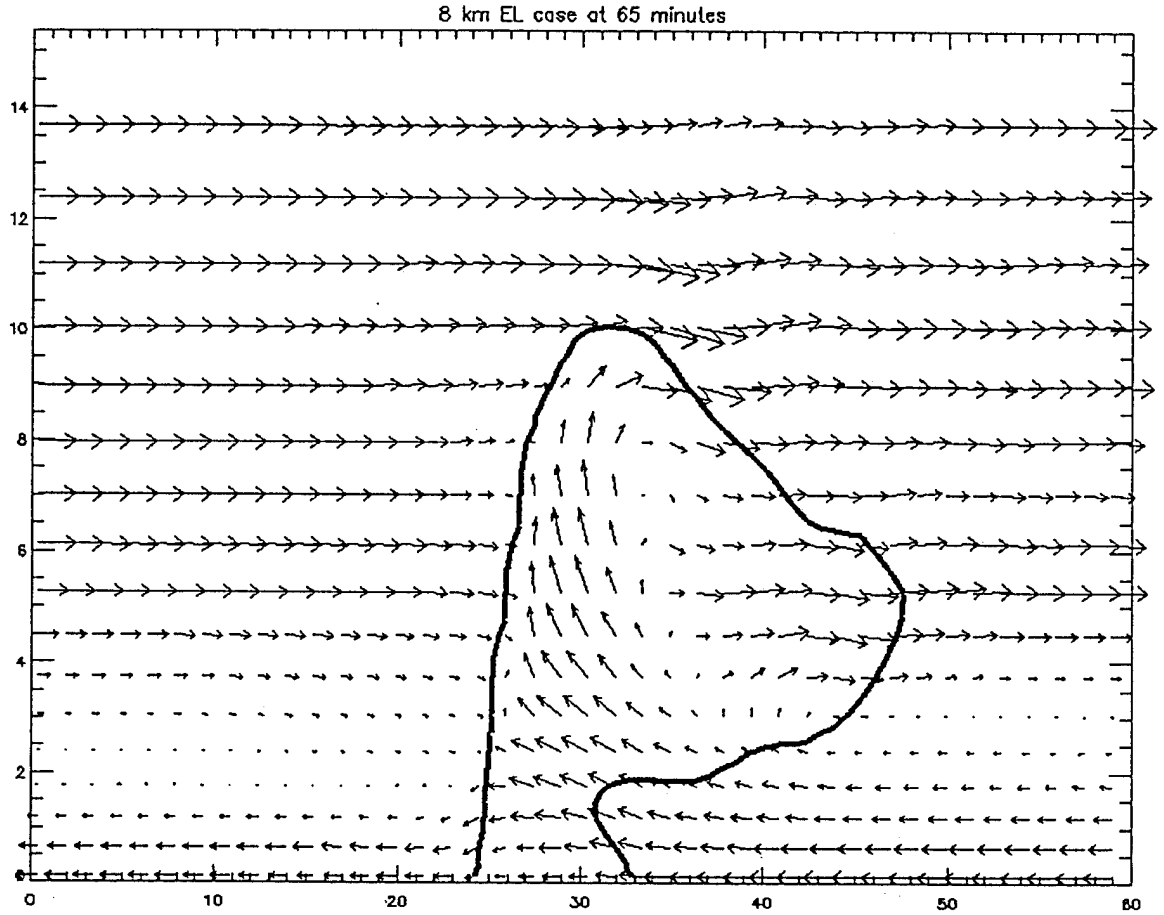

FIG. 12a. Vertical cross section of rain region and wind vectors for the 08 km EL, 0.008 s^{-1} shear case at 65 minutes into the simulation. View is facing north into page. Rain region marked by 0.25 g kg^{-1} q_r contour. Scale of wind vectors is 10 m s^{-1} for each 1 km distance horizontally. Vertical distances are stretched by a factor of three.

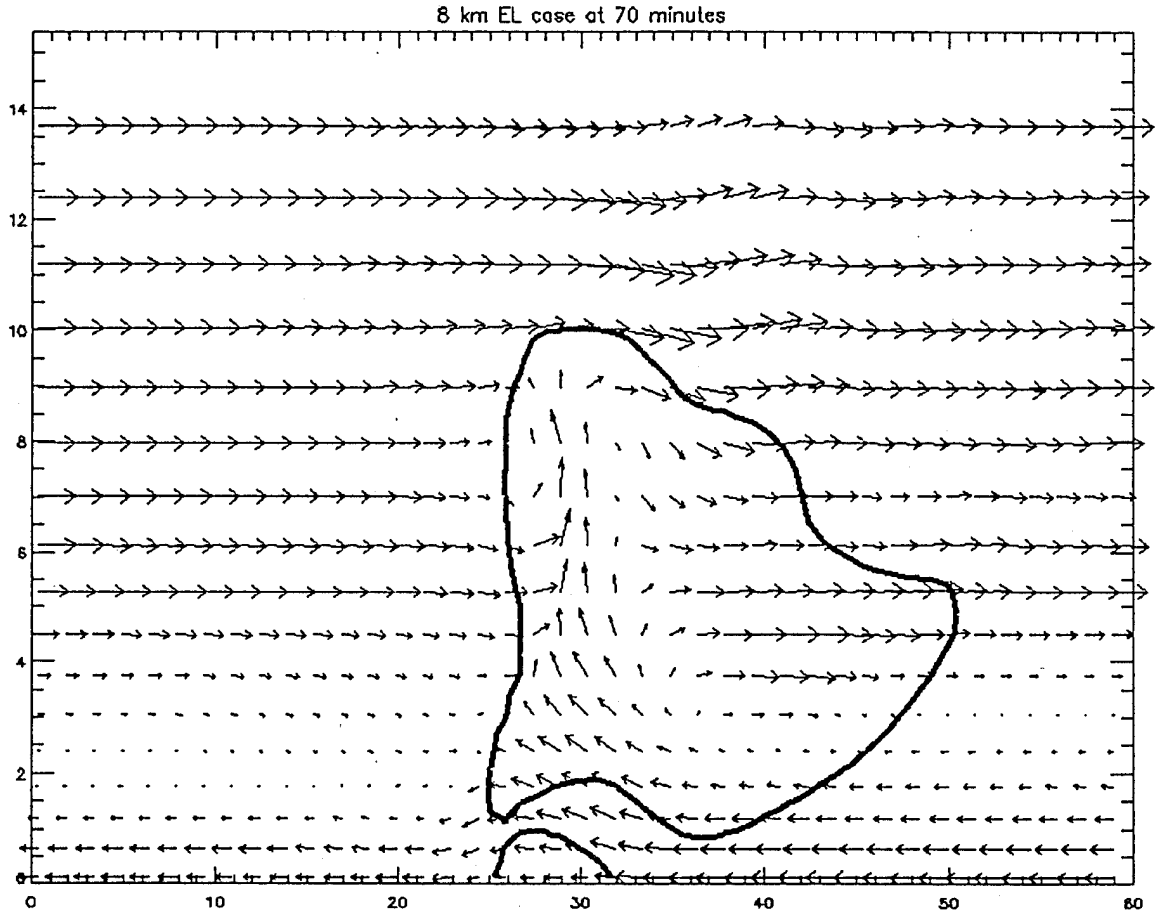

FIG. 12b. Same as FIG. 12a at 70 minutes.

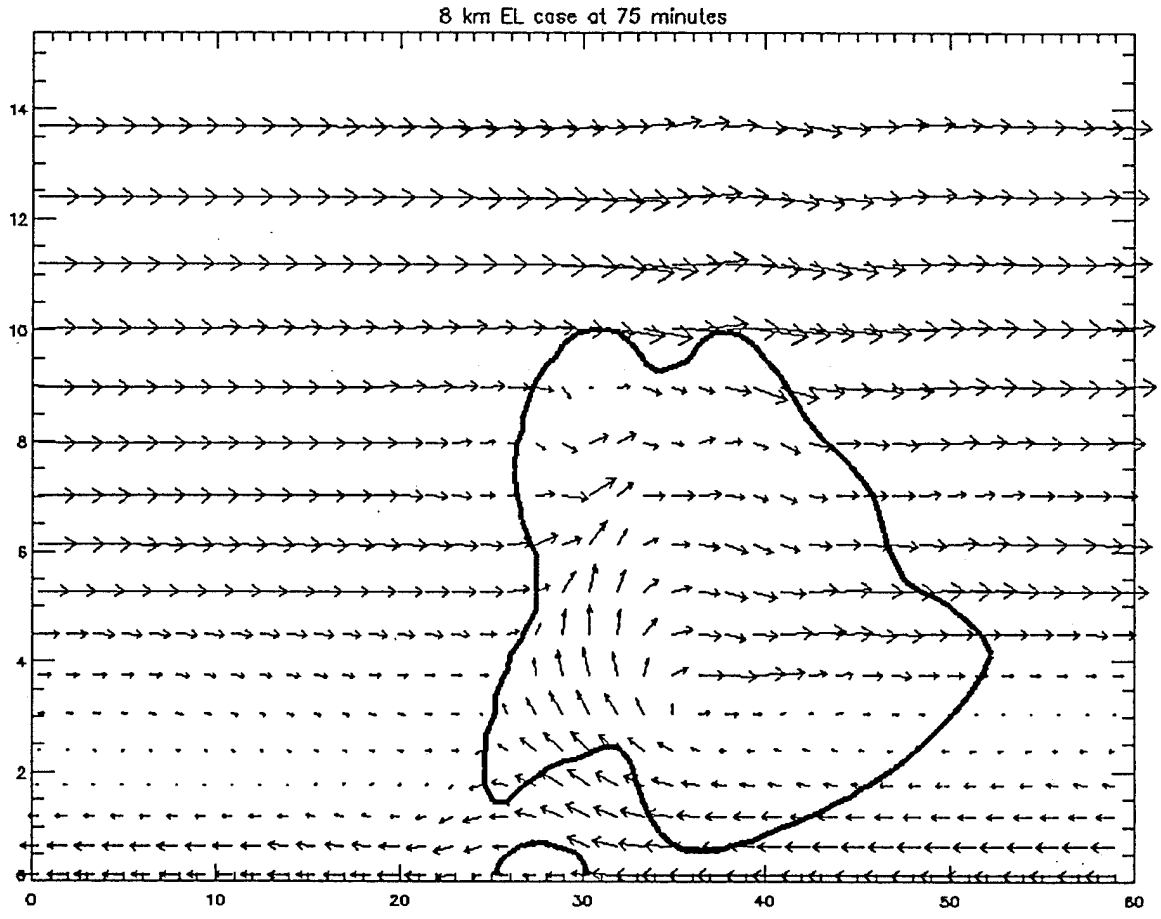

FIG. 12c. Same as FIG. 12a at 75 minutes.

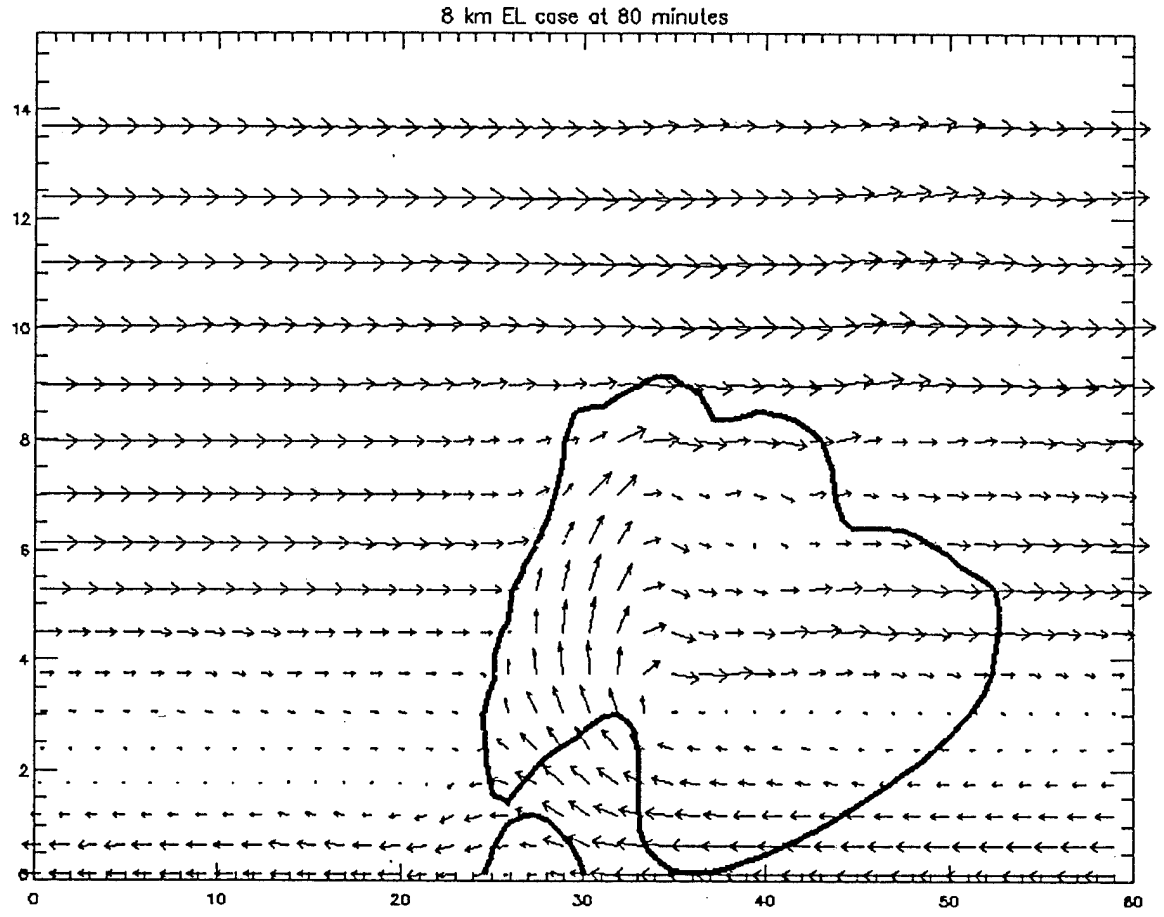

FIG. 12d. Same as FIG. 12a at 80 minutes.

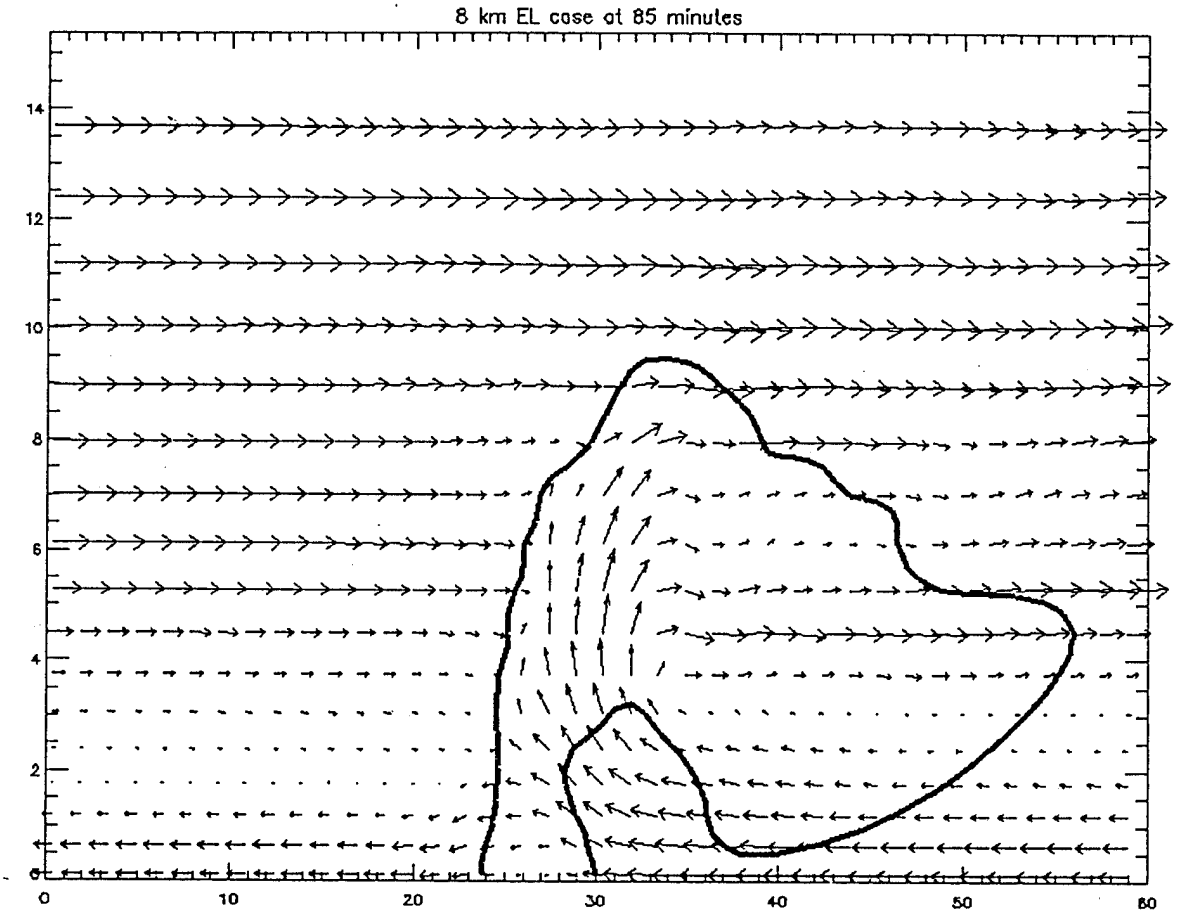

FIG. 12e. Same as FIG. 12a at 85 minutes.

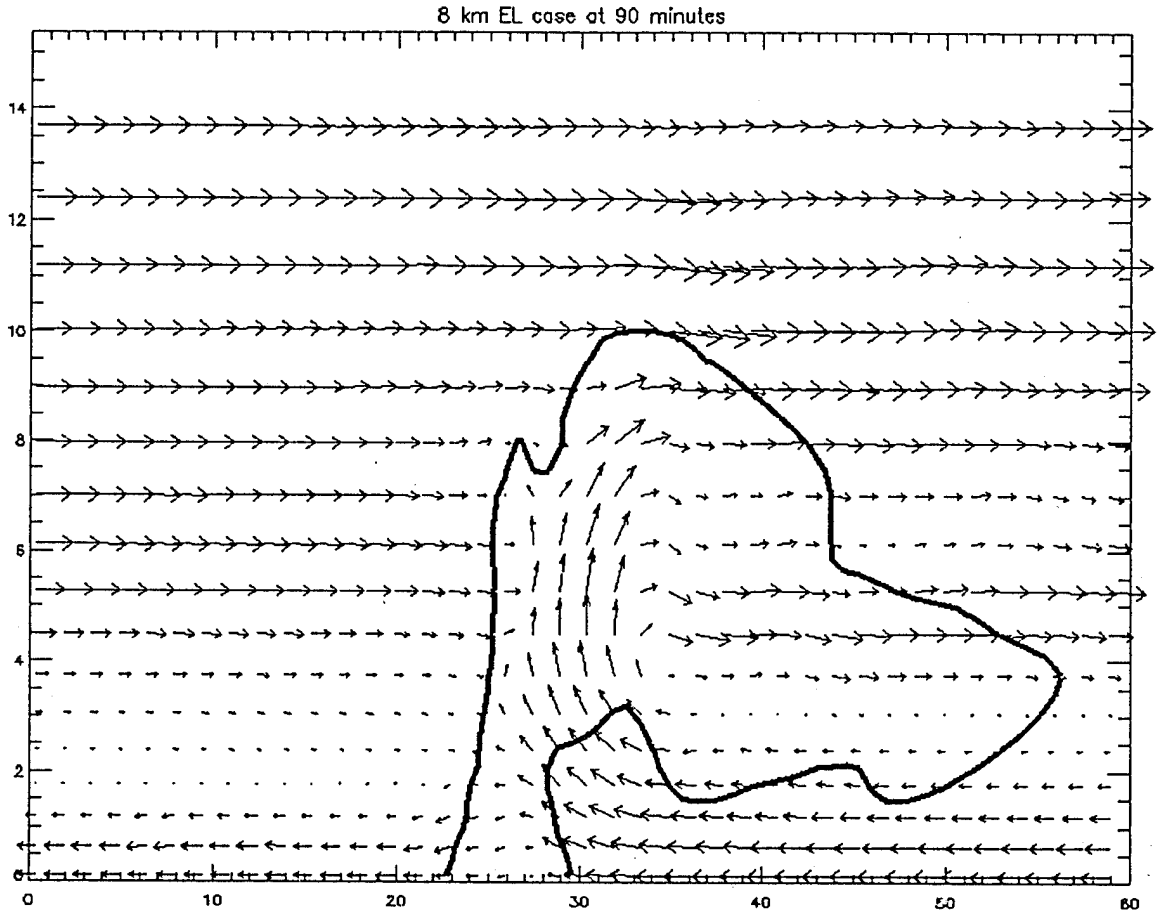

FIG. 12f. Same as FIG. 12a at 90 minutes.

column. However, increasing the shear may have a stronger impact on weakening the developing low-level updraft than on reducing the rainwater production aloft. This could result in water loading penetrating deeper into the updraft. This dip is not seen in the 7 km EL, 0.008 s^{-1} shear case. This may be because vertically integrated rain water is smaller since the updraft in the 7 km EL, 0.008 s^{-1} shear case is limited to a shallower depth. The decreased water loading results in a lower sensitivity to variations in shear magnitude.

d. Time-averaged updraft

The evolution of the maximum updraft at each of the 35 vertical levels of the model for the 0.006 s^{-1} shear cases are given in Figs. 13a-c. In the 12 km EL storm (Fig. 13a), the maximum updraft magnitude is about 48 m s^{-1} at an altitude of about 10 km. Low and mid-level magnitudes are steady, and there are pulses in the maximum magnitude at the higher levels of the storm. Figure 13b is for the same shear, 8 km EL case. The maximum updraft magnitude is about 35 m s^{-1} at 7 km and there is less variability in its strength at the upper levels. Figure 13c is for the same shear, 7 km EL case. The maximum updraft magnitude is about 29 m s^{-1} at 6 km and there is almost no variability in its strength at the upper levels. Again these plots illustrate the stratification of maximum updraft and of the height at which the maximum occurs by total CAPE. The updrafts of these storms show decreased variability in the upper levels as the EL is decreased. It is speculated that this may be a result of higher water loading in the upper part of the storm, or possibly an effect of stronger vertical gravity waves as the updraft parcels impinge against the stable layer above the EL.

It is apparent that below 5 km there is little variability in the strength of the maximum updraft and that all three storms have similar low-level vertical distributions of maximum vertical wind speed. The time-averaged vertical distribution of the maximum updraft velocity for the mature supercells based on the three plots in Figs. 13a-c and for similar data

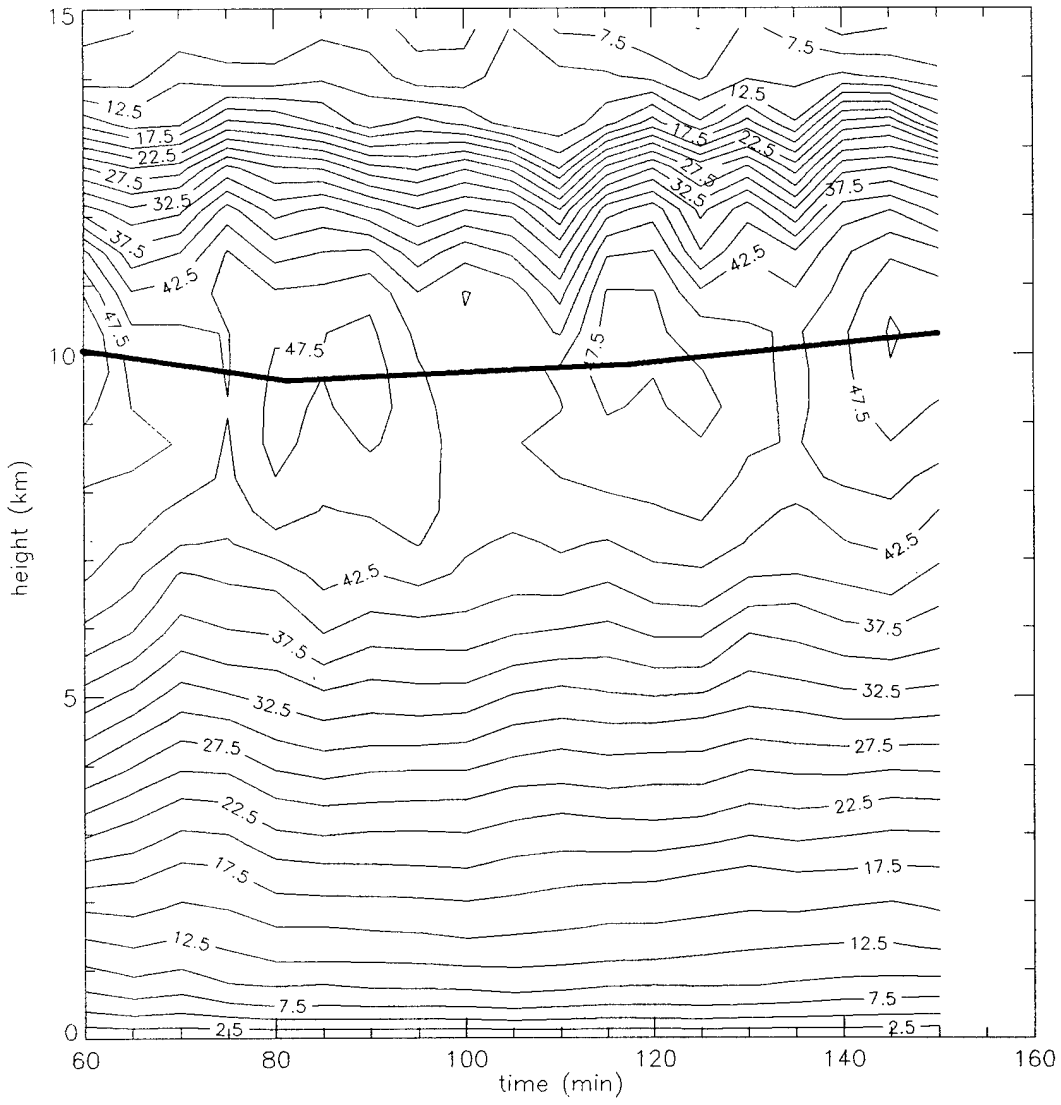

FIG. 13a. Evolution of vertical distribution of maximum updraft for the 0.006 s^{-1} shear, 12 km EL case. Time units are in minutes between 60 minutes and 150 minutes. Thick solid line represents position of domain maximum updraft. Contour interval is 2.5 m s^{-1}.

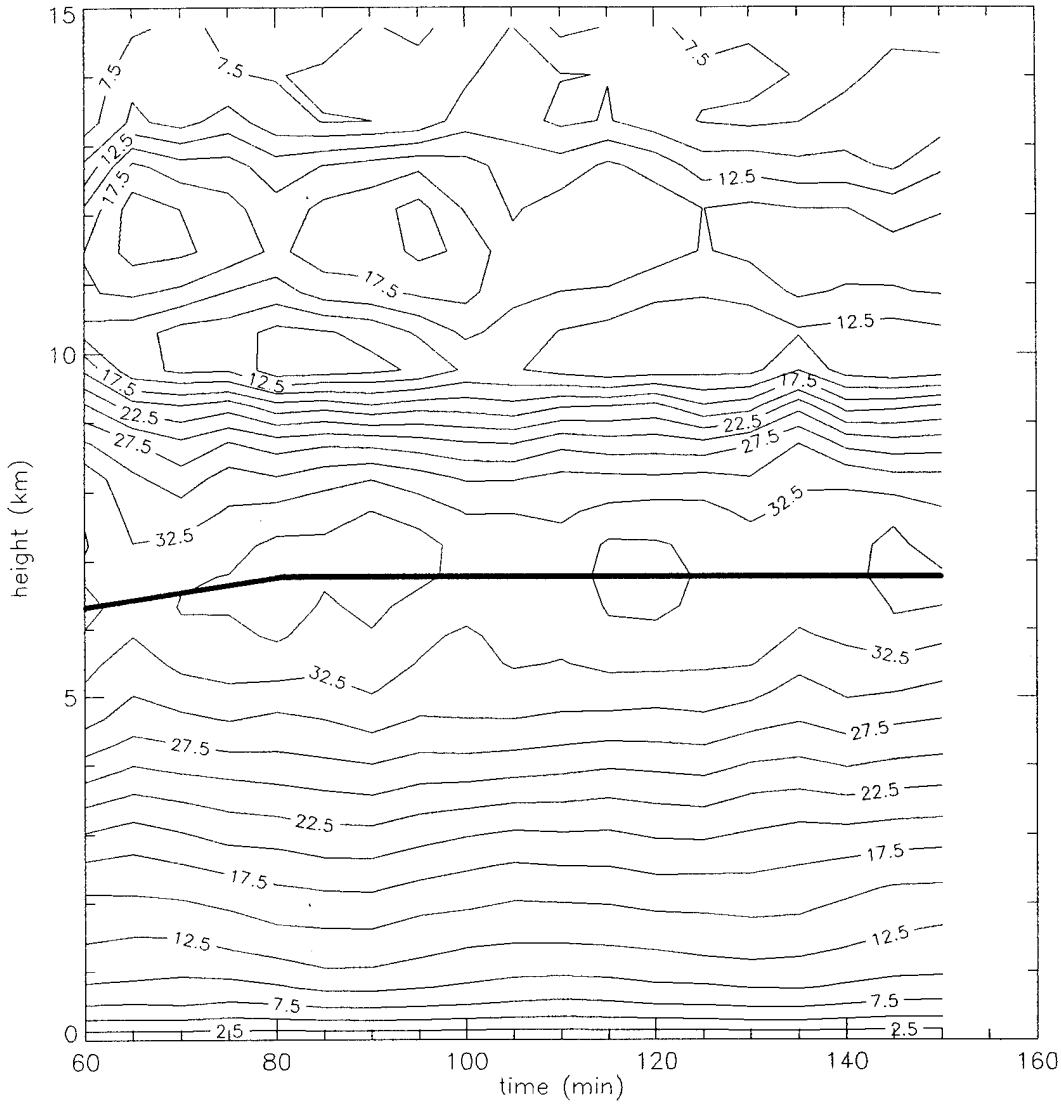

FIG. 13b. Same as FIG. 13a for the 0.006 s^{-1} shear, 08 km EL case.

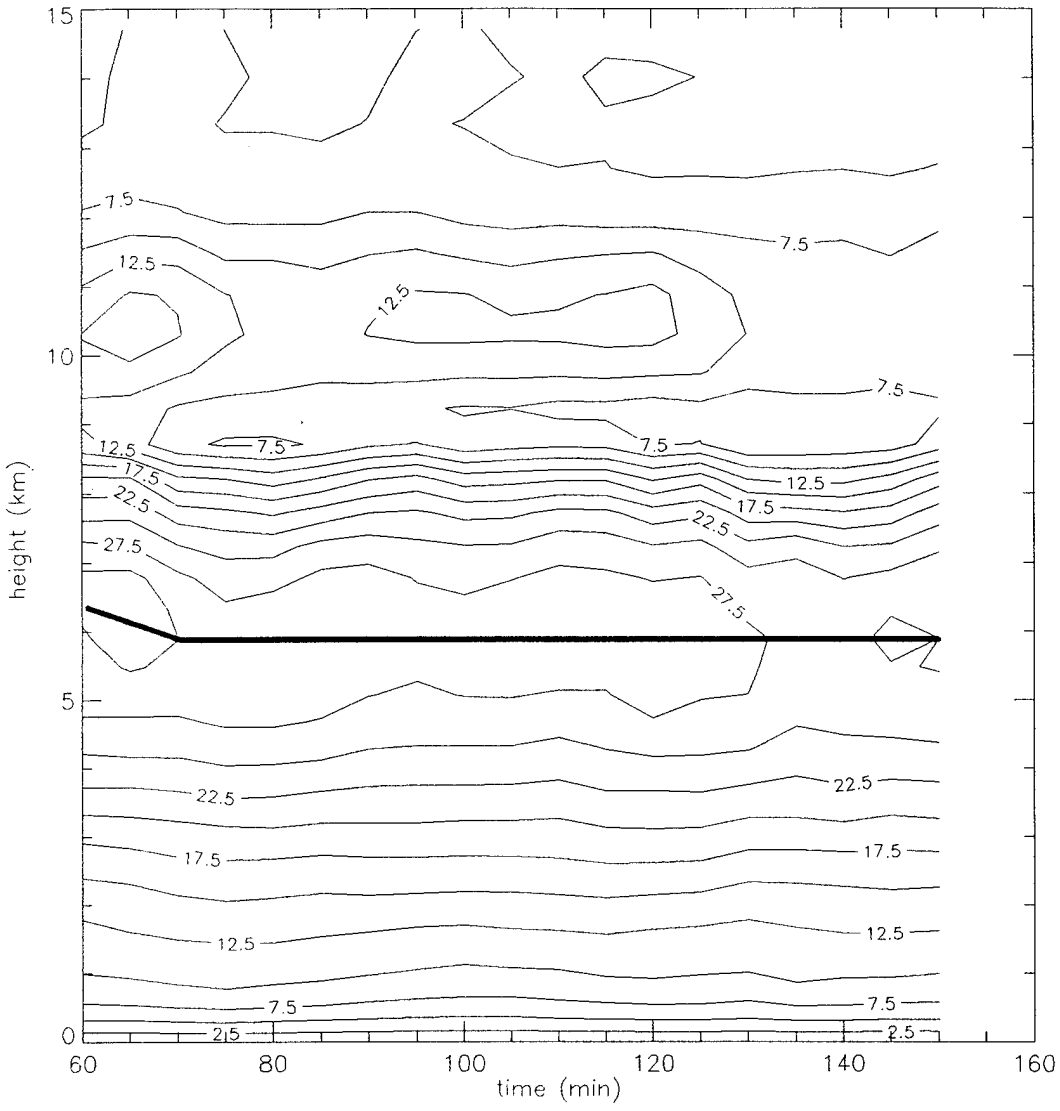

FIG. 13c. Same as FIG. 13a for the 0.006 s^{-1} shear, 07 km EL case.

collected for the 0.008 s^{-1} shear cases for each EL are presented in Figs. 14a-c. These figures again show strongest updraft magnitudes occur for an environmental shear of 0.006 s^{-1} for all three EL cases tested.

e. Energy overturning efficiency

A qualitative measure of the modeled storm's efficiency at converting buoyant potential energy to updraft kinetic energy is the ratio of measured maximum updraft speed to the theoretical maximum updraft predicted by parcel theory (McCaul and Weisman 1995).

$$\text{"Overturning Efficiency"} = \frac{w_{\max}}{\sqrt{2CAPE}} \tag{2}$$

This is the same parameter representing storm strength (S) quantified by Weisman and Klemp (1982, 1984) where S is the maximum vertical velocity obtained in a particular storm normalized by the maximum which would have occurred based solely on buoyancy. Figure 15 is constructed using the maximum values of time-averaged maximum vertical wind speed for each storm. These values indicate that the 0.006 s^{-1} shear produces the best "overturning" efficiency. Additionally, for the 0.006 s^{-1} shear cases, as total CAPE decreased, efficiency increased. This may be a function of rainwater production. Deeper storms produce more rain and may have decreased overall potential instability. How water loading affects potential instability and overall efficiency is seen in the following equation:

$$MoistCAPE = CAPE + Loading \tag{3}$$

where $CAPE = g\int_{lfc}^{el}\left(\frac{\theta - \overline{\theta}}{\overline{\theta}}\right)dz$

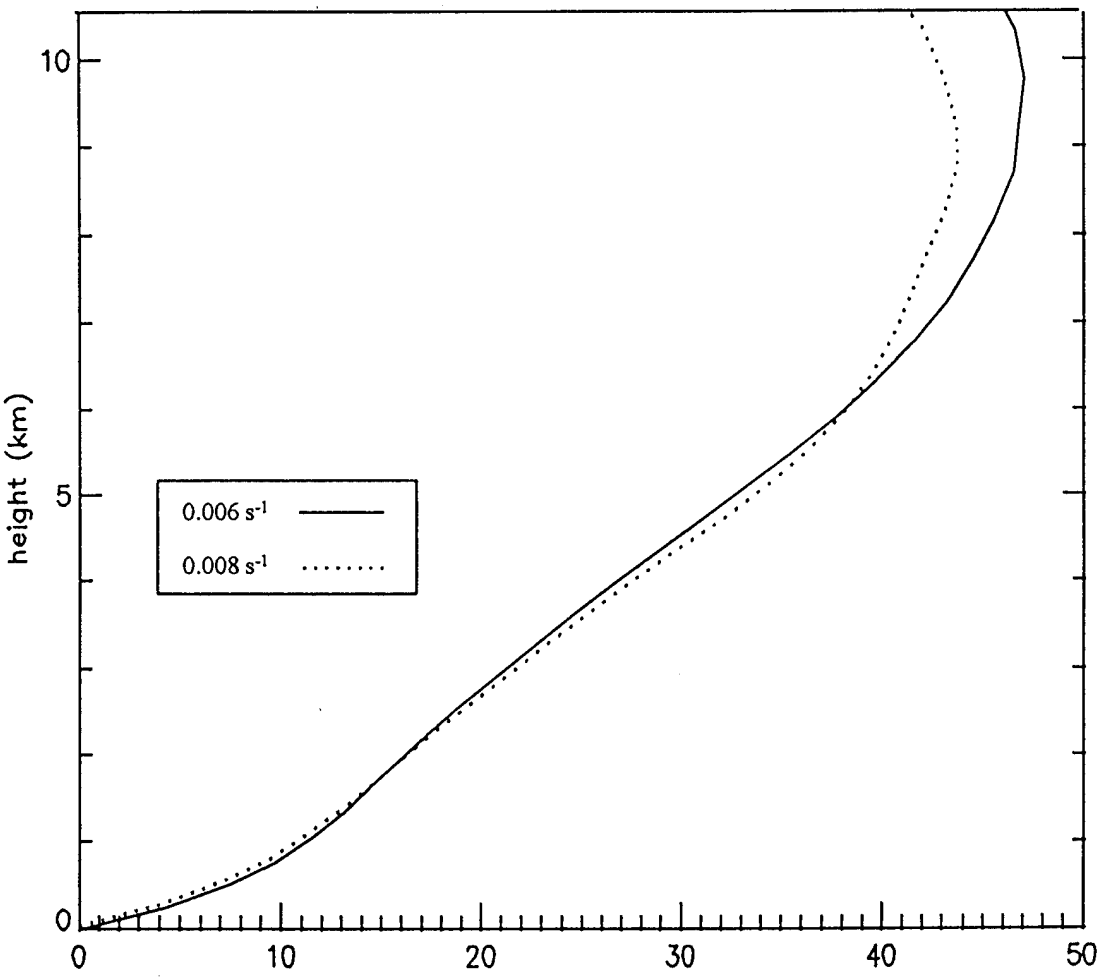

FIG. 14a. Time averaged evolution of vertical distribution of maximum updraft for the 12 km EL, 0.006 s^{-1} and 0.008 s^{-1} shear cases. Magnitudes are averaged over the 60 minute to 150 minute time interval. Solid line represents 0.006 s^{-1} shear cases, dotted line represents 0.008 s^{-1} shear cases.

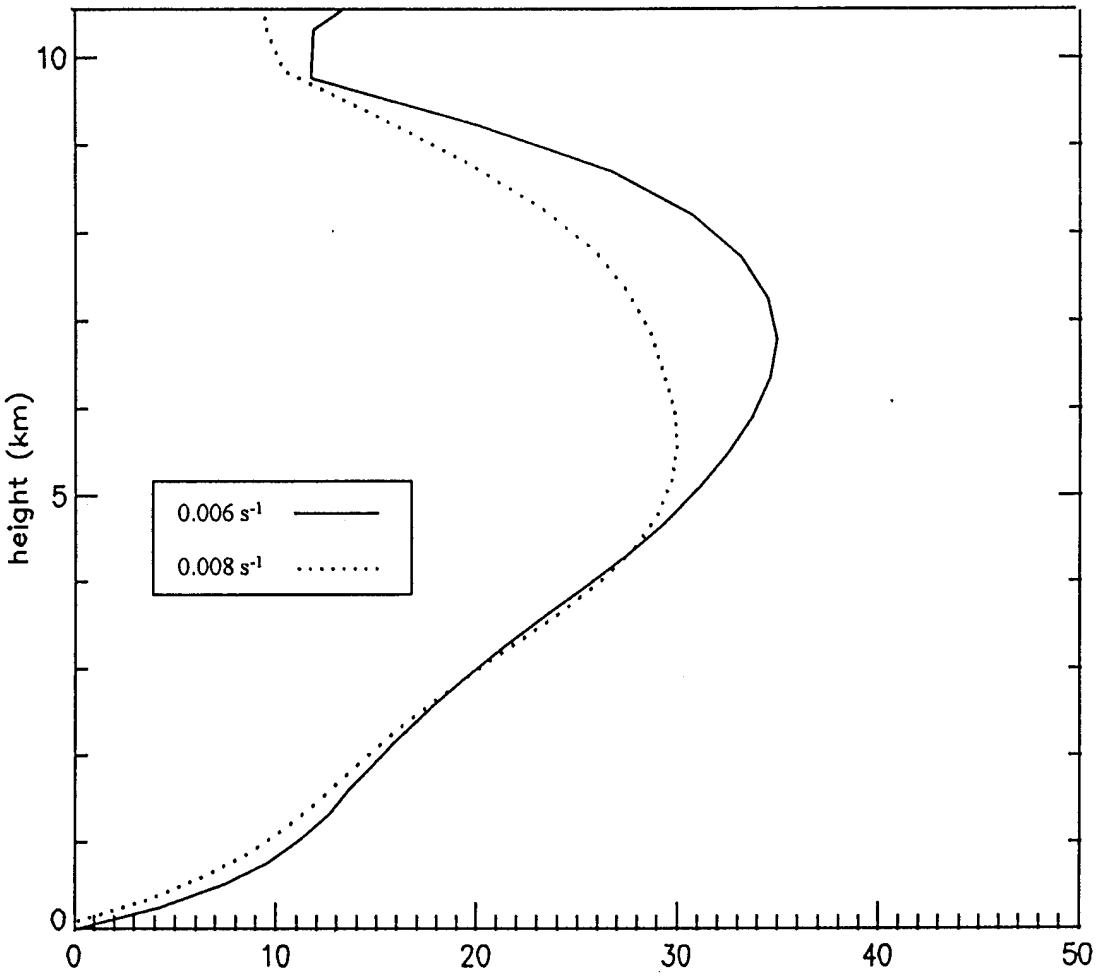

FIG. 14b. Same as FIG. 14a for the 08 km EL, 0.006 s^{-1} and 0.008 s^{-1} shear cases.

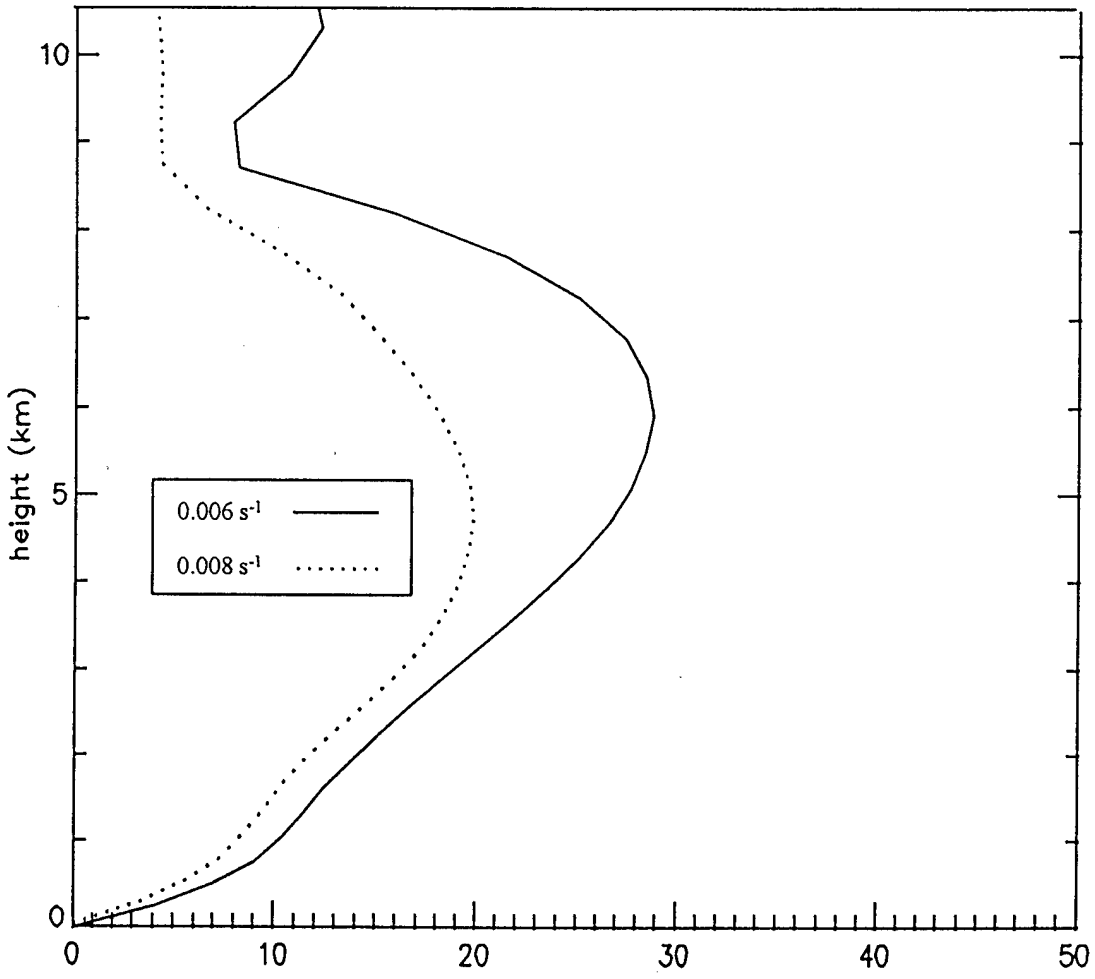

FIG. 14c. Same as FIG. 14a for the 07 km EL, 0.006 s^{-1} and 0.008 s^{-1} shear cases.

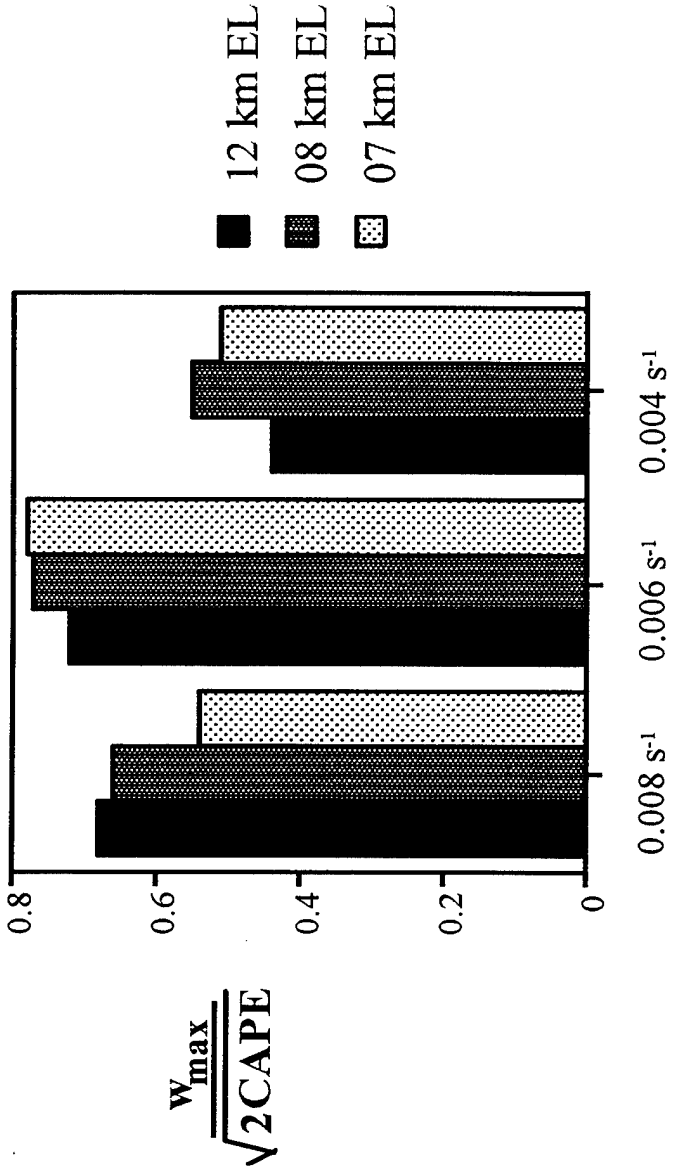

FIG. 15. Plots of overturning efficiency (dimensionless) for each of the nine simulations.

and $MoistCAPE = g\int_{lfc}^{el}\left(\frac{\theta-\overline{\theta}}{\overline{\theta}} + 0.61q_v' - q_c - q_r\right)dz$

The evaporation and water loading terms included in the equation can cause the maximum updraft velocity to deviate from that expected by parcel theory which uses only *CAPE*. As suggested by McCaul and Weisman (1995), differences in efficiency may also be due to differences in entrainment of the updraft because shear strengths vary among the cases. The best shear profiles (0.006 s^{-1} shear) produced stronger persistent updrafts and stronger storm deviate motion. Storm deviate motion in these unidirectional wind profile experiments produces a veering storm-relative wind profile (in the rightward propagating storm of the mirror image pair) and subsequently, increasing storm-relative helicity. Davies-Jones (1984), and Droegemeier et al. (1993) suggested an updraft with high helicity has the property of entraining less which results in increased energy "overturning" efficiency. The three 0.004 s^{-1} shear cases show lower overturning efficiency values because the time-averaged updraft strength is smaller (due to gust out) than in the higher shear cases.

f. Vertical rotation

The evolution of the maximum vertical vorticity at each of the 35 vertical levels for the 0.006 s^{-1} shear cases is given in Figs. 16a-c. The region of vertical vorticity higher than 0.02 s^{-1} is shaded. Maximum vertical vorticity occurs in the middle and upper portions of the three storms. In accordance with the definition of supercells, these storms have large vertical rotation over a significant depth of each storm. The lower boundary of the mid-level mesocyclone is between 2 and 3 km. As expected, the magnitude as well as the depth of the mid-level mesocyclone is stratified by CAPE. Mesocyclone intensity is stronger in higher CAPE environments reflecting a larger production of vertical vorticity through

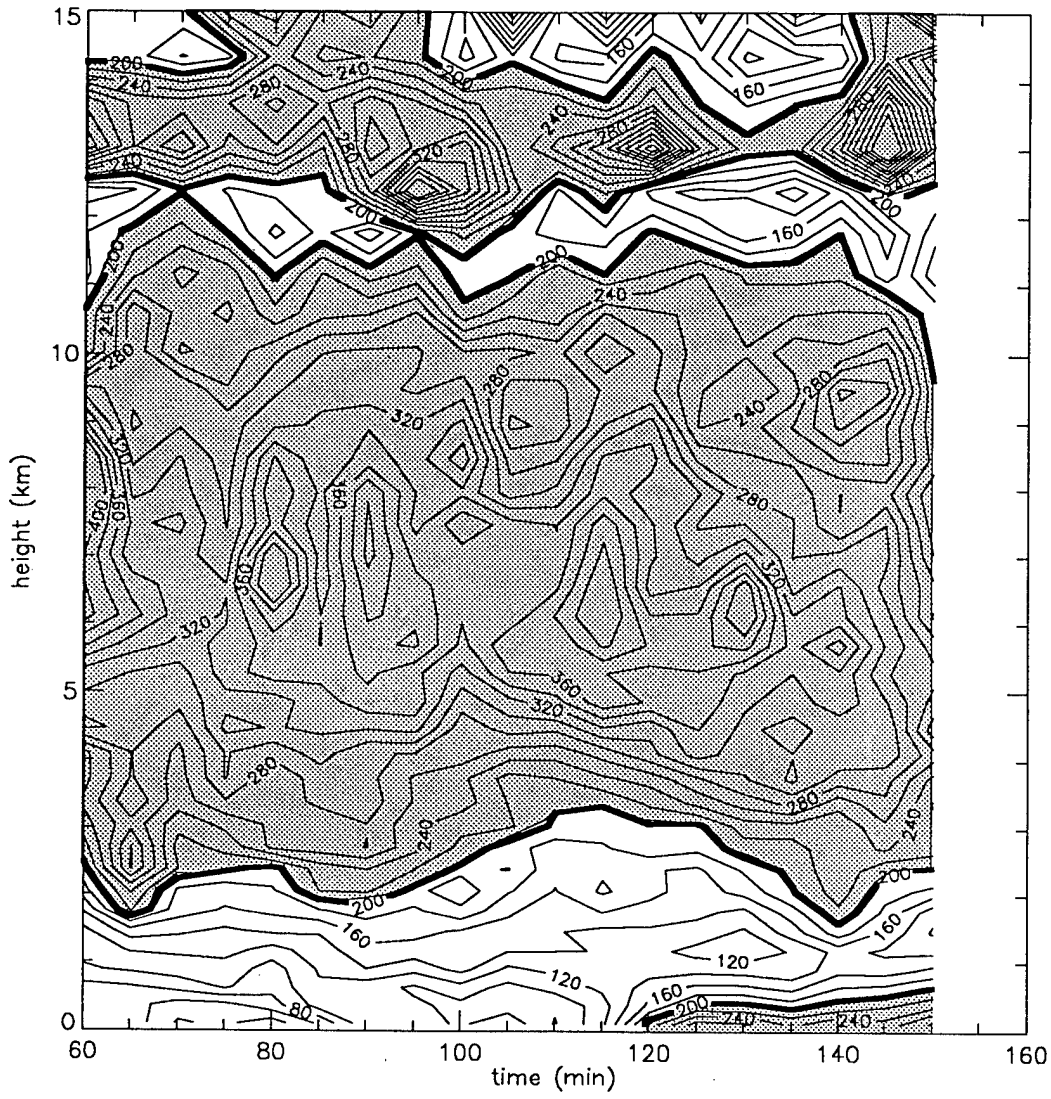

FIG. 16a. Evolution of vertical distribution of maximum positive vertical vorticity for the 0.006 s^{-1} shear, 12 km EL case. Time units are in minutes between 60 minutes and 150 minutes. Magnitudes are in 10^{-4} s^{-1}, and contour interval is 20 x 10^{-4} s^{-1}. Thick solid line represents contour of 0.02 s^{-1}, and shaded area represents positive vertical vorticity magnitudes > 0.02 s^{-1}.

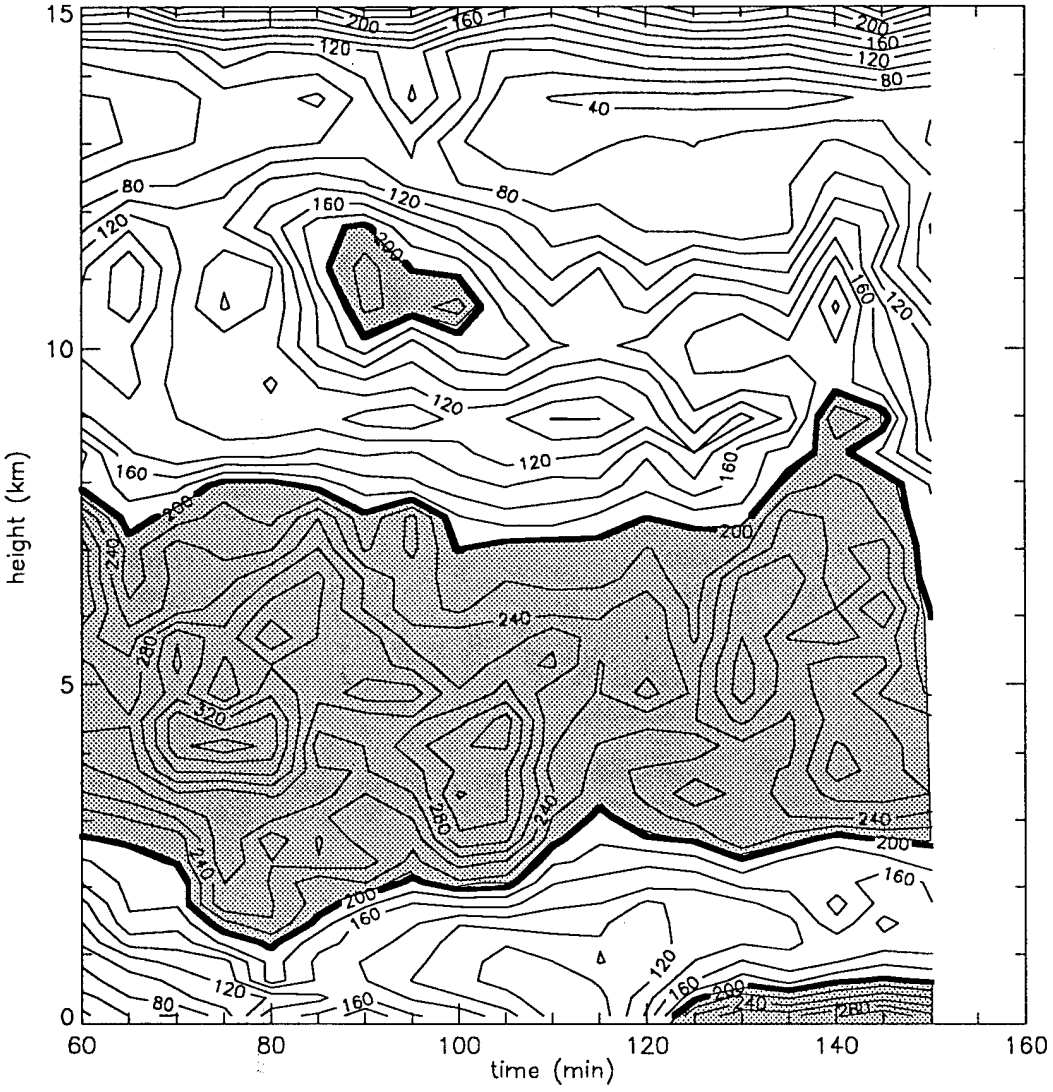

FIG. 16b. Same as FIG. 16a for the 08 km EL case.

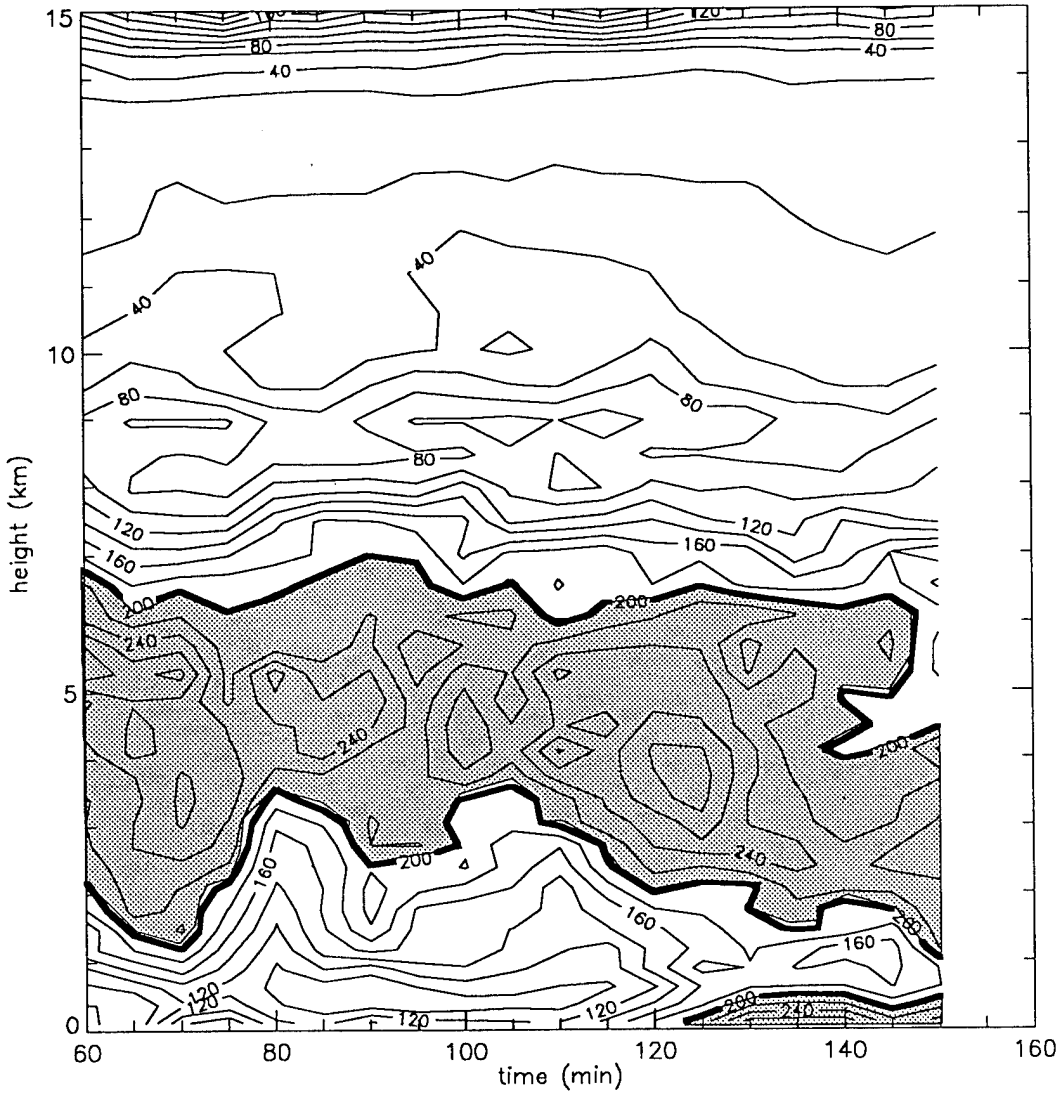

FIG. 16c. Same as FIG. 16a for the 07 km EL case.

tilting and stretching by stronger updrafts. Below 5 km, however, the vertical distribution of vertical vorticity is similar among these three cases.

A low-level region of high vertical vorticity develops at about 120 minutes into all three of these simulations. This signals the development of the low-level mesocyclone which represents the parent tornado mesocyclone in nature. There is a distinct minimum between the lower boundary of the mid-level mesocyclone and the low-level mesocyclone. The separation of the low-level mesocyclone from the mid-level mesocyclone is similarly detailed by Brandes (1984) in his observations of the Del City-Edmond tornadic storm of 20 May 1977. It is interesting to note that the magnitude of the low-level mesocyclone peaks at 0.03 s^{-1} for all three cases. The strength of the low-level mesocyclone appears then to be uncorrellated with the strength, depth, or altitude of the mid-level mesocyclone. Klemp and Rotunno (1983) showed that low-level mesocyclone intensity is largely a result of horizontal vorticity generated along the strong buoyancy gradients within the lower levels of the storm. The results here may imply low-topped supercells can develop strong low-level mesocyclones independent of the strength of the mid-level rotation normally observed on radar.

g. Time-averaged vertical vorticity distribution

To pull out the largest signal in the vertical vorticity evolution plots in Figs. 16a-c, the time-averaged maximum vertical vorticity for the 0.006 s^{-1} and 0.008 s^{-1} shear storms are presented for each EL case in Figs. 17a-c. The dashed lines represent the 0.008 s^{-1} shear cases and the solid lines represent the 0.006 s^{-1} shear cases. The altitude at which the vertical vorticity is a maximum (a reasonable approximation to the altitude of the maximum mid-level mesocyclone strength) varies little for a particular CAPE. Generally, this altitude increased with increasing CAPE. This is a reflection of the heights at which the maximum updraft velocity occurs. The maximum strength of the mid-level mesocyclone increases

55

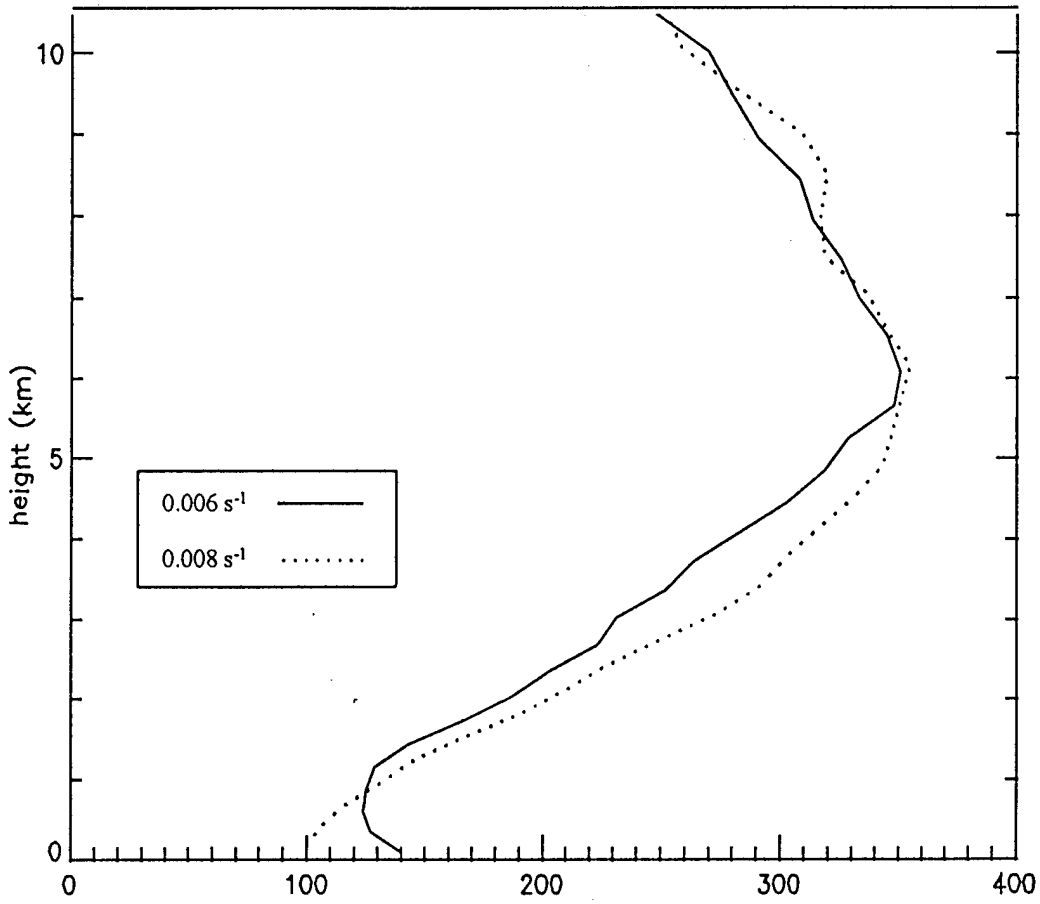

FIG. 17a. Time averaged evolution of vertical distribution of maximum positive vertical vorticity for the 12 km EL cases. Values are averaged over the 60 minute to 150 minute time interval. Solid line represents 0.006 s^{-1} shear cases, dotted line represents 0.008 s^{-1} shear cases. Magnitudes are in 10^{-4} s^{-1}.

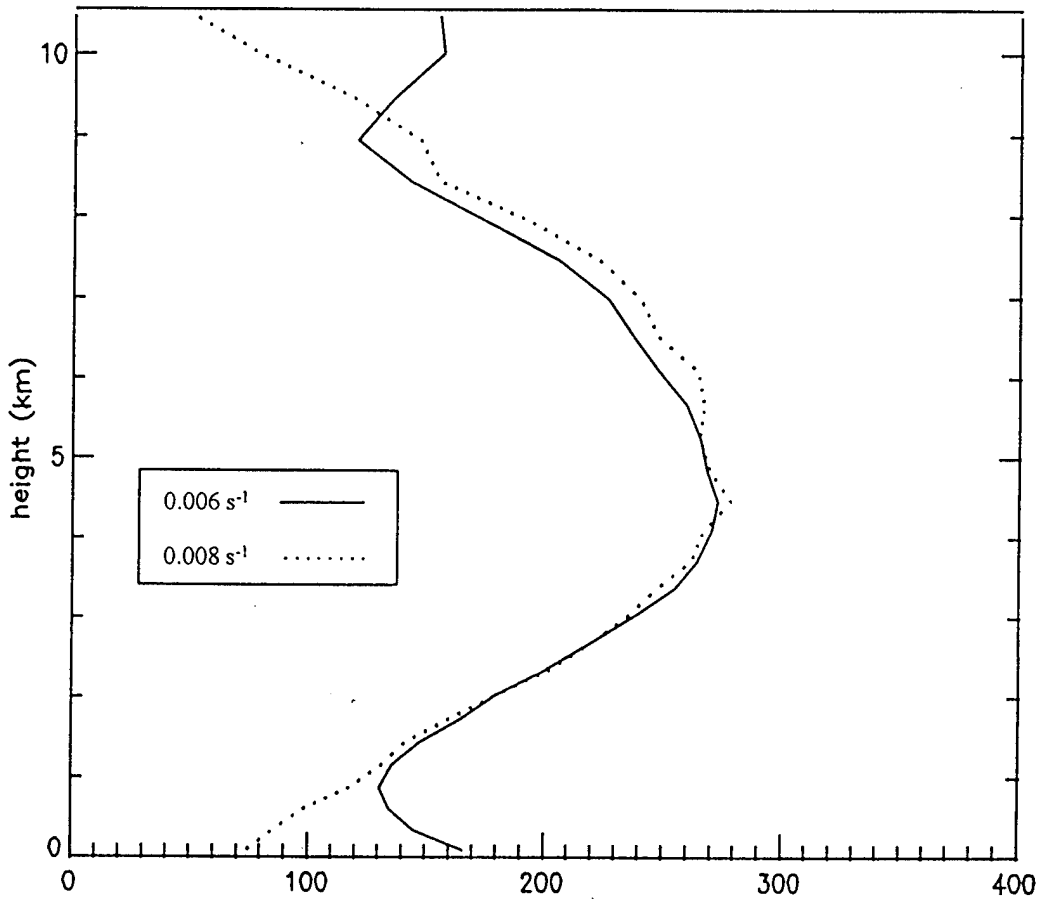

FIG. 17b. Same as FIG. 17a for the 08 km EL cases.

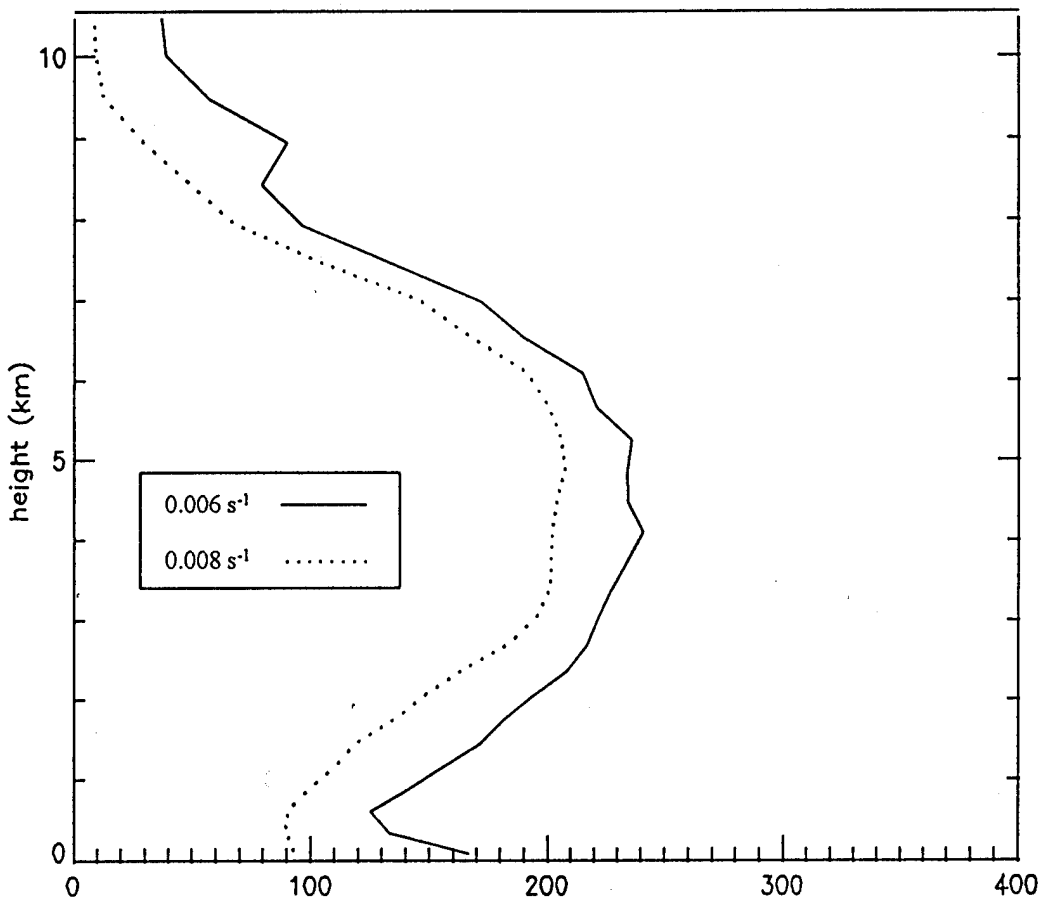

FIG. 17c. Same as FIG. 17a for the 07 km EL cases.

with increasing CAPE as well which reflects the maximum updraft velocities occurring within the storms. Mesocyclone heights and magnitudes for storms having the same CAPE show little sensitivity to variations in environmental shear. Interestingly, Figs. 17a-c also show that vertical vorticity magnitudes between 1 km and 4 km are nearly the same regardless of shear magnitude or total CAPE. The production of a low-level mesocyclone is found only in the 0.006 s^{-1} shear cases. Brooks and Wilhelmson (1990) noted that low-level mesocyclones may not develop if the ambient shear is too strong. This is left for further discussion in Section 4.

In the following section, updraft forcing is evaluated in each of the 0.006 s^{-1} shear cases to see if the propagation and persistence of the low-topped supercells is fundamentally different from the deeper 12 km EL supercell case. A more detailed look at low-level mesocyclone development as well as a comparison of low-level vertical vorticity development between the 7 km EL, 0.006 s^{-1} and 0.008 s^{-1} cases will be discussed to examine why the higher shear cases did not produce a strong low-level mesocyclone. At the end of Section 4, a reformulation of a storm scale Richardson Number is proposed as an attempt to distinguish among the storm types created in these model simulations; namely multicells (0.004 s^{-1} shear cases), supercells with great tornadic potential (0.006 s^{-1} shear cases), and supercells with little tornadic potential (0.008 s^{-1} shear cases).

4. DISCUSSION

Rotunno and Klemp (1985) illustrated that vortex lines are constrained to remain on surfaces of constant equivalent potential temperature (with the simplifying assumptions of the Boussinesq approximation for density and no diffusion of vorticity - see Fig. 18). Tilting of vortex lines implies lifting of an equivalent potential temperature surface. This suggests that the source of positive vertical vorticity in supercells is from the lower layers of the atmosphere. They also found that supercell transverse propagation is a result of vertical rotation on the right flank of the updraft at mid-levels. Variations in updraft magnitude above the mid-levels may be of little importance in the dynamics controlling storm propagation and persistence because it has little impact on the production of mid-level rotation.

From this theory, it may be hypothesized that storms occurring within similar thermodynamic and wind profiles below the mid-levels will evolve and propagate similarly regardless of CAPE, or EL height. Differences among these storms result primarily from differences in water loading of the updraft and in rain distribution. Rotunno and Klemp (1985) showed that for numerically simulated supercells, transverse propagation and persistence are not necessarily dependent on precipitation; however, the production of strong low-level rotation is dependent on the rain induced cold pool. Therefore, differences in the precipitation amounts produced by each storm are expected to have only a small affect on storm propagation and longevity. The impact of differences in precipitation amounts on low-level mesocyclone production are unclear.

This section explores two features of tornadic supercells that the results in the previous section imply may be nearly invariant for environments with moderate low-level lapse rates in temperature and sufficient shear, but with different total CAPE's. They are the persistence and propagation of the updraft and the development of the low-level mesocyclone.

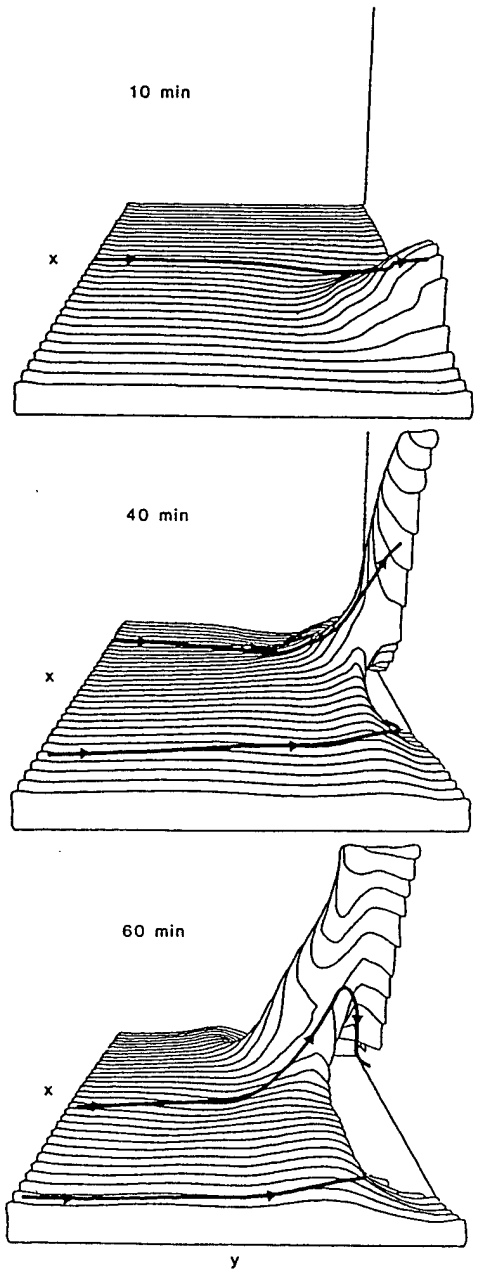

FIG. 18. Three-dimensional perspective (the view is westward) showing the contour θ_e = 336 K surface on a 30 X 20 X 9 km portion of the computational domain. The upward surging of the high-θ_e air reflects the updraft region. Vortex lines, denoted by heavy solid lines, lie approximately on the constant-θ_e surface owing to near conservation of the initially zero equivalent potential vorticity in the model. These vortex lines tilt upward on the south flank, producing a positive vertical component of the vorticity vector. As the updraft propagates to the south, low-θ_e air descends on the north flank. The vortex lines, adhering to the surface, tilt downward, producing a negative component of the vorticity vector on the north flank. The vertical scale is exaggerated by a factor of two. (Reprinted from Rotunno and Klemp 1985)

a. Updraft persistence and propagation

1) UPDRAFT FORCING

As in the work of McCaul and Weisman (1995), this study seeks to show how low-CAPE storms can produce low-level updrafts of comparable magnitude to high CAPE storms. Similar to the results noted in Section 3, they found the strength of the maximum updraft is correlated with the total CAPE of the sounding; however, the magnitude of the updraft in the lower levels is not correlated with the total CAPE but rather the buoyancy integrated to the level being examined. To understand the persistence, propagation and strength of the updraft, it is instructive to represent updraft forcing in terms of buoyancy and non-hydrostatic vertical pressure gradients. Following Weisman and Klemp (1984), the forcing terms in the Lagrangian derivative of the vertical wind (following the parcel) are divided into dynamic and buoyancy forcing (see appendix D):

$$\frac{dw}{dt} = \underbrace{-c_p\overline{\theta}_v\frac{\partial \pi_d}{\partial z}}_{\substack{dynamic\\ forcing}} \underbrace{-\left(c_p\overline{\theta}_v\frac{\partial \pi_b}{\partial z} - B\right)}_{\substack{buoyancy\\ forcing}} \tag{4}$$

Using this decomposition, a pressure associated with the respective dynamic and buoyant forcing terms may be extracted from the Boussinesq-Poisson relationships:

$$\begin{aligned} \vec{\nabla}\bullet c_p\overline{\rho}\overline{\theta}_v\vec{\nabla}\pi_d &= -\vec{\nabla}\bullet\left(\overline{\rho}\vec{V}\bullet\vec{\nabla}\vec{V}\right) \\ \vec{\nabla}\bullet c_p\overline{\rho}\overline{\theta}_v\vec{\nabla}\pi_b &= \frac{\partial\overline{\rho}B}{\partial z} \end{aligned} \tag{5}$$

Turbulence is ignored in equations (4) and (5). Rotunno and Klemp (1985) showed that in modeled supercells, maximum updraft forcing is generally concentrated in the storm's

inflow. They also showed that maximum values of dynamic forcing due to dynamically induced vertical pressure gradients coincide more closely to contours of total updraft forcing than do maxima in forcing due to buoyancy. This indicates the dynamically induced vertical pressure gradient forces play a larger role in propagating the updraft than does buoyancy.

2) TRAJECTORY ANALYSIS

To investigate the dynamics of the updraft in more detail, a trajectory analysis is performed on the core of the updraft of the 0.006 s^{-1} shear storms similar to that done by McCaul and Weisman (1995) and Weisman and Klemp (1984). The analysis is executed in three parts. First, the trajectories are calculated by interpolating the velocity fields in time and space. After the trajectories are calculated, the two terms on the RHS of Eq. (5) are interpolated along those same trajectories. Finally, the magnitudes of the forcing terms are integrated over time to produce the net contribution to the updraft velocity from each term in Eq. (6).

$$w \approx \int \frac{dw}{dt} Dt = -\int \underbrace{c_p \overline{\theta}_v \frac{\partial \pi_d}{\partial z}}_{\substack{dynamic \\ forcing}} Dt - \int \underbrace{\left(c_p \overline{\theta}_v \frac{\partial \pi_b}{\partial z} - B \right)}_{\substack{buoyancy \\ forcing}} Dt + w_0 \qquad (6)$$

A trajectory path is representative of the path a neutrally buoyant, massless, inertialess parcel would take if it were to move with the flow. The trajectories are calculated using model data saved at five minute intervals. Parcel positions are interpolated every 6 seconds over each five minute interval in place of using model data saved at that temporal resolution to conserve computer resources. The trajectories are calculated over a one hour time period between 1.5 hours and 2.5 hours using the trapezoidal method of integration for each 6 second interval. Using the technique employed by McCaul and Weisman (1995), the focus

of the trajectories is a 1.5 km wide ring centered at the maximum updraft magnitude at 1.5 km AGL at 120 minutes (shown in Figs. 19a-c). The ring represents 10 evenly spaced parcels. Trajectories are calculated backward in time from 120 minutes to 90 minutes, and forward in time from 120 minutes to 150 minutes.

The paths followed by all ten trajectories for each storm are given in Fig. 20. In all three cases, the updraft parcels originate southeast of the storm, enter the updraft, and exit out the top of the storm toward the east. The maximum trajectory height increases with CAPE. The higher CAPE storms also show larger wavelike perturbations at the top of the storm. This may be a result of the updraft parcels having larger vertical velocities impinging against the stable layer at the top of the storm, or from the effects of water loading in the deeper storms.

Figures 21a-c depict plots of the integrated forcing terms as well as the magnitude of the vertical wind following the trajectory for each of the 0.006 s^{-1} shear storms. These plots are representative of those trajectories traversing through the greatest depth of the updraft. Contributions to the vertical wind before the parcel enters the updraft, and those after the vertical wind becomes zero at the top of the storm are ignored. This was to draw a relationship between forcing terms and vertical wind magnitudes only within the updraft. The trajectory plots reveal results which are expected of mature supercell updrafts, however, some striking similarities among the cases are also found. Weisman and Klemp (1984) noted in their numerical analysis of multicells and supercells that supercells exhibit strong dynamic forcing in the updraft which contributes to the updraft's persistence and to the storm's deviate propagation. Within the 0.006 s^{-1} shear storm cases, the parcels do indeed show dynamic forcing as the major contributor to updraft intensities particularly in the low levels. It is also apparent that the vertical distribution of the integrated updraft forcing terms in Eq. (6) are nearly identical below 5 km for these three cases.

Table 3 compares data obtained from trajectories within the updraft in each storm. The table shows that the maximum updraft velocity, the height of the maximum updraft

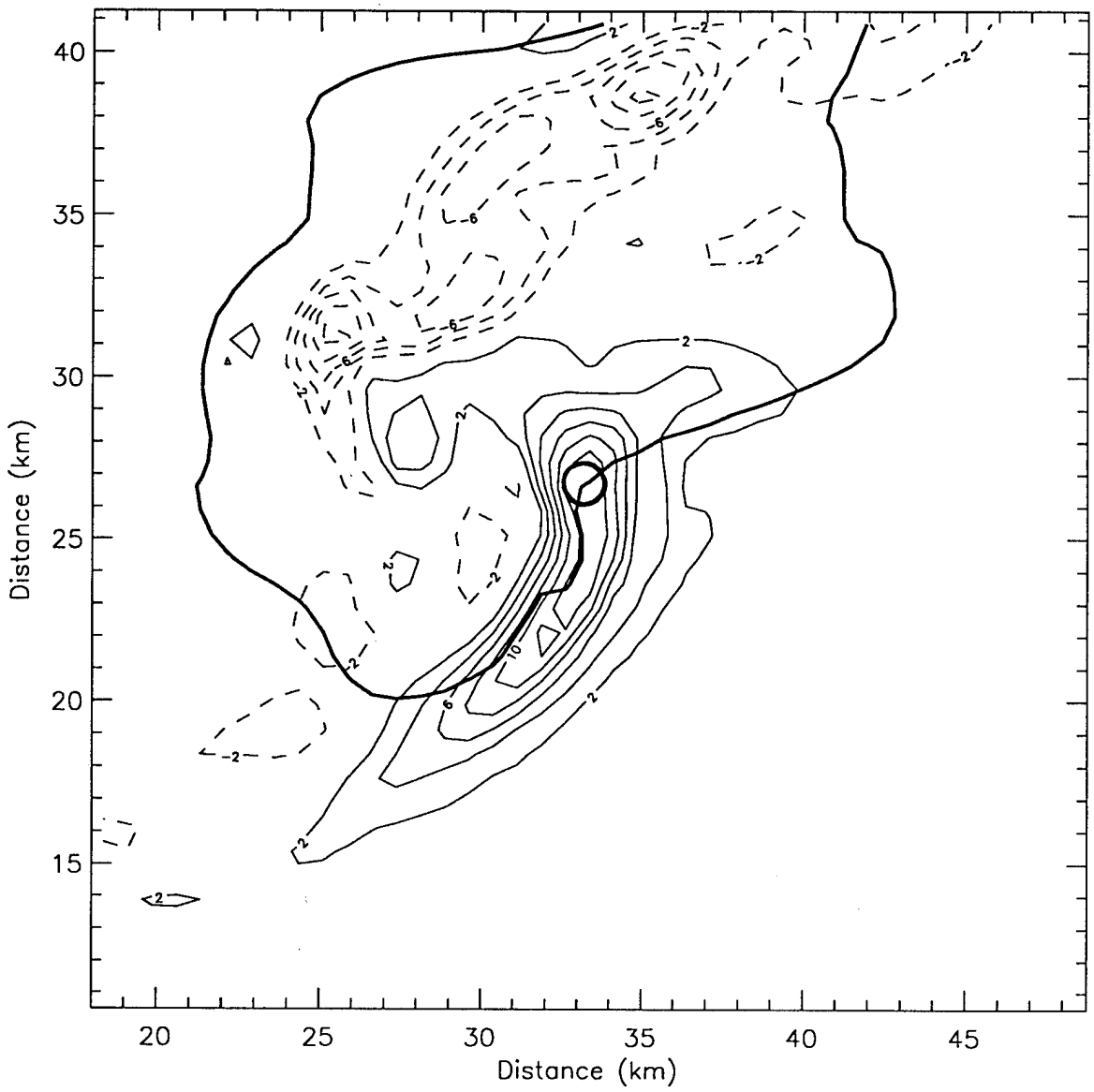

FIG. 19a. Vertical wind speed (contour interval of 2 m s^{-1}) at 1500 m AGL and surface rain region (marked by contour of q_r = 0.25 g kg^{-1}) for the 12 km EL, 0.006 s^{-1} shear case at 90 minutes. Position of trajectory focus identified by 1500 m wide ring at the location of maximum updraft speed.

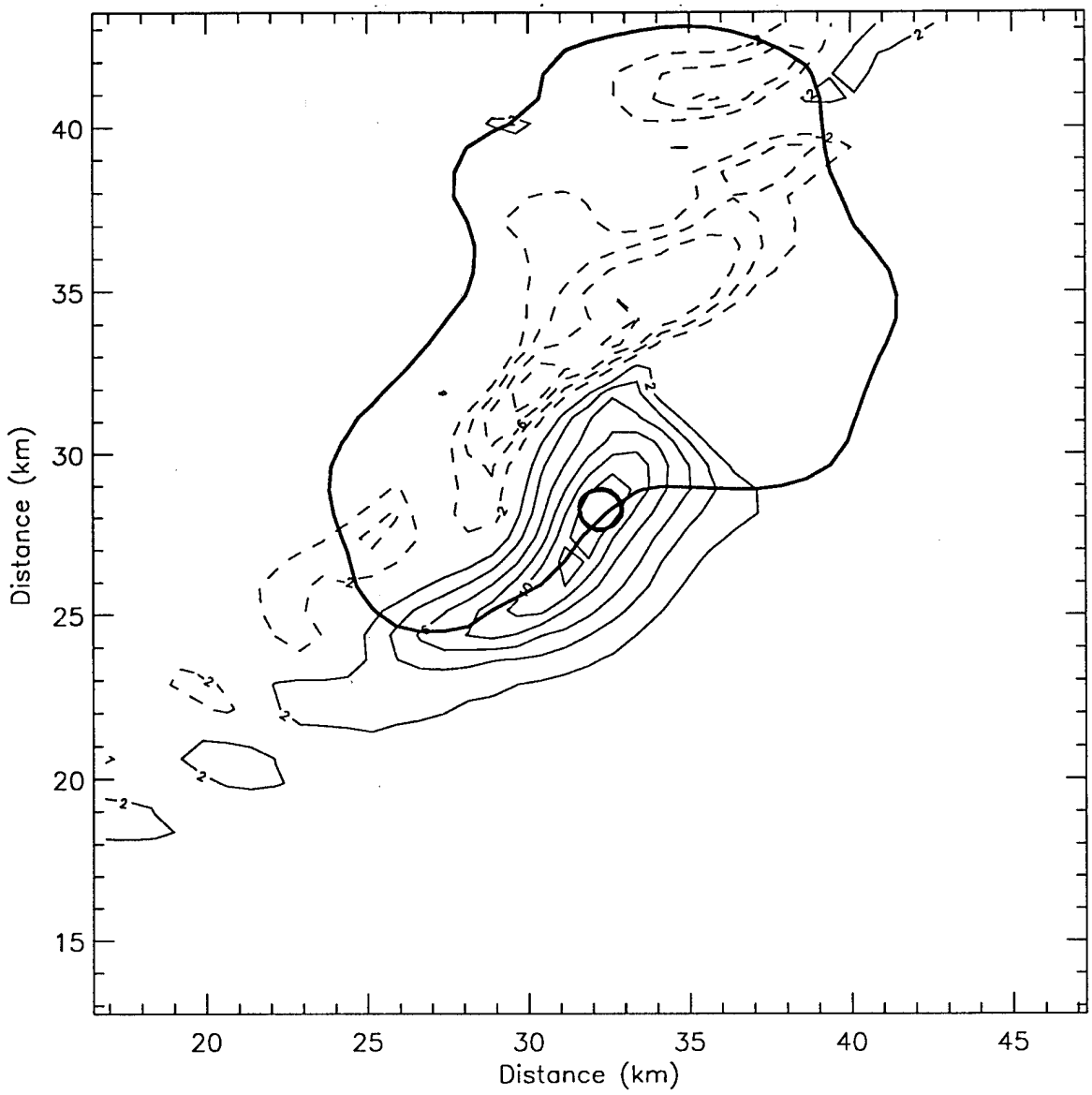

FIG. 19b. Same as FIG. 19a for the 08 km EL case.

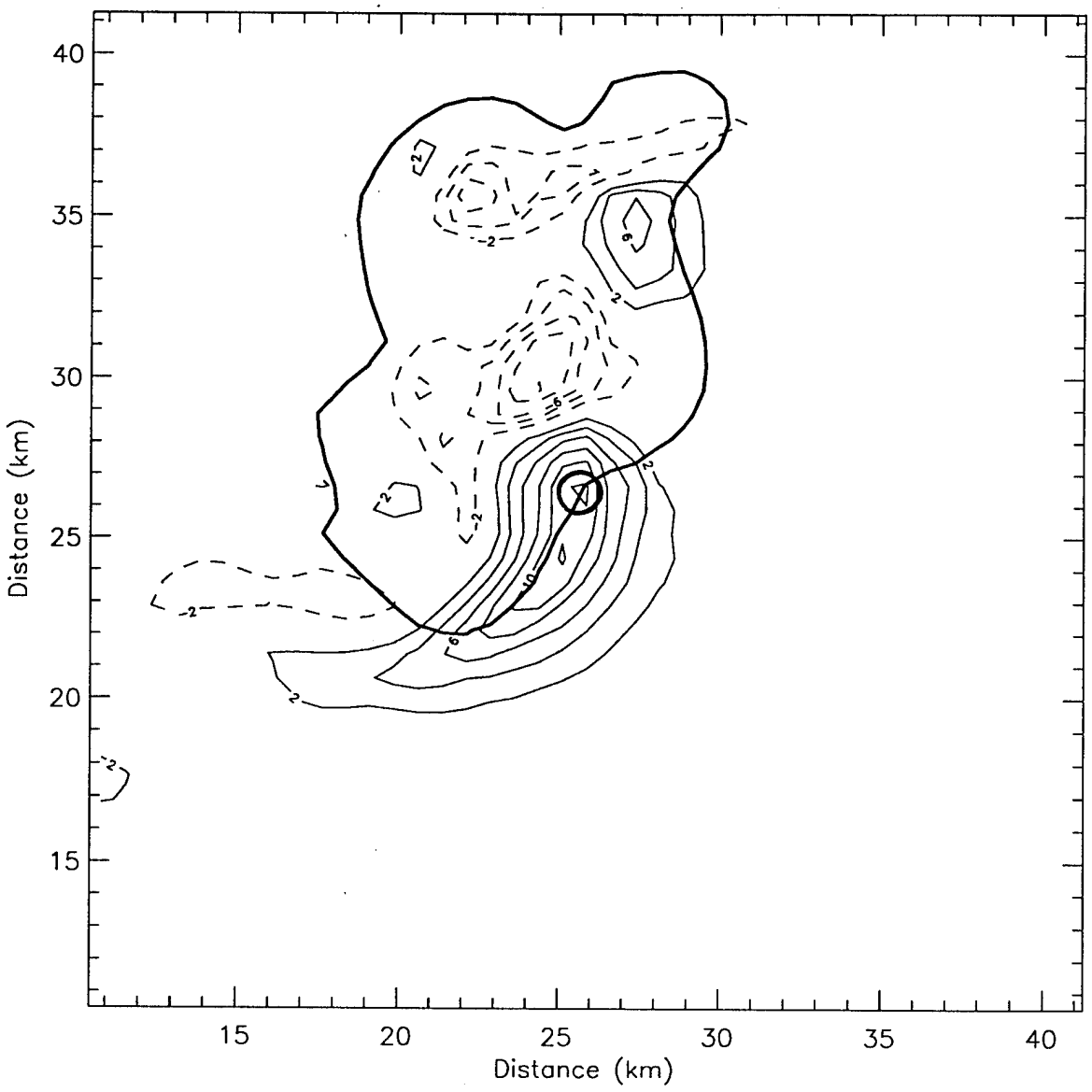

FIG. 19c. Same as FIG. 19a for the 07 km EL case.

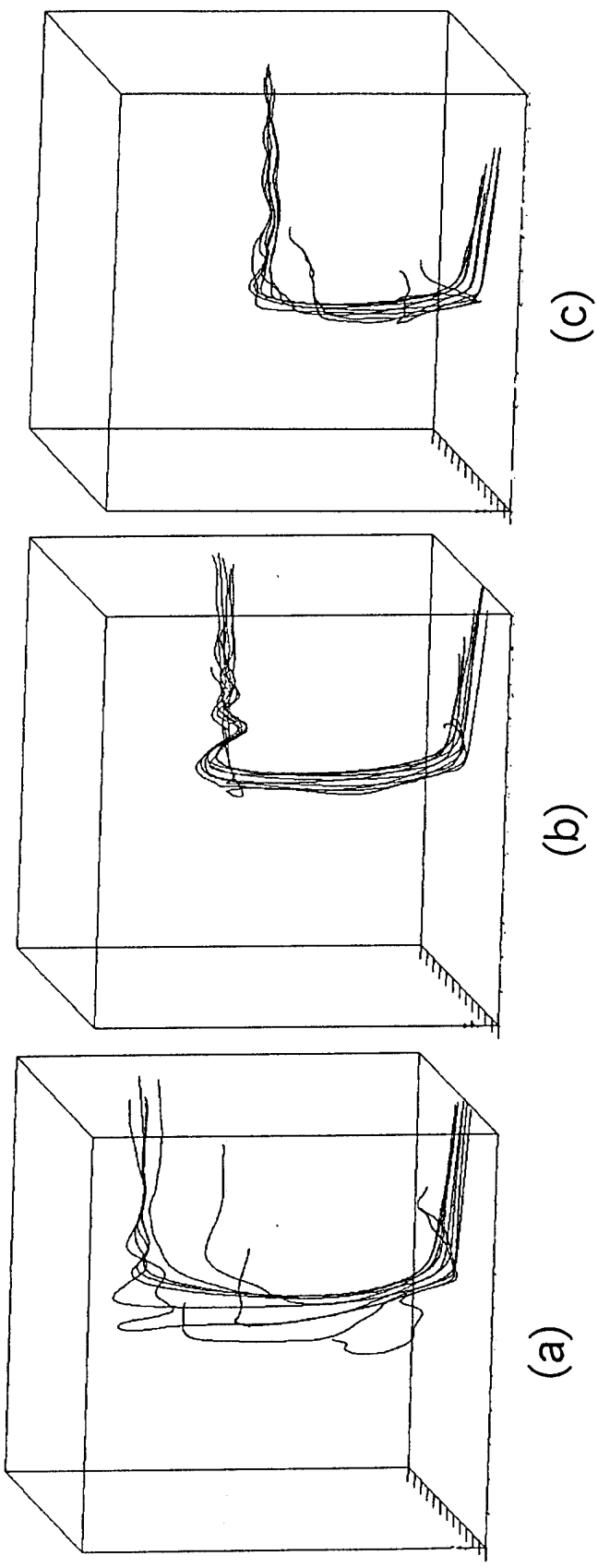

FIG. 20. Trajectory paths traced by the 10 trajectories in each of the 0.006 s^{-1} shear cases between 1.5 hours and 2.5 hours. View is from the southeast. Domain dimensions are 60 km horizontally and 15 km vertically. (a) is for the 12 km EL case, (b) is for the 08 km EL case, and (c) is for the 07 km EL case.

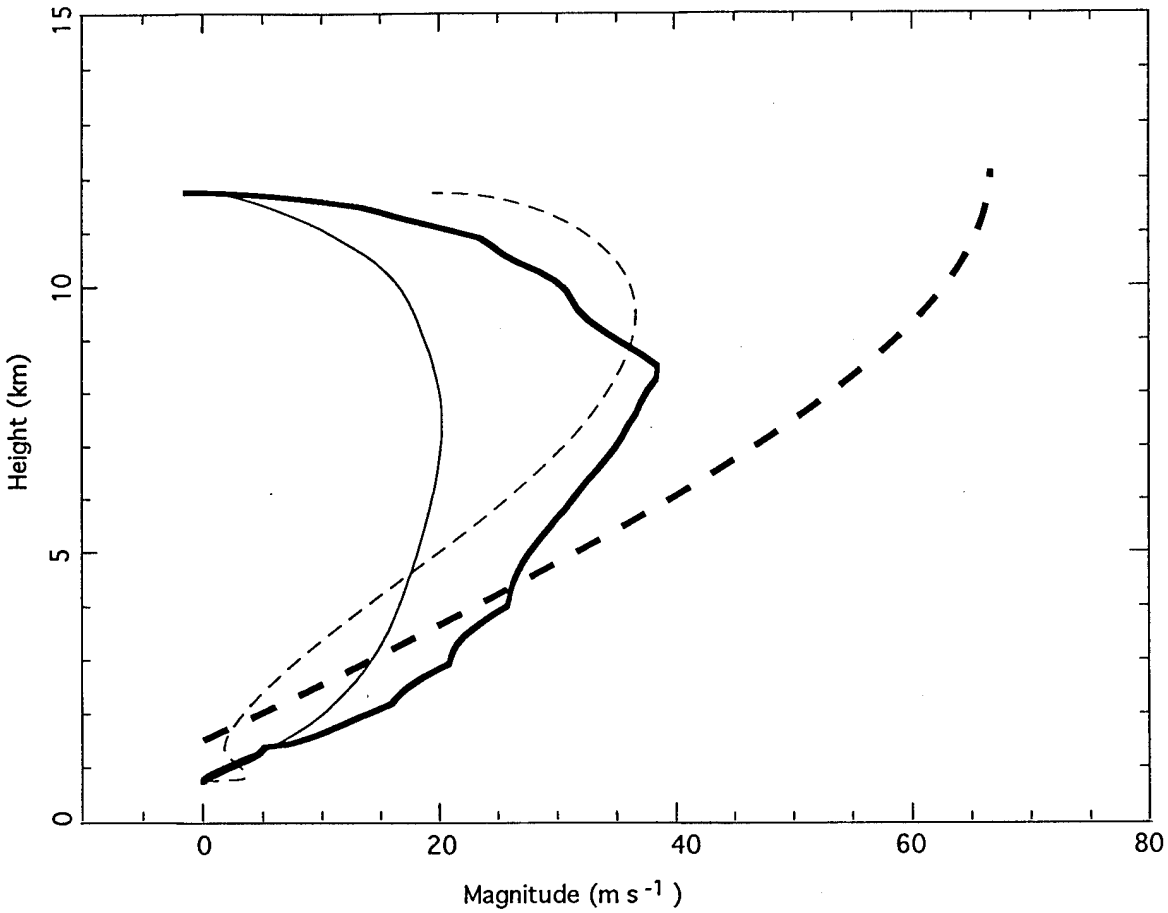

FIG. 21a. Plot of integrated updraft forcing along representative trajectory paths within the updraft of the 12 km EL case. Thick solid line represents vertical wind speed measured along the trajectory. Thin solid line represents time integrated dynamic forcing measured along the trajectory. Thin dashed line represents time integrated buoyancy forcing (including buoyancy and vertical pressure gradients due to vertical gradients of buoyancy). Thick dashed line represents theoretical (vertically integrated buoyancy used in CAPE computation) vertical wind speeds.

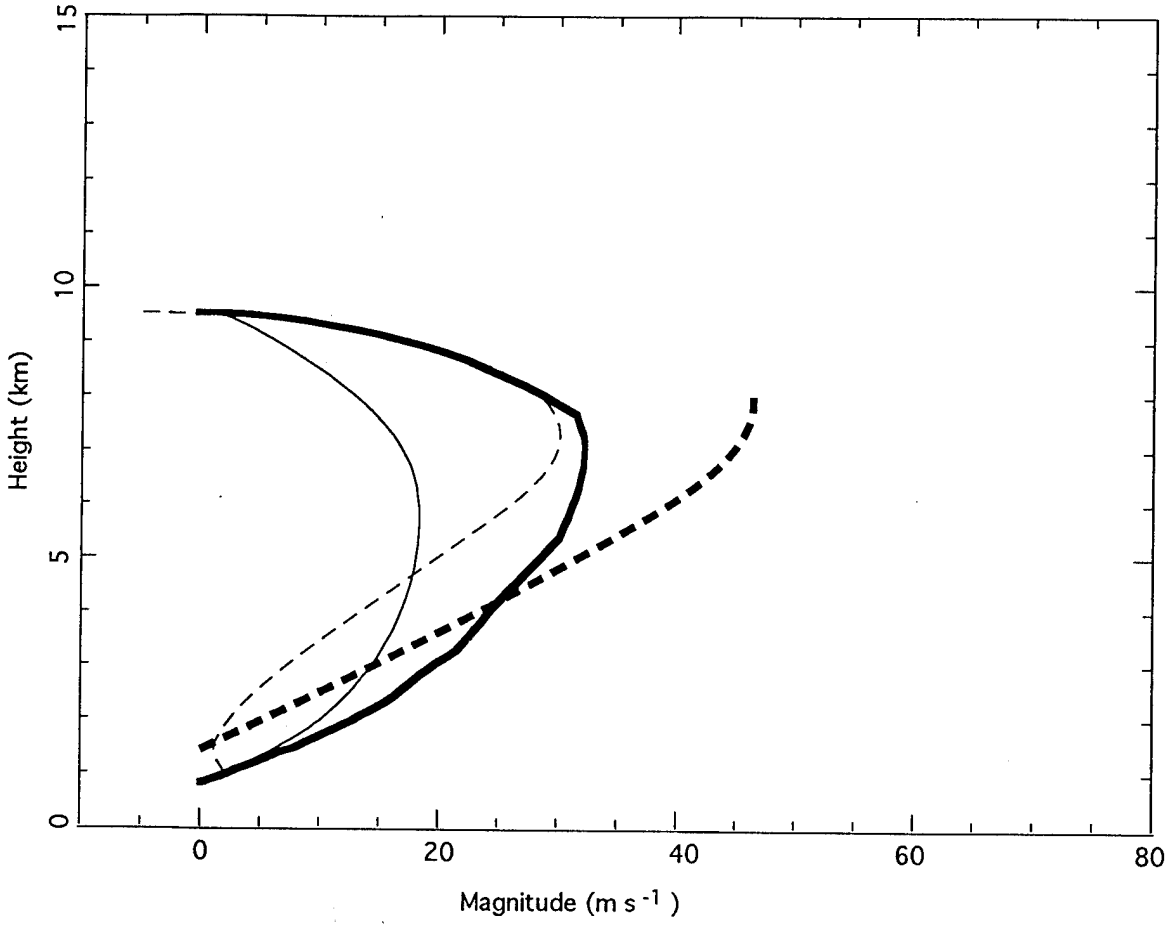

FIG. 21b. Same as FIG. 21a. for the 08 km EL case.

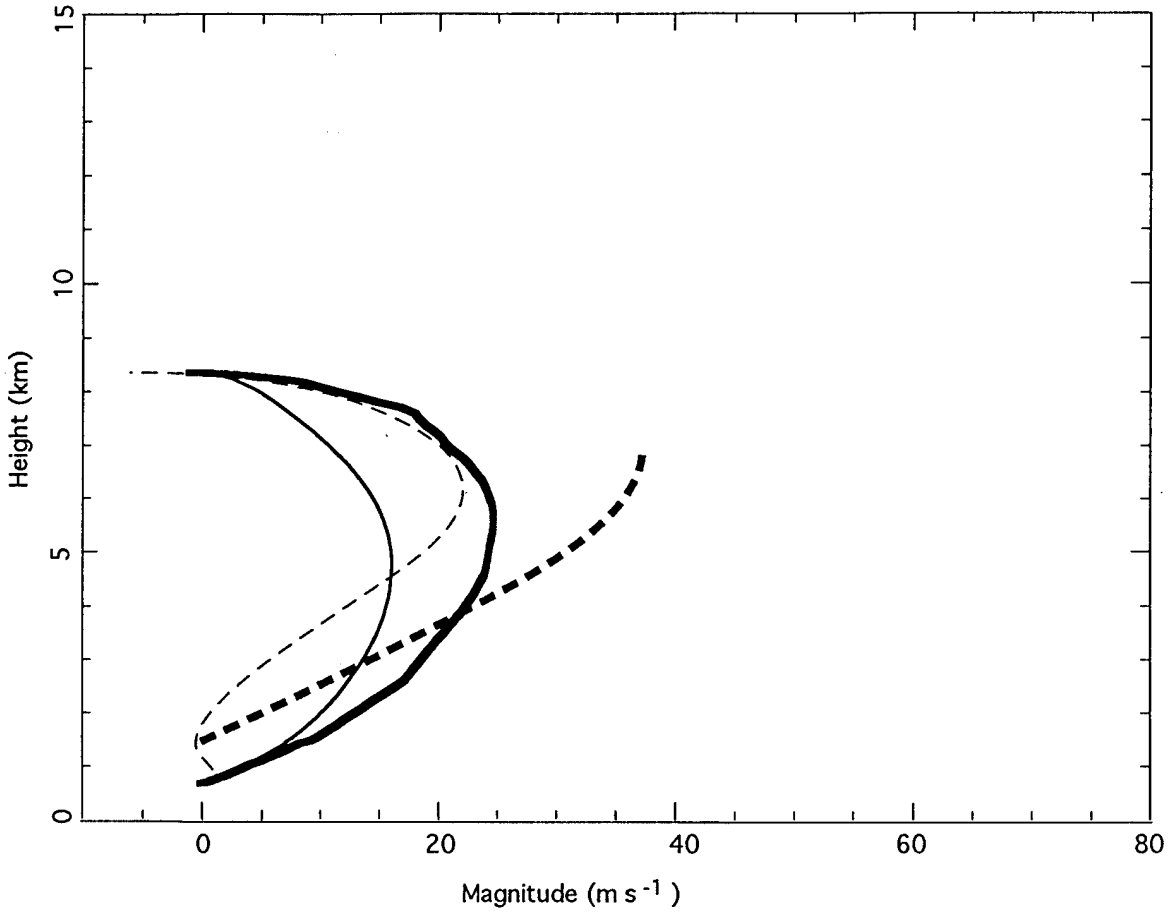

FIG. 21c. Same as FIG. 21a. for the 07 km EL case.

velocity, and the maximum height of the updraft are stratified by the total CAPE of each storm environment as expected. As total CAPE increases, the depth of the updraft and its maximum magnitude increase. A striking result, however, is the narrow range of values found for the height at which dynamic forcing contributes equally with buoyancy forcing to the updraft, and for the magnitude of the updraft forcing terms at that level. McCaul and Weisman's (1995) intercomparison of storm updraft dynamics between observed low-topped supercells from land-falling hurricanes and Great Plains supercells similarly found that updraft magnitudes at low levels are comparable even though maximum updraft aloft varies greatly among the storms. The height at which dynamics and buoyancy influence the updraft equally varies less than a kilometer among the three 0.006 s^{-1} shear storms. Additionally, the magnitude of the updraft at these levels varies only about 5 m s^{-1} among the three storms. These three storms have nearly identical forcing characteristics in the updraft below the 5 km level. In all three storms, dynamic forcing dominates the updraft below the mid-levels to the same degree. In one respect, this is to be expected because the low level environmental wind and buoyancy profiles are the same for the three cases. However, the similarity of the updraft forcing in the mature phase of each storm's evolution qualitatively implies the buoyancy profile above the mid-levels has little impact on storm persistence and propagation.

TABLE 3. Updraft characteristics for the three 0.006 s^{-1} shear cases taken from a representative updraft trajectory in each case.

	12 km EL	08 km EL	07 km EL
Maximum Updraft	37 m s^{-1}	31 m s^{-1}	24 m s^{-1}
Height of Maximum Updraft	8.0 km	6.8 km	4.5 km
Maximum Height of Updraft	11.7 km	9.4 km	7.9 km
Height of Equal Forcing Between Terms	5.1 km	4.3 km	4.5 km
Updraft at Height of Equal Forcing	28 m s^{-1}	26 m s^{-1}	23 m s^{-1}

b. Low-level mesocyclones

1) PRODUCTION OF VERTICAL VORTICITY

All of the 0.008 s^{-1} and 0.006 s^{-1} shear simulations produce storms with a persistent updraft and strong vertical rotation at mid-levels of the storms relative to the EL. The primary objective of this study is to identify characteristics of the environment conducive to the development of severe low-topped supercells. So far, some environmental buoyancy and wind shear characteristics have been identified which may lead to low-topped supercell development. With this in mind, attention is now turned to the development of the near-surface mesocyclones which occurred in the 0.006 s^{-1} shear model simulations. While the resolution of the model is too course to capture the dynamics associated with tornadogenesis, an analysis of surface mesocyclone development can contribute useful information about observed parent tornado mesocyclones.

To gain a better understanding of how strong vertical vorticity is produced near the surface, the various sources of vertical vorticity are first qualitatively examined. The local production of vertical vorticity may be modeled with the following form of the inviscid vertical vorticity equation.

$$\frac{d\zeta}{dt} = \vec{\omega}_H \bullet \vec{\nabla}_H w + \zeta \frac{\partial w}{\partial z} \tag{7}$$

where ζ is the vertical component of the total vorticity $\vec{\omega}$

$\vec{\omega}_H$ is the horizontal vector component of the total vorticity $\vec{\omega}$

$\vec{\nabla}_H$ is the horizontal gradient vector

The first term on the rhs of Eq. (7) represents tilting of horizontal vorticity by the vertical component of the wind. The second term represents vertical stretching or compression of vertical vorticity by vertical gradients of the vertical wind. Thus vertical

vorticity develops as a result of tilting and stretching pre-existing vorticity. Contributions from planetary vorticity (Coriolis force), and turbulent mixing are ignored in the formulation. Vertical shear in the pre-storm environment is generally present because of the thermal wind arising from the large scale synoptic environment. This vertical shear is the source of the ambient horizontal vorticity for the storms. After the storms mature and precipitation begins to influence horizontal temperature gradients, horizontal vorticity is further generated baroclinically at low levels.

The equation approximating vorticity forcing is

$$\frac{d\vec{\omega}}{dt} = \left(\vec{\omega} \bullet \vec{\nabla}\right)\vec{V} + \vec{\nabla} \times B\hat{k} \tag{8}$$

which indicates vorticity is changed by reorienting and stretching the vortex lines, and by solenoidal generation. The solenoidal term $\vec{\nabla} \times B\hat{k}$ is geometrically represented by a vector pointing right of the horizontal buoyancy gradient and parallel to contours of constant buoyancy. The horizontal vector component of the total vorticity may then be represented as the sum of vertical vorticity resulting from the effects of vertical wind shear and horizontal gradients in potential temperature.

$$\vec{\omega}_H = \vec{\omega}_e + \vec{\omega}_\theta \tag{9}$$

where $\vec{\omega}_e = \int \left(\vec{\nabla} \times B\hat{k}\right) dt + \vec{\omega}_{e_0}$

and $$\frac{d\zeta}{dt} = \underbrace{\vec{\omega}_e \bullet \vec{\nabla}_H w}_{\substack{barotropic \\ tilting}} + \underbrace{\vec{\omega}_\theta \bullet \vec{\nabla}_H w}_{\substack{baroclinic \\ tilting}} + \underbrace{\zeta \frac{\partial w}{\partial z}}_{stretching} \tag{10}$$

With the gross assumption that $\bar{\omega}_e$ is constant among the cases since the shear profiles are all constant at 0.006 s^{-1}, we are motivated to reexamine how the updraft magnitude varies among the cases.

It is apparent from the vertical distribution of the time-averaged updraft in Figs. 14a-c that the magnitude of the updraft varies little in the low levels. This is expected to some degree because the environmental buoyancy profiles below 600 mb are exactly the same among the cases. The scale of the horizontal gradient of vertical wind among the 0.006 s^{-1} shear cases is roughly the same with a magnitude of 3.5 m s^{-1} per 2 km. To a gross approximation then, we may ignore the differences among the cases arising in the barotropic and stretching terms of the above vertical vorticity equation.

Rotunno and Klemp (1985) found that the precipitation induced cold pool is primarily responsible for the development of vertical rotation in the low levels. This motivates a closer look at the baroclinic tilting term in Eq. (9) for each storm. It is assumed that if large differences in vertical vorticity production among the cases will occur, it will be due primarily to this production term. Rotunno and Klemp (1985) found low-level in-flowing parcels acquire baroclinically induced horizontal vorticity along the buoyancy gradient generated by the cool forward flank downdraft. The parcels are then tilted by the vertical wind gradient between the updraft and downdraft and advected into the updraft. Within the updraft, the newly generated vertical vorticity is then intensified through stretching.

The focus here is not to thoroughly investigate the many mechanisms thought to influence vertical vorticity production in the low-levels, but rather to compare the three simulation results in light of this theory of low-level mesocyclone development in supercells. As shown in Figs. 16a-c and Figs. 17a-c, these three cases are similar regardless of the total CAPE and EL height.

Figures 22a-c depict the updraft, the rainwater contours, and horizontal wind vectors for the three 0.006 s^{-1} shear storms at the time of maximum low-level rotation. This is at 130 minutes for the 7 km and 8 km EL storms, and at 135 minutes for the 12 km EL storm.

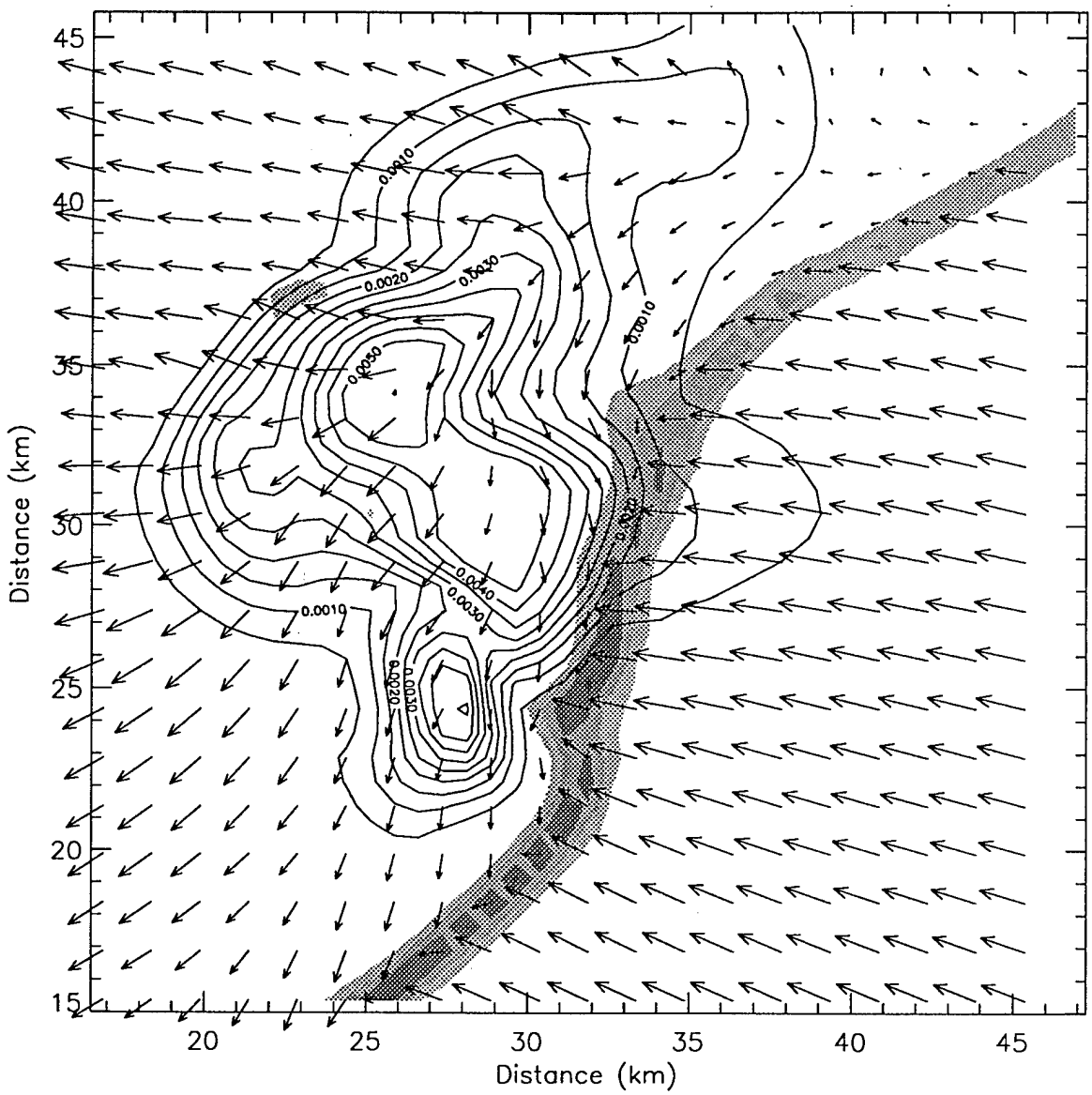

FIG. 22a. Rain region (contours of q_r at 0.5 g kg^{-1} interval), updraft (shaded at 1 m s^{-1} interval), and wind vectors (scale of vector is 1 km = 10 m s^{-1}) near the surface for the 12 km EL, 0.006 s^{-1} shear case at the time of maximum low-level vertical vorticity production (135 minutes).

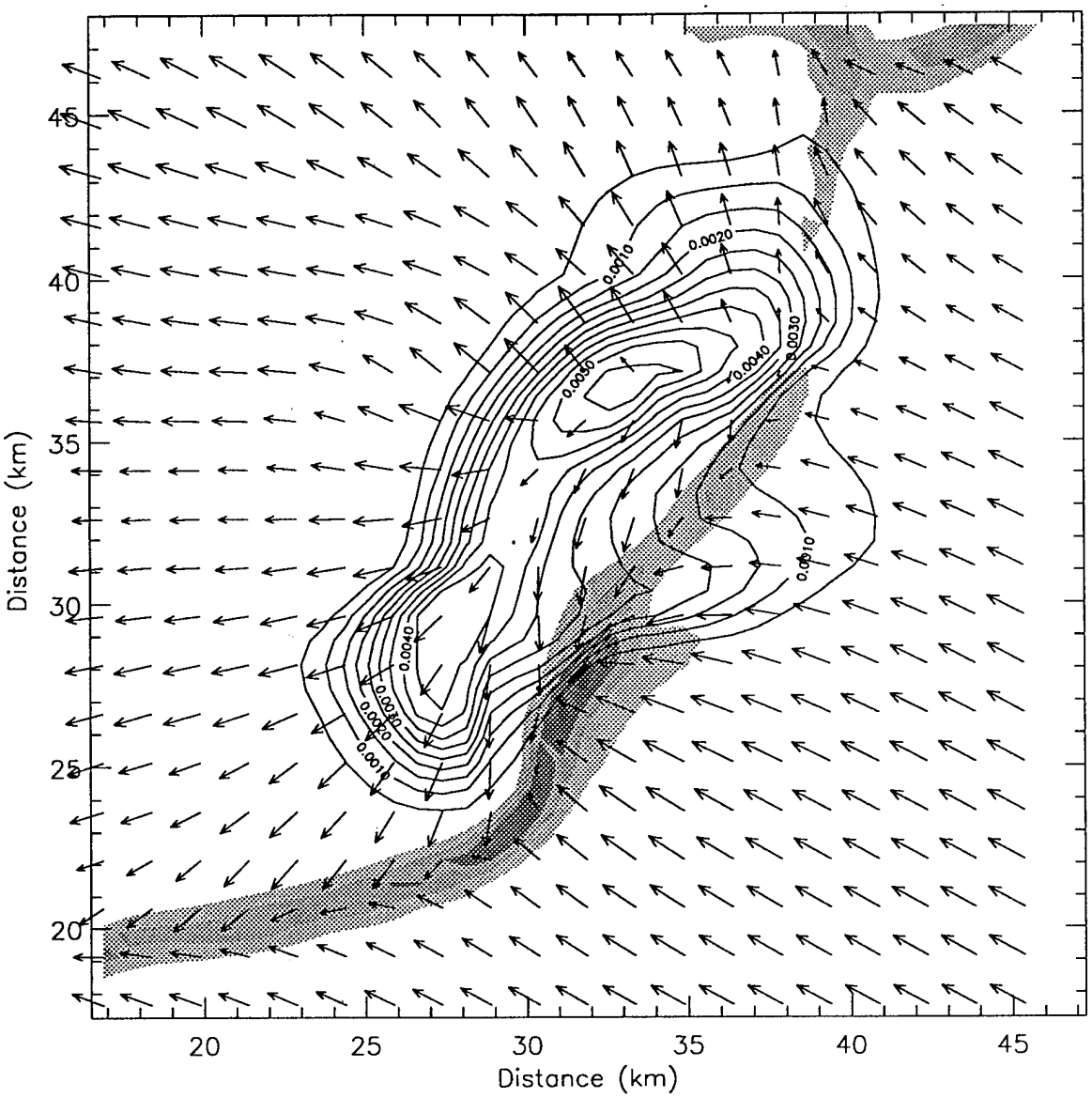

FIG. 22b. Same as FIG. 22a for the 08 km EL case at 130 minutes.

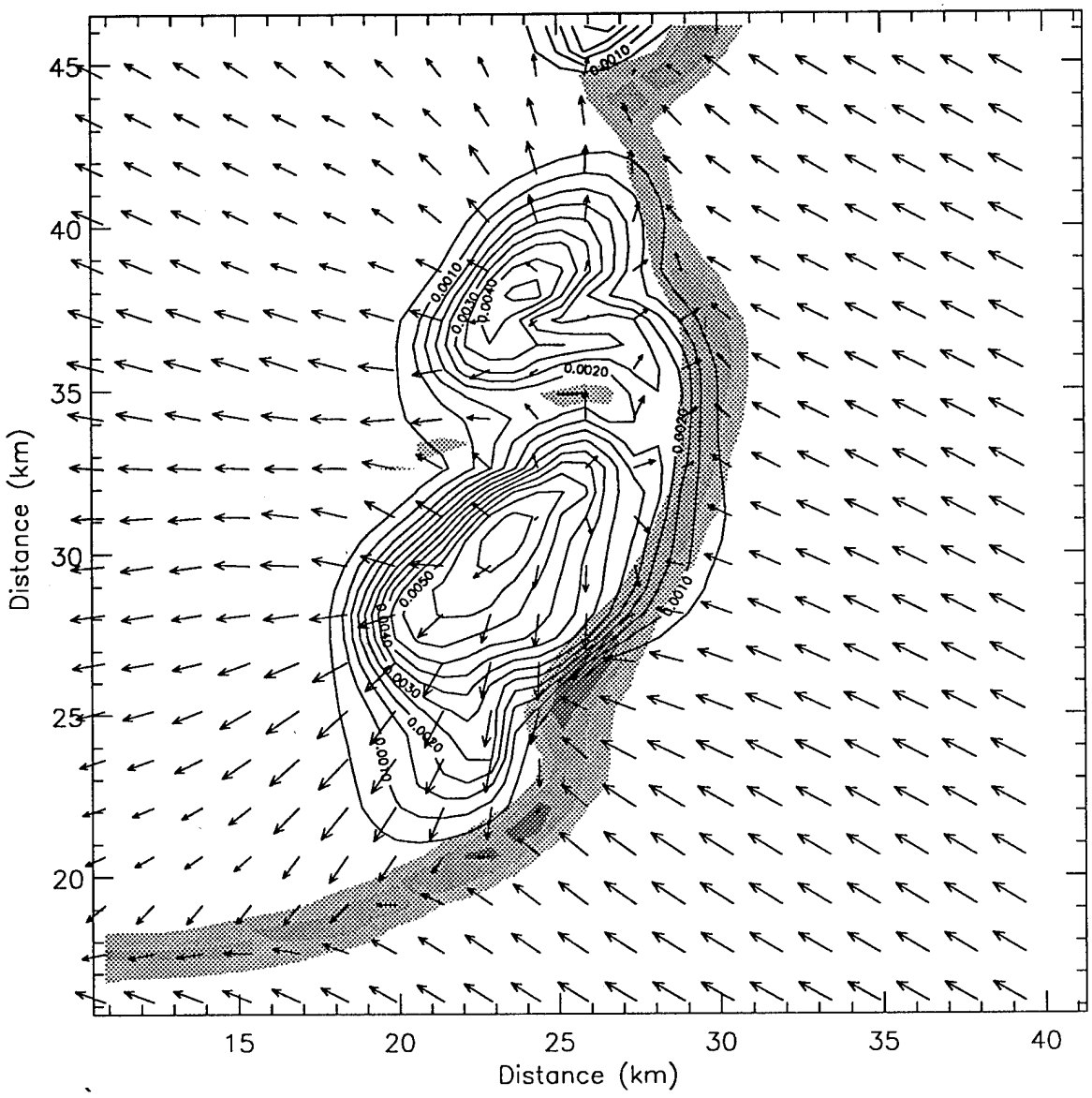

FIG. 22c. Same as FIG. 22a for the 07 km EL case at 130 minutes.

The maximum vertical vorticity is located just south of the maximum updraft in the notch of the rainfield and gustfront. These plots indicate the higher EL cases produced greater aerial coverage in precipitation and a forward flank precipitation region extending further east of the updraft than in the low EL case. Also, the divergent region below the maximum downdraft in the low EL case is much closer to the updraft than for the other two cases. The notch in the updraft and rain region is generally an indicator of rotational development.

To illustrate the process of low-level mesocyclone formation, Figs. 23a-c show the vertical vorticity contours, dashed buoyancy contours, and vectors representing horizontal vorticity and horizontal wind at the time of maximum vertical vorticity development at the lowest grid level. A comparison of the near surface vorticity and buoyancy fields among the three cases during these times shows several similarities.

As in Rotunno and Klemp (1985), and McCaul and Weisman (1995), the barotropically derived horizontal vorticity vectors are represented in the SE portion of the plot (Figs. 20a-c) in the undisturbed inflow region outside of any horizontal gradients in buoyancy. The magnitude of the barotropic horizontal vorticity is small and points northward. Large horizontal vorticity vectors are seen nearly parallel to the contours of buoyancy west of the updraft. This is due to the production of baroclinic horizontal vorticity (see appendix E for a more detailed discussion on the relationship between buoyancy gradients and vorticity). The buoyancy contours are tightly packed just west of the updraft. To the north of the updraft, the contours fan out beneath the rainy forward flank downdraft. This is more evident in the higher EL storms with rainfall falling further east. Since these figures show large horizontal vorticity vectors pointing in directions other than the barotropically generated vorticity vectors found in the southeast corner of the plots, and since these vectors are nearly parallel to the buoyancy contours and pointing right of the buoyancy gradient, we may assume these vorticity vectors are baroclinically generated.

A look at the horizontal wind vectors indicates the horizontal vorticity vectors from the northeast have a large component in the streamwise direction. As noted in the baroclinic

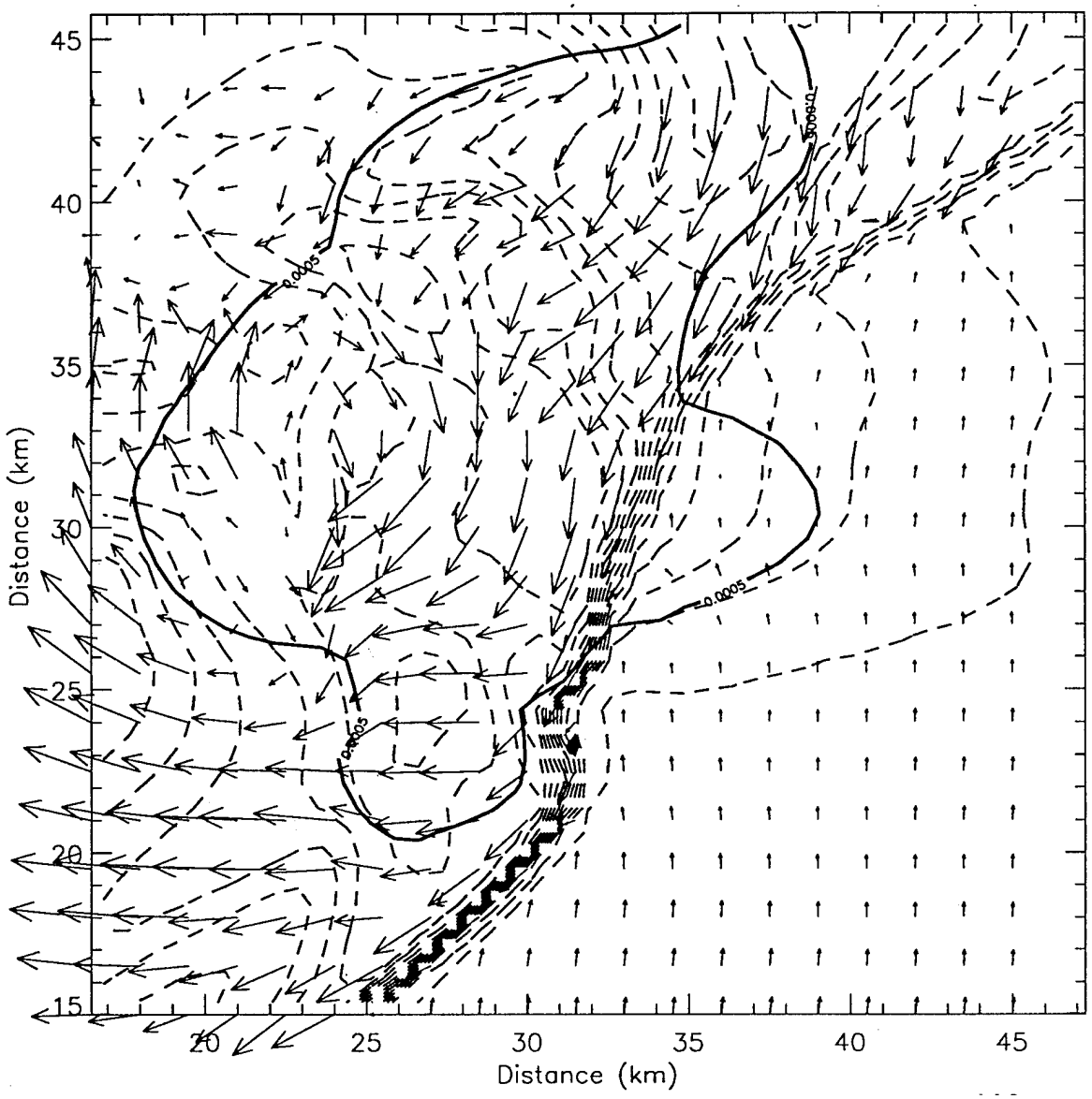

FIG. 23a. Surface rain region (marked by thick contour of $q_r = 0.5$ g kg^{-1}), buoyancy (thin dashed contours from -0.26 m s^{-2} to 0 at interval of 0.02 m s^{-2}), horizontal vorticity vectors (vector scale is 1 km = 0.005 s^{-1}), and position of mesocyclone (vertical vorticity > 0.02 s^{-1} marked by solid circle) for the 12 km EL, 0.006 s^{-1} shear case at 135 minutes.

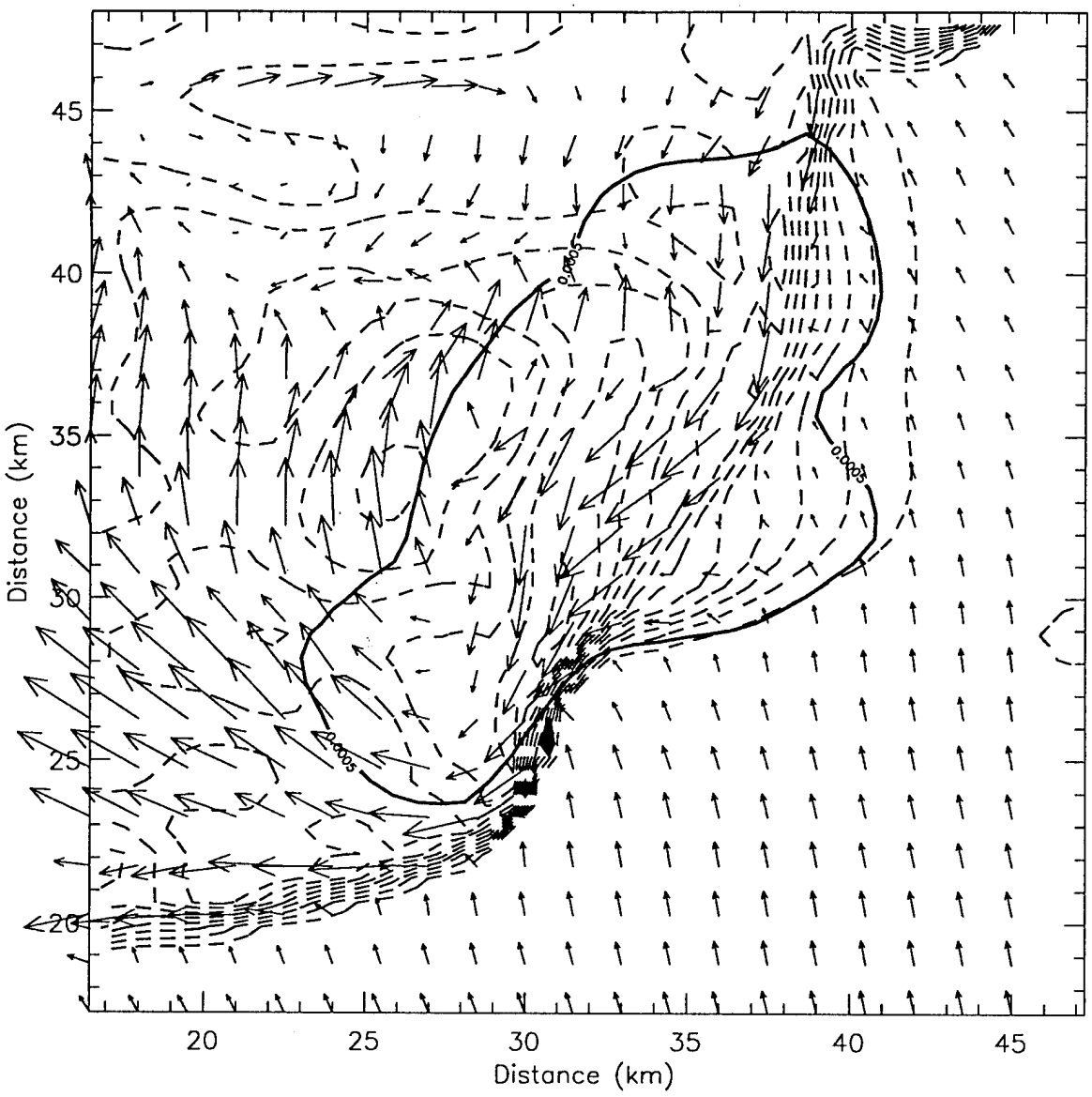

FIG. 23b. Same as FIG. 23a for the 08 km EL case at 130 minutes.

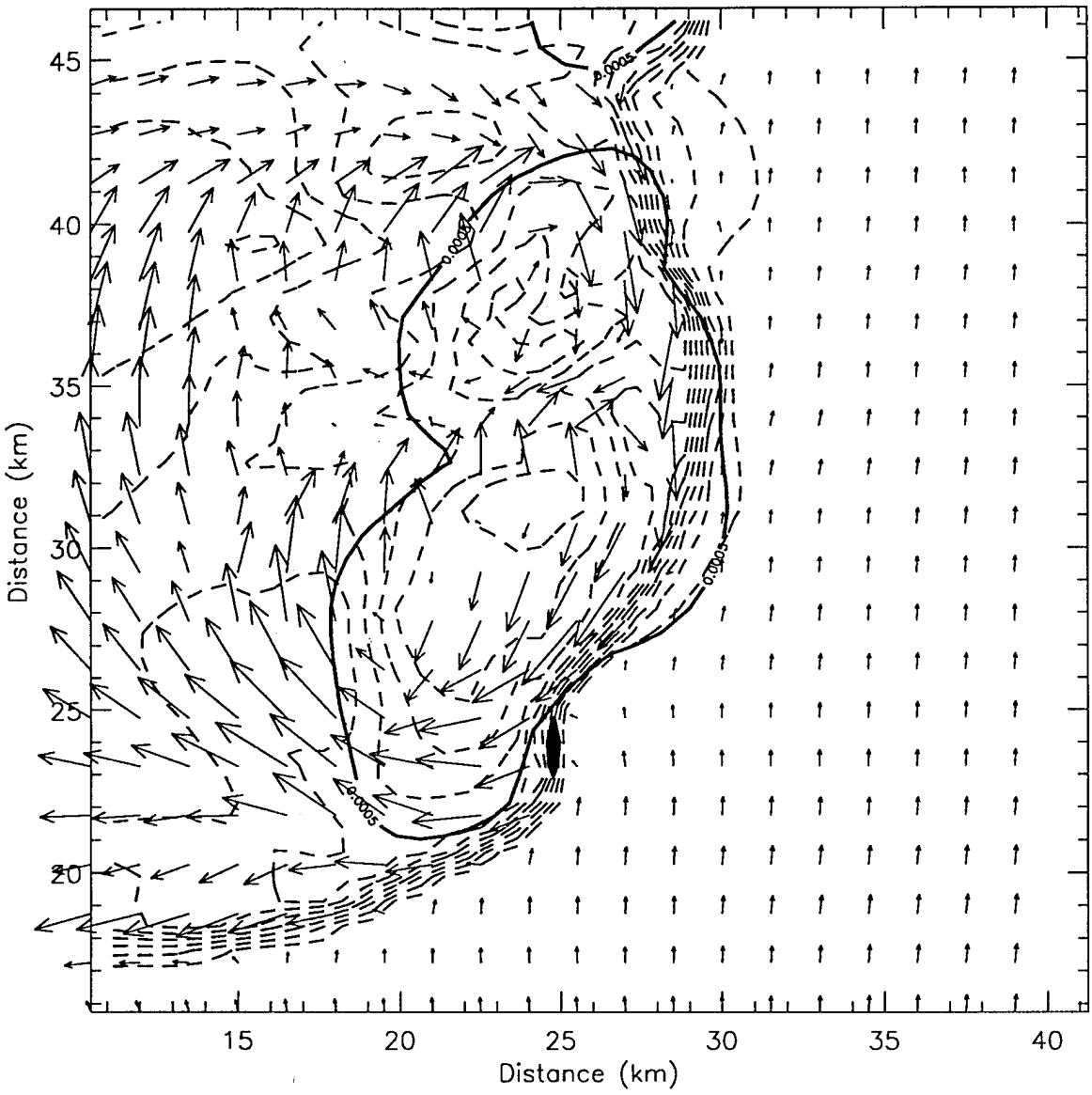

FIG. 23c. Same as FIG. 23a for the 07 km EL case at 130 minutes.

tilting term of Eq. (10), $\vec{\omega}_\theta \bullet \vec{\nabla}_H w$, those vorticity vectors pointing in the direction toward the updraft will have the greatest potential for generating vertical vorticity. These features are similar among all three 0.006 s^{-1} shear storms. The vertical vorticity magnitudes are nearly identical.

The strong horizontal vorticity north of the mesocyclone must be tilted to produce vertical vorticity. Plots of vertical vorticity magnitude, forcing from tilting and forcing from stretching over-plotted with shaded contours of the updraft for the 7 km EL case are shown in Figs. 24a-c. Maximum values of vorticity and stretching are positioned near the maximum updraft as expected; however, tilting contours tell a different story. In an environment characterized by barotropic horizontal vorticity only, tilting would be maximized on the south side of the maximum updraft.

The plots of vertical vorticity forcing from tilting show generally high positive values north through northwest of the updraft. A 30-minute trajectory path into the mesocyclone is over plotted in Figs. 24a-c. This path indicates parcels entering the mesocyclone have large components of vorticity pointing toward the south as they enter the updraft from the north. The contribution of barotropic vorticity parallel to the inflow from the south is smaller. These positive values are located in a region opposite what would be expected from tilting of the environmental horizontal vortex lines by the updraft. Large positive values northwest of the maximum updraft are generated from tilting the baroclinically produced horizontal vorticity by the updraft/downdraft gradient in the rainy region. Vertical vorticity produced in this manner is additionally advected toward the updraft.

2) COMPARISON BETWEEN HIGH SHEAR AND MODERATE SHEAR ENVIRONMENTS

Brooks, Doswell and Wilhelmson (1994) showed that supercell storms in environments with too much shear will not develop strong low-level mesocyclones. They attribute this partially to the orientation of the gust front. Figures 22c and 23c depict the 7 km EL, 0.006

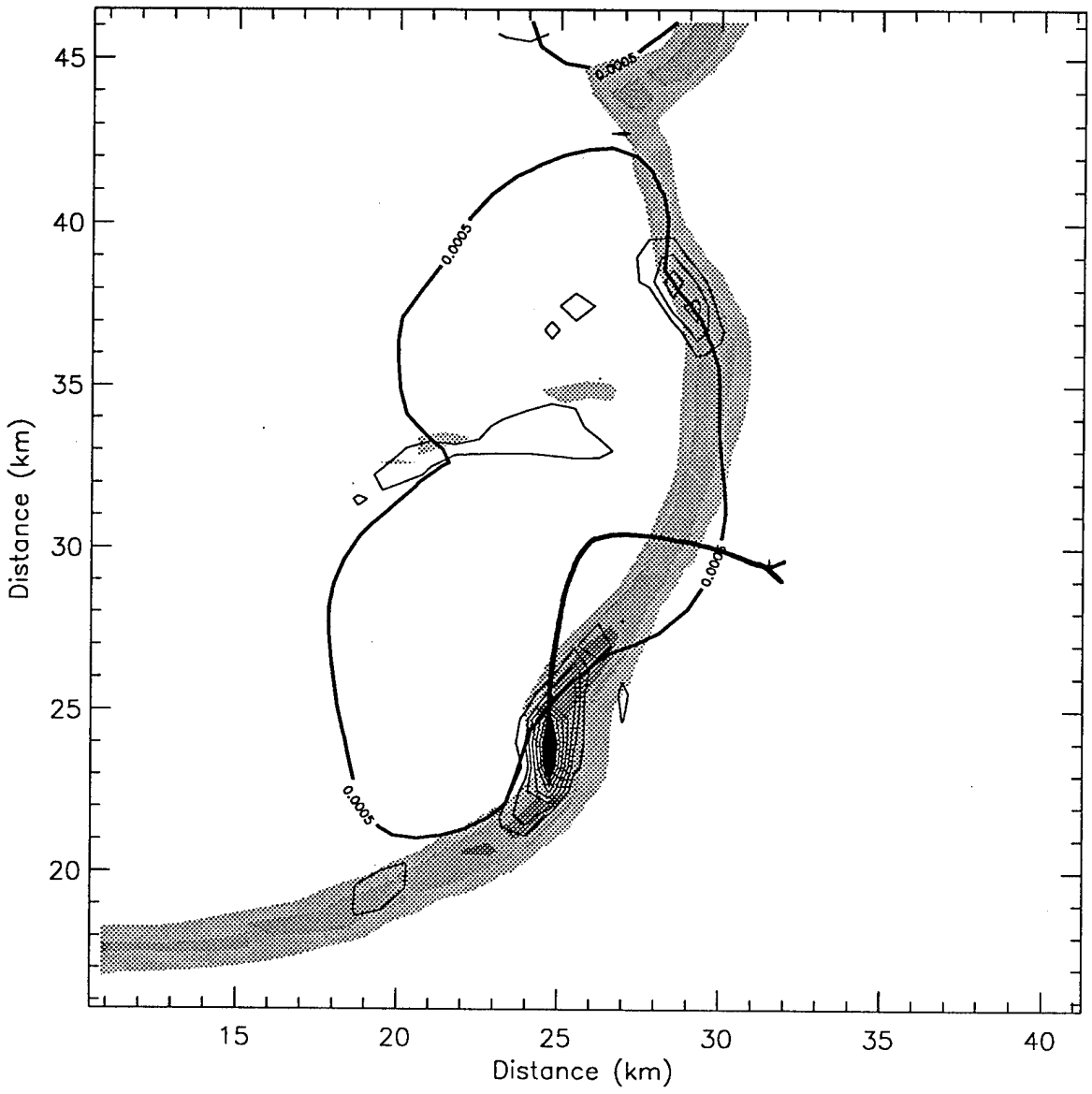

FIG. 24a. Surface rain region (solid contour of q_r = 0.5 g kg^{-1}), updraft (shaded at contour interval of 1 m s^{-1}), and positive vertical vorticity (ranging from 0 to 0.03 s^{-1} at contour interval of 0.003 s^{-1}) for the 7 km EL, 0.006 s^{-1} case at 130 minutes. Parcel trajectory over 30 minutes prior to the time of this plot is also shown (thick solid line).

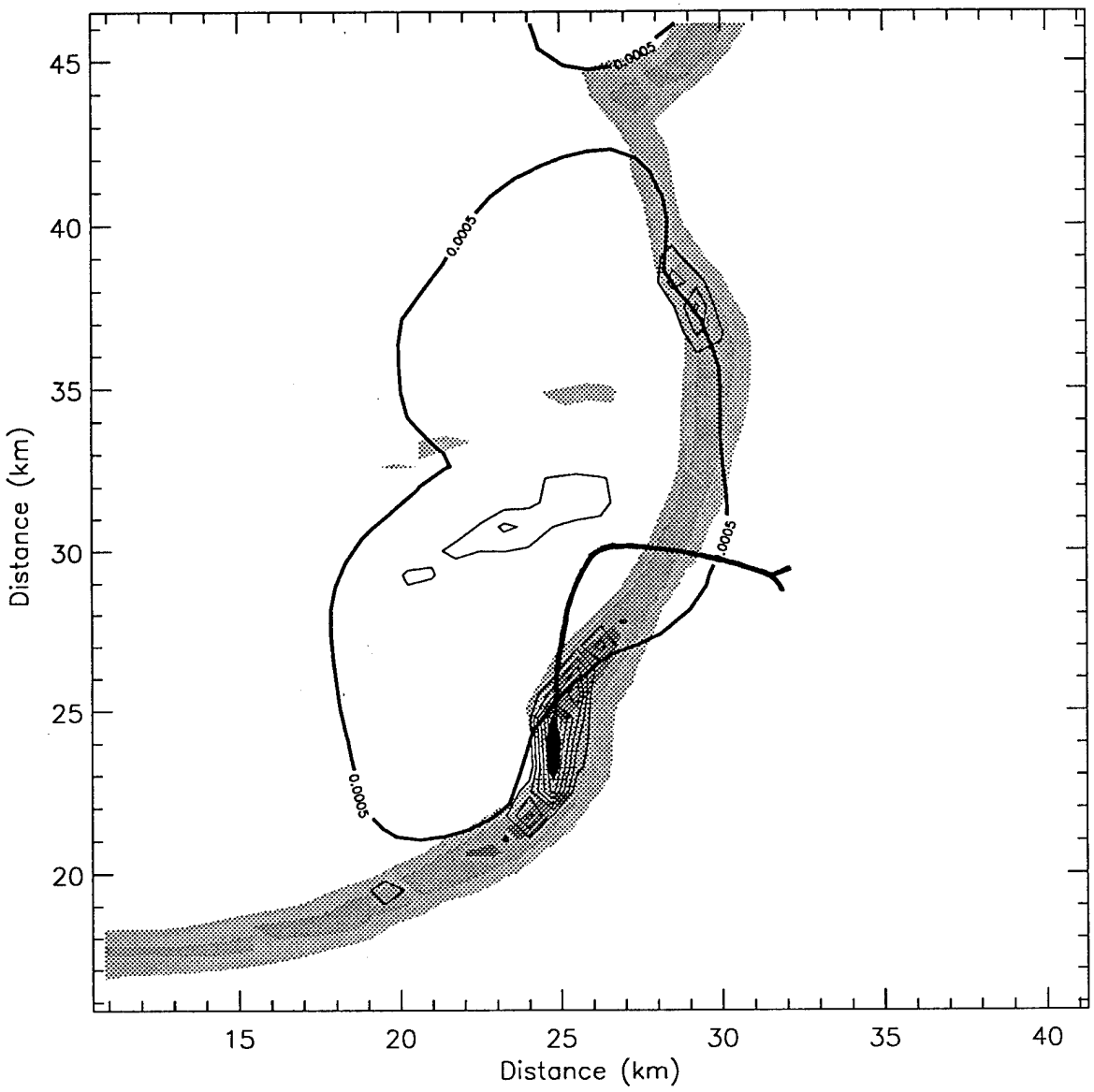

FIG. 24b. Same as FIG. 24a with vertical stretching (ranging from 0 to 0.021 s^{-2} at contour interval of 0.003 s^{-2}).

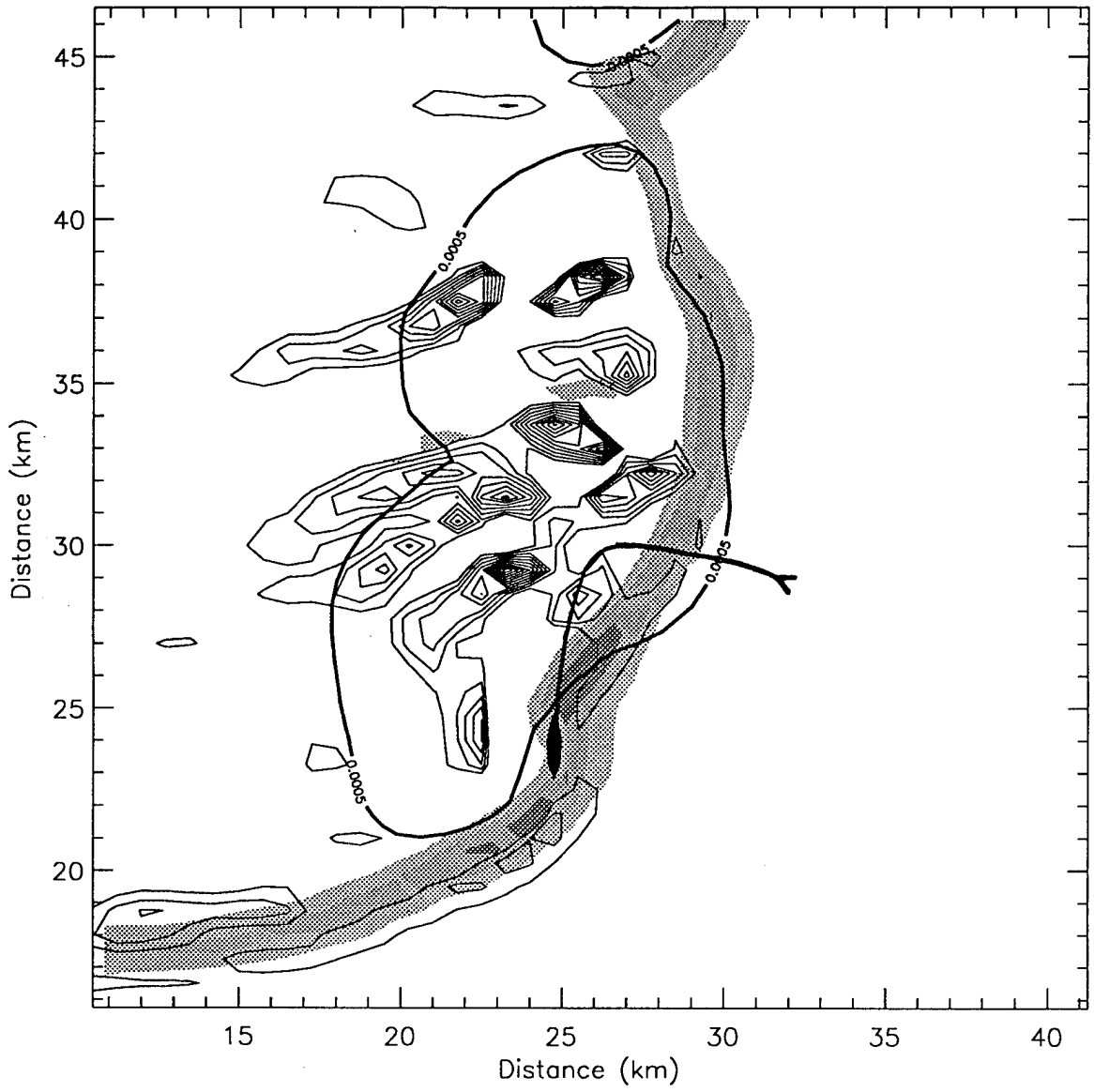

FIG. 24c. Same as FIG. 24a with tilting into the vertical (ranging from 0 to 0.0024 s^{-2} at contour interval of 0.0002 s^{-2}).

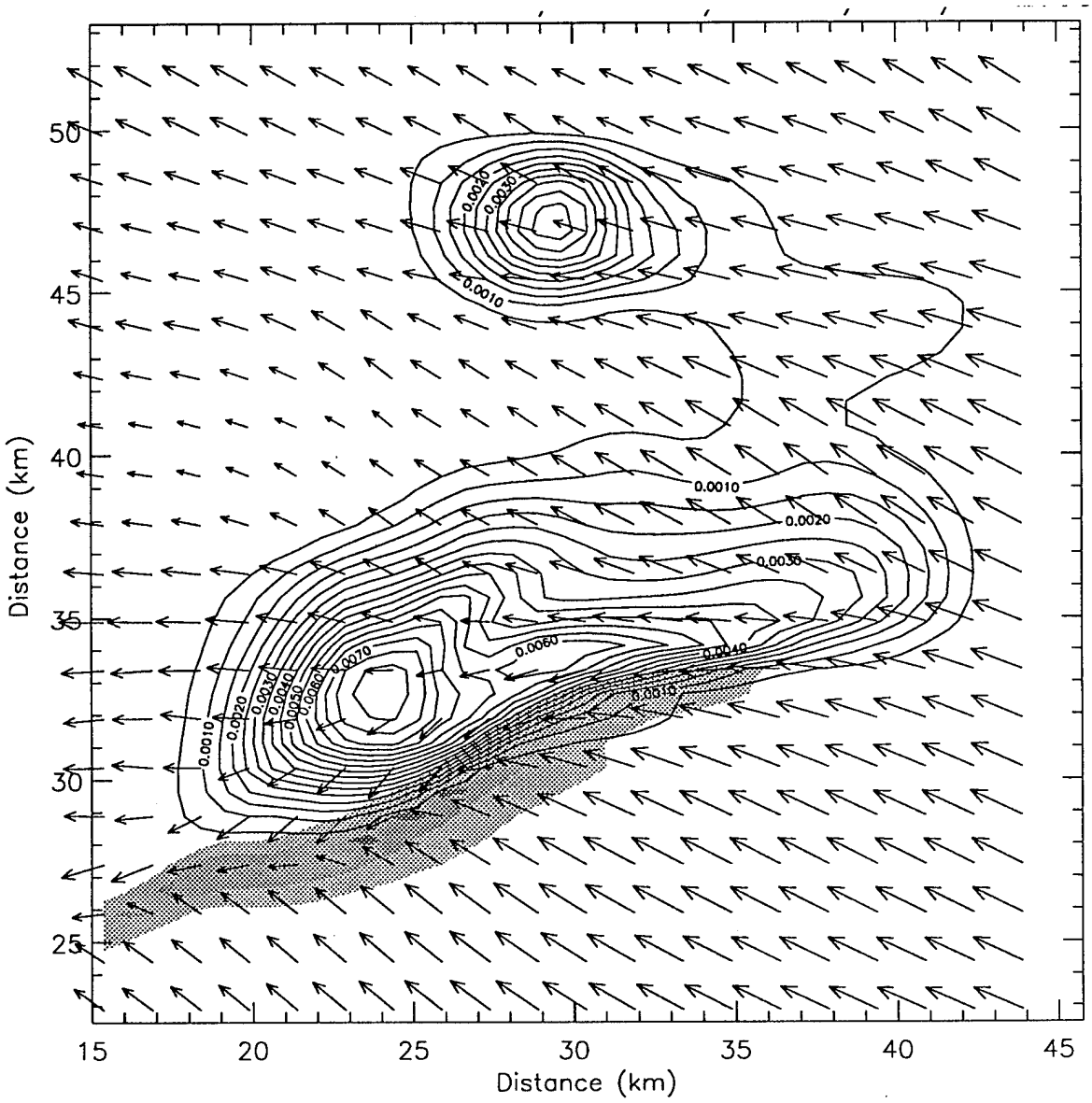

FIG. 25a. Rain region (contours of q_r at 0.5 g kg^{-1} interval), updraft (shaded at 1 m s^{-1} interval), and wind vectors (scale of vector is 1 km = 10 m s^{-1}) near the surface for the 07 km EL, 0.008 s^{-1} shear case at 130 minutes.

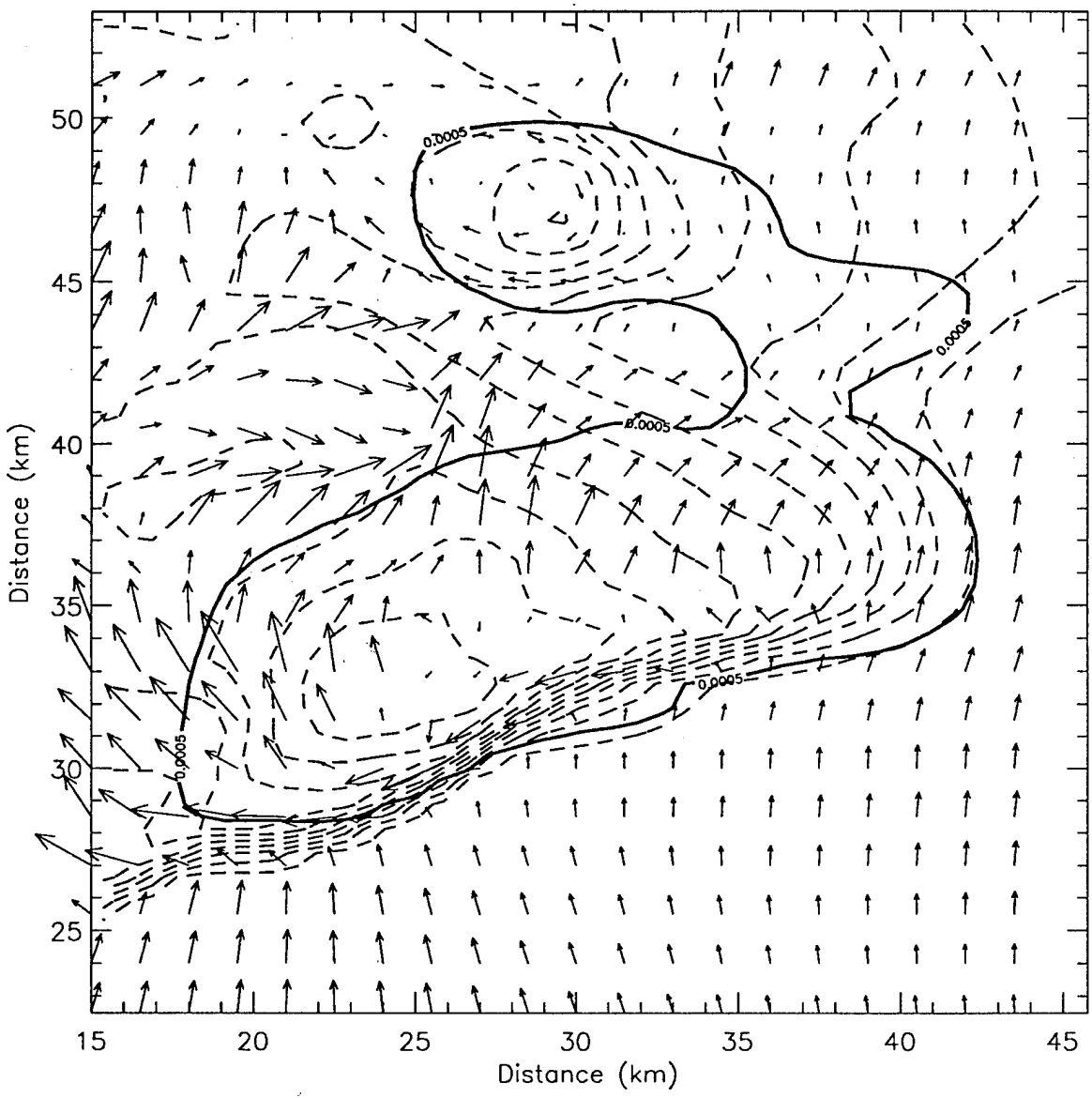

FIG. 25b. Surface rain region (thick contour of q_r = 0.5 g kg^{-1}), buoyancy (thin dashed contours from -0.26 m s^{-2} to 0.0 m s^{-2} at interval of 0.02 m s^{-2}), and horizontal vorticity vectors (vector scale is 1 km = 0.005 s^{-1}) for the 07 km EL, 0.008 s^{-1} shear case at 130 minutes.

s^{-1} shear case, and Figs. 25a-b depict the 0.008 s^{-1} shear case, both at 130 minutes. The 0.006 s^{-1} shear case shows an updraft oriented nearly north-south with a strong cold pool in the rear of the storm and large baroclinically generated horizontal vorticity vectors with a large streamwise orientation into the updraft from the north through northwest.

The gust front of the 0.008 s^{-1} shear case is oriented more east-west than that of the 0.006 s^{-1} shear case. In the 0.008 s^{-1} shear case, the strength of the cold pool is weaker due to the effects of stronger mixing in the updraft and downdraft. This has resulted in weaker horizontal vorticity vectors parallel to the buoyancy contours. The updraft is also weaker because it is weakened more by entrainment, and because the orientation of the gust front does not encourage strong surface convergence. There is a large streamwise component of the vorticity into the updraft but there are two problems here. First, the magnitude of the baroclinically generated horizontal vorticity vectors are small, so even if they are tilted by the updraft /downdraft gradient, they will contribute little to vertical vorticity production. Second, the updraft is elongated in the east-west direction, the same direction that the vorticity vectors are oriented. This means tilting will be very small. These two figures suggest that the 0.008 s^{-1} shear cases were not optimal for the production of strong low-level rotation. The time-averaged plots of vertical vorticity (Figs. 17a-c) bear this out as well.

c. Storm scale Richardson Number

The Richardson Number (*Ri*) is the characteristic ratio of work done against gravitational instability to energy transferred from mean to turbulent motion (Huschke 1959). This is represented in Eq. (11).

$$Ri = \frac{\frac{g}{\theta}\frac{\partial \theta}{\partial z}}{\left|\frac{\partial \vec{V}}{\partial z}\right|^2} \tag{11}$$

Moncrief and Green (1972) pointed out two important points about the Richardson Number. First, *Ri* is the ratio of available potential to available kinetic energy. Second, the value of *Ri* is dependent on the process that defines it. For example, the stability criterion for Kelvin-Helmholtz waves is different than for purely geostrophic flows. For storm processes, stability criterion cannot be obtained analytically. Instead, stability criterion must be developed with reference to observed storm behavior.

Moncrief and Green developed a function to represent the conservation of energy for a parcel moving along a streamline and entering a storm at height z_0 and speed u_0, then exiting at the top of the storm at height z_1 and speed u_1 (measured far away from the storm). From that function, they extracted a Richardson scale of:

$$Ri = \frac{-g\int_{z_0}^{z} \ln\left(\frac{\theta(z)}{\bar{\theta}(z)}\right) dz}{\frac{u^2{}_0}{2}} \tag{12}$$

where u_0 is the inflow wind. Weisman and Klemp (1982) used this function to define a Bulk Richardson Number (BRN).

$$BRN = \frac{CAPE}{\frac{u^2{}_0}{2}} \tag{13}$$

The numerator, which is vertically integrated buoyancy, is calculated up to the EL. The u_0 term in the denominator represents storm-relative inflow at the lowest level. To estimate

the strength of u_0, the storm's motion is computed using the 0-6 km density weighted mean wind. Drogemeier et al. (1993) and McCaul (1989) suggest that storm motion for supercells is best estimated by the density weighted mean wind computed over the depth of the shear layer however thick that may be. The storm's motion is then subtracted from the surface winds. Weisman and Klemp (1982) select the winds at 500 m to eliminate the effects of surface drag in the calculation. The numerator is a measure of the inflow kinetic energy. Moncrief and Green (1972) note that *Ri* is a function of height and they suggest computing an average *Ri* for the storm. This method was not persued further because, "... *in practice this would be inconvenient.*" That of course was 1972 when computers were not as readily available as they are today.

In this study and in others such as Rotunno and Klemp (1985), it is shown that storm motion is controlled primarily by the shear layer. The storm's motion ultimately determines the strength of the inflow kinetic energy. Additionally, it is unnecessary to measure outflow kinetic energy for the purpose of computing a Richardson Number using the original Moncrief and Green formulation. With this in mind, *Ri*(z) may be calculated at each level of the storm only through the shear layer and then averaged to obtain a storm representative *Ri* as Moncrief and Green suggested.

To calculate a mean storm Richardson Number, we initially compute *Ri*(z) by integrating the buoyancy from the LFC to z, then divide the integral by the estimated inflow kinetic energy of the storm. The inflow wind speed may be estimated by subtracting the 0-6 km density weighted mean wind from the environmental wind speed at 500 m AGL. After *Ri*(z) is calculated at each height, it is averaged over the depth from the LFC to the top of the shear layer at 6 km.

$$Ri(z) = \frac{g \int_{LFC}^{z} \frac{\theta'(z)}{\overline{\theta}(z)} dz}{\frac{u^2_0}{2}}, \overline{Ri} = \frac{\int_{LFC}^{6km} Ri(z^*) dz^*}{6km - LFC} \qquad (14)$$

Table 4 contains mean Richardson Numbers calculated for the shear layer of each of the nine storms in this study (compare with Table 1). The mean Richardson Numbers are scaled differently from the Bulk Richardson Numbers; however, they appear to distinguish from among the three types of storm behavior found in this study. All of the low shear cases produced multicell type storms, all of the moderate shear cases produced strong supercells with low-level mesocyclones, and all of the high shear cases produced supercells without low-level mesocyclones. While the sample of storms presented here is insufficient to prove the efficacy of using a mean *Ri* to evaluate an environment's potential to produce a particular storm type, future comparisons of observed storms and their mean *Ri* may be useful.

TABLE 4. Mean Richardson Numbers computed from the LFC to 6 km for each of the model simulations.

	0.004 s^{-1}	0.006 s^{-1}	0.008 s^{-1}
12 km EL	7.592	3.374	1.898
08 km EL	7.264	3.228	1.815
07 km EL	6.975	3.100	1.744

5. CONCLUSION

a. Summary

Severe low-topped supercells are difficult to forecast and detect. A greater understanding of severe supercellular and non-supercellular low-topped convection is important to increasing our ability to timely warn the public. Tornadic low-topped supercells appear to form in a variety of environments which are different than typical Great Plains severe storm environments.

The interaction of shear and buoyancy on supercell development is complex. To gain a better understanding of low-topped supercells, a 3-dimensional non-hydrostatic cloud model was used to simulate low-topped convection with many properties characteristics of supercells. This study modeled a range of environmental buoyancy and shear profiles with Bulk Richardson Numbers within the range predictive of supercells. Three idealized thermodynamic profiles were created by modifying the form of the analytic functions created by Weisman and Klemp (1982). The unique feature of the three temperature profiles was the variation in total CAPE. This was to see if environments with identical moderate low to mid-level buoyancy distributions, but differing total CAPE's, would produce supercell type convection. Three unidirectional wind profiles with constant shear magnitudes covering the range of shears predictive of supercells were also used. The cloud model was initialized with the nine combinations of these three thermodynamic profiles and three wind profiles.

The nine storms that developed in the cloud model behaved much like the unidirectional wind profile experiments of Weisman and Klemp (1982). Six of the storms satisfied the definition of low-topped convection as predicted by their EL heights. All three of the weakest shear cases (0.004 s^{-1}) did split to produce mirror image leftward and rightward propagating cells similar to supercells; however, after one hour of integration the ambient

shear was insufficient to slow the forward movement of the gust front and the storms evolved into multicells.

Quasi-steady updrafts formed in the remaining six storms. The most steady and persistent supercells were produced in the moderate shear environments. Maximum updrafts, maximum updraft heights, maximum mid-level mesocyclone strengths and maximum mid-level mesocyclone heights were stratified by the total CAPE of the environment. However, these storms had similar low-level distributions of updraft strength and vertical vorticity for a given shear profile independent of total CAPE. Additionally, only the moderate shear storms produced strong low-level mesocyclones of the same intensity and at the same time independent of the total CAPE, even though the lowest CAPE case had less than one third the CAPE of the highest CAPE case. In fact, the strength of the mid-level mesocyclone seemed uncorrellated with the strength of the low-level mesocyclone in all six of the supercell cases.

Because the moderate and high shear storms all produced supercells with persistent updrafts, the updraft forcing characteristics were examined for each of the moderate shear storms to examine why these storms behaved similarly. To do this, a trajectory analysis was performed within the core of the mature updraft for each of the three moderate shear storms. For each trajectory, the measured updraft was compared to the time-integrated dynamic and buoyancy forcing terms measured along the trajectory path. Results similar to Rotunno and Klemp (1985) were found, namely that dynamic forcing of the updraft dominates buoyancy forcing of the updraft from the surface to the mid-levels of these storms. This verified that the persistence and propagation of the updraft is primarily controlled by the shear induced non-hydrostatic vertical pressure gradient to the right of the ambient shear vector. Interestingly, the magnitude of the updraft forcing as well as the vertical distribution of the updraft forcing was similar among the moderate shear cases. The high CAPE storm had nearly the same updraft forcing characteristics below 5 km as the low CAPE storm.

All three of the moderate shear storms produced strong low-level mesocyclones of equal intensity at nearly the same time. A qualitative analysis of the production of vertical vorticity was done to examine the formation of the low-level mesocyclone. It was found that large horizontal vorticity is baroclinically generated by the cold pool density gradient similar to the findings of Rotunno and Klemp (1985), and that the reorientation and stretching of the baroclinically generated horizontal vorticity is responsible for producing the mesocyclone. The strength of the cold pool and the orientation of the low-level updraft was similar among the moderate shear cases. It is hypothesized that the low-level storm structure encouraged the production of vertical vorticity independent of the total CAPE, maximum updraft strength, or mid-level mesocyclone strength.

b. Implications

Observations of CAPE and shear magnitudes alone appear insufficient to characterize severe weather potential. In this study, Bulk Richardson numbers overlapped greatly between the low and moderate shear cases, however, storm behavior was most definitely distinguishable by shear magnitude. All three of the low shear cases produced multicell type convection, the moderate shear cases produced supercells with strong low-level mesocyclones and the high shear cases produced supercells with no strong low-level mesocyclone. It is suggested that a storm scale Richardson Number could be formulated with the vertical distribution of the buoyancy instead of the total CAPE. This method produced numbers that separated the storms into 3 regimes. The limited number of cases tested with this formulation is too small though to justify its application to all observed environments. Environments with large low-level distributions of buoyancy can produce supercells regardless of total CAPE or EL height. This is still implicit on the environmental shear being strong enough to maximize sources of horizontal vorticity, inflow wind strength, and the production of upward-directed vertical pressure gradients while being

weak enough so that entrainment is minimized. Low-level vertical buoyancy distributions may be more of a determining factor in supercell and low-level mesocyclone development than the total CAPE. Low-level mesocyclone development may be more sensitive to the strength of the low-level horizontal buoyancy gradients than to the magnitude of the mid-level mesocyclone.

c. Future work

This study generated more questions than it answered. In order to forecast and identify TLTS storms, additional work needs to be done. To help radar operators identify severe potential in low-topped convection, we need to evaluate storm top dynamics. Enhanced Doppler radar data displays for smaller signature patterns must be developed. We need more radar observations of severe and non-severe low-topped supercells, and to identify their frequency of occurrence. Construction of representative wind and buoyancy profiles from a large number of these events should be made for further numerical modeling. Attention must be focused on potential energy and kinematics for lower levels. Additional simulations that include ice microphysics need to be performed. We need to reevaluate bulk parameters and indices on observed prestorm environments that utilize only total CAPE. Some improvements in forecasting would likely result from considering low-level vertical buoyancy distributions in the sounding. Additionally, forecasters need to know more about the synoptic scale environments of the many systems that produce these tornadoes. Davies (1993a) stated: "*When the proper combination of wind and thermodynamic characteristics is present in a given environment, storms that develop in that environment can become supercells and produce tornadoes, regardless of vertical extent.*" The object of further research on this topic is to identify that "proper combination" so that severe weather from these storms can be timely and accurately forecast.

REFERENCES

Bluestein, H. P., 1985: The formation of a "landspout" in a "broken-line" squall line in Oklahoma. *14th Conf. Severe Local Storms*, Indianapolis, IN, Amer. Meteor. Soc., 267-270.

Brady, R. and E. Szoke, 1988: The landspout - a common type of northeast Colorado tornado. *15th Conf. Severe Local Storms*, Baltimore, MD, Amer. Meteor. Soc., 312-315.

Brandes, E. A., 1984: Relationships between radar derived thermodynamic variables and tornadogenesis. *Mon. Wea. Rev.*, **112**, 1033-1052.

Brooks, H. E., and R. B. Wilhelmson, 1990: The effect of low-level hodograph curvature on supercell structure. *16th Conf. Severe Local Storms*, Kananaskis Park, Alberta, Amer. Meteor. Soc., 34-39.

_____, C. A. Doswell, and R. B. Wilhelmson, 1994: The role of midtropospheric winds in the evolution and maintenance of low-level mesocyclones. *Mon. Wea. Rev.*, **122**, 126-136.

Browning, K. A., 1964: Airflow and precipitation trajectories within severe local storms which travel to the right of the winds. *J. Atmos. Sci.*, **21**, 634-639.

Burgess, D. W., 1976: Single Doppler radar vortex recognition. Part 1: Mesocyclone signatures. *17th Conf. Radar Meteorology*, Seattle, WA, Amer. Meteor. Soc., 97-103.

_____, and R. P. Davies-Jones, 1979: Unusual tornadic storms in eastern Oklahoma on 5 December 1975. *Mon. Wea. Rev.*, **107**, 451-457.

Cooley, J. R., 1978: Cold air funnel clouds. *Mon. Wea. Rev.*, **106**, 1368-1372.

Davies, J. M., 1993a: Small Tornadic Supercells in the Central Plains, *17th Conf. Severe Local Storms*, Vienna, VA, Amer. Meteor. Soc., 305-309.

_____, 1993b: Hourly helicity, instability, & EHI in forecasting supercell tornadoes. *17th Conf. Severe Local Storms*, Vienna, VA, Amer. Meteor. Soc., 107-111.

Davies-Jones, R. P., 1984: Streamwise vorticity: The origin of rotation in supercell storms. *J. Atmos. Sci.*, **41**, 2991-3006.

_____, D. W. Burgess, and M. P. Foster, 1990: Test of helicity as a tornado forecast parameter. *16th Conf. Severe Local Storms*, Kananaskis Park, Alberta, Amer. Meteor. Soc., 588-592.

Doswell, C. A., A. R. Moller, and R. Przybylinski, 1990: A unified set of conceptual models for variations on the supercell theme. *16th Conf. Severe Local Storms*, Kananaskis Park, Alberta, Amer. Meteor. Soc., 40-45.

Droegemeier, K. K., S. M. Lazarus, and R. P. Davies-Jones, 1993: The influence of helicity on numerically simulated convective storms. *Mon. Wea. Rev.*, **121**, 2005-2029.

Foster, M. P., A. R. Moller, L. J. Wicker, and L. E. Cantrell, 1995: The rapid evolution of a tornadic small supercell; observations and simulation. Preprints: *18th Conf. Severe Local Storms*, San Francisco, CA, Amer. Meteor. Soc.

Goetsch, E. H., 1988: Forecasting cold core severe weather outbreaks. *15th Conf. Severe Local Storms*, Baltimore, MD, Amer. Meteor. Soc., 468-471.

Golden, J., 1971: Waterspouts and tornadoes over south Florida. *Mon. Wea. Rev.*, **99**, 146-154.

_____, 1978: Scale-interaction implications for the waterspout life cycle. *J. Appl. Meteor.*, **13**, 693-709.

Guerrero, H., and W. Reed, 1993: Operational use of the WSR-88D during the November 21, 1992 Southeast Texas tornado outbreak. *17th Conf. Severe Local Storms*, St. Louis, MO, Amer. Meteor. Soc., 399-402.

Hales, J. E., Jr., 1993: Topographically induced helicity enhancement and its role in the Los Angeles Basin tornado maximum. *17th Conf. Severe Local Storms*, St. Louis, MO, Amer. Meteor. Soc., 98-101.

Hart, J. A., and W. D. Korotky, 1991: The SHARP workstation - v1.50. A skew-T / hodograph analysis and research program for the IBM and compatible PC. User's manual. NOAA/NWS Forecase Office, Charleston, WV, 62 pp.

Hess, S. L., 1979: *Introduction to Theoretical Meteorology*. Robert E. Krieger Publishing Co., 364 pp.

Holton, J. R., 1992: *An Introduction to Dynamic Meteorology*. Academic Press, 511 pp.

Huschke, R., 1959: *Glossary of Meteorology*. Amer. Meteor. Soc., 638 pp.

Johns, R. H., and C. A. Doswell III, 1992: Severe local storms forecasting. *Wea. Forecasting*, **7**, 588-612.

Kennedy, P. C., N. E. Westcott, and R. W. Scott, 1990: Single doppler radar observations of a mini-tornado. *16th Conf. Severe Local Storms*, Kananaskis Park, Alberta, Amer. Meteor. Soc., 209-212.

Klemp, J. B., and R. Wilhelmson, 1978: The simulation of three-dimensional convective storm dynamics. *J. Atmos. Sci.*, **35**, 1070-1096.

_____, and R. Rotunno, 1983: A study of the tornadic region within a supercell thunderstorm. *J. Atmos. Sci.*, **40**, 359-377.

_____, 1987: Dynamics of tornadic thunderstorms. *Ann. Rev. Fluid. Mech.*, **19**, 369-402.

Kessler, E., 1969: *On the Distribution and Continuity of Water Substance in Atmospheric Circulation.* Meteor. Monograph 32, Amer. Meteor. Soc., 84 pp.

Lazarus, S. M. and K. K. Droegemeier, 1990: The influence of helicity on the stability and morphology of numerically simulated storms. *16th Conf. Severe Local Storms*, Kananaskis Park, Alberta, Amer. Meteor. Soc., 269-274.

Lemon, L. R., and C. A. Doswell, 1979: Severe Thunderstorm Evolution and mesocyclone structure as related to tornadogenesis. *Mon. Wea. Rev.*, **107**, 1184-1197.

Lilly, D., 1986: The structure, energenetics and propagation of rotating convective storms. PartII: Helicity and storm stabilization. *J. Atmos. Sci.*, **43**, 126-140.

Maddox, R. A., L. R. Hoxit, and C. F. Chappel, 1980: A study of tornadic thunderstorm interactions with thermal boundaries. *Mon. Wea. Rev.*, **108**, 322-336.

Marwitz, J. D., 1972: The structure and motion of severe hail storms. Part I: Supercell storms. *J. Atmos. Sci.*, **11**, 166-179.

McCaul, E. W., 1989: *The dynamics of simulated convective storms in hurricane environments*. Report 88, Cooperative Institute for Mesoscale Studies, Norman, OK.

_____, and M. L. Weisman, 1995: Simulations of shallow supercell storms in landfalling hurricane environments. Submitted for publication to *Mon. Wea. Rev.* (Personal collection of Dr. Louis Wicker, Texas A&M University, College Station, TX.)

Moncrieff, M. and J. Green, 1972: The propagation and transfer properties of steady convective overturning in shear. *Quart. J. Royal Meteor. Soc.*, **98**, 336-352.

Murphy, T. W., and V. S. Woods, 1992: A damaging tornado from low topped convection. *Symposium on Weather Forecasting*, Atlanta, GA, Amer. Meteor. Soc., 195-201.

Moller, A. R., and G. Ely, 1985: On the operational problem of warning for the anomalous severe weather event: The Dallas county tornado of December 13, 1984. *14th Conf. Severe Local Storms*, Indianapolis, IN, Amer. Meteor. Soc., 346-349.

Ray, P. S., 1976: Vorticity and divergence within tornadic storms from duel Doppler radar. *J. Appl. Meteor.*, **15**, 879-890.

_____, 1986: *Mesoscale Meteorology and Forecasting*. Amer. Meteor. Soc., 793 pp.

Rotunno, R., 1981: On the evolution of thunderstorm rotation. *Mon. Wea. Rev.*, **109**, 171-180.

_____, and J. B. Klemp, 1982: The influence of shear indiced pressure gradient on thunderstorm motion. *Mon. Wea. Rev.*, **110**, 136-151.

_____, and J. B. Klemp, 1985: On the rotation and propagation of simulated supercell thunderstorms. *J. Atmos. Sci.*, **42**, 271-292.

_____, 1993: Supercell thunderstorm modeling and theory. *The Tornado: Its Structure, Dynamics, Prediction, and Hazards*. Geophysical Monograph 79, Amer. Geophys. U., 57-73.

Thompson, R. L., et al., 1994: Operational response of the WSO HOU to the 16 Nov 1993 Houston area tornadoes. NOAA/Houston Area National Weather Service Office, Dickinson, TX.

Vescio, M. D., et al., 1993: A low-top weak reflectivity severe weather episode along a thermal/moisture boundary in eastern North Carolina. *17th Conf. Severe Local Storms,* St. Louis, MO, Amer. Meteor. Soc., 628-632.

Vickers, G. C., 1990: Two small Alberta tornadoes. *16th Conf. Severe Local Storms*, Kananaskis Park, Alberta, Amer. Meteor. Soc., 522-525.

Wallace, J. M., and P. V. Hobbs, 1977: *Atmospheric Science: An Introductory Survey.* Academic Press, Inc., 467 pp.

Weisman, M. L., and J. B. Klemp, 1982: The dependence of numerically simulated convective storms on vertical wind shear and buoyancy. *Mon. Wea. Rev.*, **110**, 504-520.

_____, 1984: The structure and classification of numerically simulated convective storms in directionally varying wind shears. *Mon. Wea. Rev.*, **112**, 2479-2498.

Wicker, L. J., and R. B. Wilhelmson, 1993. Numerical simulation of tornadogenesis within a supercell thunderstorm. *The Tornado: Its Structure, Dynamics, Prediction, and Hazards*. Geophysical Monograph 79, Amer. Geophys. U., 75-88.

Wilhelmson, R. B., and J. B. Klemp, 1978: A numerical study of storm splitting that leads to long lived storms. *J. Atmos. Sci.*, **35**, 1974-1986.

APPENDICES

APPENDIX A

DEFINITIONS

Adiabatic Process: A reversible, thermodynamic change of state of an air parcel in which there is no transfer of heat or mass energy across the boundaries of the parcel. Compression of the parcel results in warming; expansion results in cooling. If the parcel is expanded or cooled beyond the point of saturation for the water vapor contained within the parcel, parcel theory allows the removal of the liquid water from the air parcel (i.e. allows it to fall out). This process is termed the "moist adiabatic process." (Huschke 1959)

Beltrami Flow: A fluid motion in which the vorticity vector is parallel to the velocity vector at every point in the fluid. (Huschke 1959)

Buoyancy: The ratio of the specific weight of an air parcel to the specific weight of the surrounding air. Buoyancy is defined by (McCaul 1989):

$$b = g\left\{\frac{\theta'}{\theta_0} + 0.61q_v' - q_c - q_r\right\} \text{ where}$$

g is gravitational acceleration

θ' is perturbation potential temperature

θ_0 is environmental potential temperature

q_v' is perturbation water vapor mixing ratio

q_c is cloud water mixing ratio

q_r is rain water mixing ratio

BRN: Bulk Richardson Number. $BRN = \frac{CAPE}{\frac{1}{2}\left|\vec{\bar{V}}\right|^2}$ where $\left|\vec{\bar{V}}\right|$ is the difference between environmental wind speeds at low levels and mid-levels. (Weisman and Klemp 1982)

CAPE: Convective Available Potential Energy per unit mass. The vertically integrated positive buoyancy of a parcel rising from the surface. (Moncrieff and Green 1972) The maximum vertical wind speed which may occur based solely on adiabatic ascent is related to CAPE by the expression: $w_{max} \approx \sqrt{2CAPE}$

Cold-Core Low: Any synoptic scale low that is generally characterized by cooler air near its center than around its periphery. (Huschke 1959)

Dust devil: A small but vigorous whirlwind, usually of short duration, rendered visible by dust. (Huschke 1959)

Dryline: A zone over the Great Plains area of the U.S. separating moist air flowing off the Gulf of Mexico and dry air flowing off the plateau regions of Mexico and the southwest. The sharpness of the moisture gradient along the dryline is affected by orographic elevation. (Ray 1986)

EL: Equilibrium Level. The maximum height positive, buoyant energy is available to a parcel rising from the surface.

Entrainment: The mixing of the environmental air into an organized updraft. It is proportional to the magnitude of the shear normal to the updraft, and the density gradient between the updraft and the environment. It is also inversely proportional to the strength of the updraft. (Huschke 1959)

Helicity: Helicity (H) is the correlation between the velocity vector and the vorticity vector. (Lilly 1986)

$$H = \vec{V}_{3d} \bullet \vec{\omega}$$

Hodograph: In meteorology, it is a plot of the vertical distribution of horizontal wind. The axes of the wind hodograph are u and v components of horizontal wind. A horizontal wind vector is plotted as a point. Continuously plotting horizontal wind vectors at increasing heights results in a trace-line. The length of the trace is proportional to the vertical shear between the end-point heights. (Huschke 1959)

Hydrostatic vertical pressure gradient: The vertical pressure gradient resulting from the pressure at each level being solely due to the weight of the fluid above. (Huschke 1959)

Landspout: Tornado type coined by Bluestein (1985). A landspout is a weak tornado which develops from the ground up to cloud base along colliding mesoscale boundaries which are present prior to the formation of the parent storm. These tornadoes usually come from rapidly developing multi-cellular cumulonimbi; and are small, weak, rope-like, and short-lived (5-10 minutes). They are common in northeast Colorado. (Brady and Szoke 1988)

LCL: Lifting Condensation Level. The level at which a parcel of moist air lifted adiabatically would become saturated. (Huschke 1959)

LFC: Level of Free Convection. The minimum height positive buoyant energy is available to a parcel rising from the surface. The level at which a parcel of air lifted adiabatically would first become warmer than its surroundings. (Huschke 1959)

Mesocyclone: A mesocyclone is a mesoscale region (5 - 10 km across) with locally high vertical vorticity. (Ray 1976)

Occluded Front: A composite of two fronts as a cold front overtakes a warm front or quasi-stationary front. (Huschke 1959)

S: A measure of storm strength. It is the maximum vertical velocity obtained in a particular storm normalized by the maximum which would have occurred based solely on adiabatic parcel ascent. (Weisman and Klemp 1982)

Supercell: A convective storm type characterized by a single, quasi-steady, rotating updraft, having a lifetime of several hours while propagating continuously to the right (normally) of the mean wind. It may produce high winds, large hail, and tornadoes. (Ray 1986)

SREH: Storm Relative Environmental Helicity. SREH = -2 times the signed area swept out by the storm-relative wind vector (on a hodograph) while ascending through a layer. (Davies-Jones *et al.* 1990) Has units $m^2\ s^{-2}$ or $J\ kg^{-1}$.

$$SREH = \int_{h}^{0} \hat{k} \bullet \left(\vec{V} - \vec{c}\right) \times \frac{\partial \vec{V}}{\partial z} dz \quad \text{where}$$

$\vec{V}(z)$ is the environmental wind profile

$\vec{c}$ is the storm motion vector

$\hat{k}$ is the unit vector in the vertical

TLTS: Tornadic low-topped supercell

Tropopause: The boundary between the troposphere and stratosphere, usually characterized by an abrupt change of temperature vertical lapse rate. Its height varies from 15 to 20 km in the tropics to about 10 km in the polar regions. Precipitation systems occur exclusively within the troposphere. (Huschke 1959)

Troposphere: The lowest 10-20 km of the atmosphere. It is characterized by decreasing temperature with height, appreciable vertical wind motions, appreciable water vapor content and weather. (Huschke 1959)

Vorticity: A point measure of rotation in a fluid. It is the curl of the velocity field. (Holton 1992) In Cartesian coordinates, vorticity ($\vec{\omega}$) is given by:

$$\vec{\omega} = \left(\frac{\partial w}{\partial y} - \frac{\partial v}{\partial z}, \frac{\partial u}{\partial z} - \frac{\partial w}{\partial x}, \zeta \right)$$

where $\zeta = \frac{\partial v}{\partial x} - \frac{\partial u}{\partial y}$ is the vertical component of vorticity.

The production of vorticity is described through the vertical and horizontal vorticity tendency equations (Klemp 1987):

$$\frac{d\zeta}{dt} = \vec{\omega}_h \bullet \vec{\nabla}_h w + \zeta \frac{\partial w}{\partial z} + F'_\zeta \qquad \text{(tilting + stretching + mixing)}$$

$$\frac{d\vec{\omega}_h}{dt} = \vec{\omega} \bullet \vec{\nabla} \vec{V}_h + \vec{\nabla} \times \left(b\hat{k} \right) + F'_h \quad \text{(tilting and stretching + baroclinic + mixing)}$$

where F' represents turbulent mixing. The subscript h represents the horizontal component of the Cartesian vector.

Waterspout: An intense columnar vortex of small horizontal extent that occurs over a body of water. Visible funnels generally do not extend from cloud base to surface as do most tornadoes. Generally, waterspouts have weaker intensity, shorter duration, and slower translation speeds than land tornadoes, and they may originate from shallow-topped cumuli. (Golden 1971)

π': Non-hydrostatic pressure perturbation where $\pi' = \left(\frac{p}{p_0}\right)^{R_d/c_p} - \overline{\pi}$

p is total pressure (initial + perturbation)

p_0 is reference pressure

R_d is specific heat of dry air

c_p is specific heat of air at constant pressure

$\overline{\pi}$ is hydrostatic pressure

APPENDIX B

OBSERVATIONS OF TORNADIC LOW-TOPPED CONVECTION

Several observations of tornadic low-topped convection have been published in recent *Radar* and *Severe Local Storms* conferences and the *Monthly Weather Review.* Only a few of them, however, described the convection as supercellular. To gain a better understanding of the tornadic potential from low-topped convection, a brief review of some tornadic low-topped events are presented here. Observations of low-topped supercells are presented first, followed by observations of tornadic non-supercellular low-topped convection.

1. Observations of Tornadic Low-Topped Supercell (TLTS) Storms

a. *Albany, Texas*

The primary motivation for this study stems from a low-topped tornadic supercell near Albany, Texas on 19 February, 1994 that was reported by Mike Foster and Alan Moller of the Fort Worth NWS Forecast Office. This storm was less than 9 km deep, less than 5 km wide and produced a tornado lasting about 10 minutes (Foster et al. 1995).

The parent synoptic scale system was a pacific cool front moving slowly east across Texas. The mesoscale system within which this particular storm cell was embedded was a squall line believed to have resulted from low pressure development beneath a well placed jet streak above the front. This cell, at the southern end of the squall line, caught the eye of radar observers because it periodically bowed out indicating a series of microbursts later confirmed in damage surveys. WSR88D algorithms were alerting forecasters to mesocyclones, but real time interpretation of the velocity fields and reflectivity fields

indicated only line type shear (such as along a gust front) instead of deep rotation. As the storm got closer, they reconfigured their radar to scan higher into the storm and identified a bounded weak echo region (BWER) at about 4 km AGL (6° elevation), a hook echo at 0.5° elevation shortly after, and then a tornado vortex signature (TVS) at 0.5° after that all in the span of 12 minutes. A pre-touchdown warning was successfully issued because the forecasters identified a BWER in the mid- to upper-levels of the storm and did not wait for the TVS.

This storm [as well as others reported by Davies 1993a, Thompson et al. 1994, Moller and Ely 1985, Guerrero and Read 1993, Murphy and Woods 1992, and Burgess and Davies-Jones 1979] has raised some important questions about a storm type that is becoming increasingly observed with the advent of the new Doppler radar network. How can low-topped convection become supercellular and possibly tornadic? Were the environmental temperature and wind profiles indicative of the potential for producing severe low-topped supercells? To search for answers to these questions, a 3-dimensional numerical cloud model was initialized with the nearby environmental temperature and wind profiles of the Albany, TX storm. That model did indeed produce a low-topped convection pattern with many characteristics similar to supercells (see Foster et al. 1995, Fig. 9) namely deep rotation, a BWER structure in the rainwater fields, and cell size relative to that which was observed in the Albany, TX storm.

b. Pratt, Kansas

Davies (1993a) observed two small supercells on March 11, 1990 and on April 28, 1991 both near Pratt, Kansas. These small supercell storms were associated with cold lows aloft, were low-topped, and had little or no lightning. The synoptic pattern was similar for both cases. A cold upper low was positioned above and slightly upwind of a surface low, and was associated with cold mid-level temperatures of around -20°C or less. A surface dryline

extended southeast of the surface low. Moderate to strong mid-level winds also extended to the south and east of the upper low. The environment ahead of the dry line was only weakly unstable. Beneath such a cold upper low, low-topped non-supercell storms can produce weak tornadoes or funnels (Johns and Doswell 1992, and Cooley 1978).

The March 11, 1990 case had many interesting features. It was a single long lived supercell with no wall cloud evident. A clear slot implying a rear flank down draft was visible and low level cloud movement suggested strong inflow. There was also a short flanking line of cumulus towers. Davies observed three tornadoes rated F1 and received reports of funnels aloft. Radar indicated tops between 25,000 and 28,000 ft (~9 km) with brief heavy rains and some hail falling north of the storm's updraft region.

In contrast, the April 28, 1991 case consisted of several tiny and short lived rotating cells which lasted on the order of tens of minutes. Cloud striations on the south and east flank suggested rotation, and a clear slot implying a rear flank down draft was visible. In this case there was no flanking line. He observed one tornado rated F1 and two "dust-whirl" tornadoes with no condensation funnels. The storm had characteristics of a low-precipitation supercell. Radar indicated only rain showers with tops at 21,000 ft (~7 km) and only one lightning flash was observed.

The thermodynamic and wind profiles (March 12, 1990 case) suggested tornadic potential. The environment was characterized by a low tropopause, a low EL at about 24,000 ft, and a low CAPE at about 915 J kg^{-1} (Fig. 1). A steep vertical lapse rate at about 8.2 °C km^{-1} occurred between 850 mb and 600 mb. This storm exhibited strong 0-3 km storm relative helicity (327 $m^2 s^2$), and strong 0-2 km storm relative inflow (21 knots). The Energy Helicity Index (EHI: Hart and Korotky 1991) was 3.7 which indicates tornadic supercells. Strong mid-level winds (48 knots) were also observed.

One possible explanation of tornadic potential derived from the lower values of CAPE is in its vertical distribution. Davies' analysis of the Kansas March 11, 1990 case revealed the CAPE is confined to roughly one half to two thirds the vertical distance associated with

typical severe storm environments. This implies moderate lapse rates that encourage rapid buoyant acceleration in updrafts. Other good indications of tornadic potential in low topped supercells are the 0-3 km AGL storm relative helicity (Davies-Jones et al. 1990) and the 0-2 km AGL storm relative inflow (Lazarus and Droegemeier 1990). Davies also found that numerical models can help. He showed that EHI and 0-2 km AGL inflow calculated from NGM based forecast winds and temperatures aloft isolated a narrow region of severe weather potential coordinate with the observed region of tornadic activity.

c. Bement, Illinois

Although the development of mid-level mesocyclones in large thunderstorms is becoming easier to detect with Doppler radar, algorithms have not been fully developed to detect other tornadogenesis patterns such as from low-topped supercell storms. Kennedy, Westcott, and Scott (1990) endeavored to expand the spectrum of Doppler radar observed tornadic storms by documenting a low-topped thunderstorm tornado.

In this case, a TLTS occurred on 19 May 1989 near Bement, Illinois. The tornado was rated F0-F1 and it lasted 25 minutes traveling 15 km. The synoptic pattern was not unusual. Surface winds were southerly ahead of an advancing moderate cold front. A line trough was identified on the surface, 850 mb and 500 mb charts in central IL. Satellite depicted a pronounced mesoscale comma pattern with deep convection in an arc from western IN to southern IL. The environment's thermodynamic and wind profiles were not strongly indicative of severe weather potential. Near the arc of deep convection at Paducha, KY, the lifted index was -3, and the K-index was 36. In the tornado environment behind the convective line at Peoria, IL (PIA), the lifted index was 0, and the K-index was 30. The wind at PIA veered 100° from surface to 500 mb with speeds less than 10 m s^{-1}. Radar indicated storm motion was 260° at 8.4 m s^{-1}. A small hook pattern was observed in the higher radar reflectivity contours. The maximum echo top height (15 dBZ) was 5-6 km

AGL. This height was roughly the height of a stable layer in the sounding (500 mb-600 mb). Radar observed wind velocities showed the tornado occurred when a strongly sheared layer ($40x10^{-5}$ s^{-1}) descended to near surface heights.

The synoptic setting was dissimilar to cold air funnel cases. Cooley (1978) reported these funnels generally occurred several hundred km to the rear of surface cold fronts, and beneath significantly cold air aloft. Neither of these characteristics applied to this case. hodograph curvature was modest and local soundings showed only weak instability. No tornado watch was in effect when the Bement, IL tornado occurred. The noteworthy radar characteristics were that the height of the maximum echo top was low (only 6 km) and the diameter of marginal echo intensity was small as well (6 km). Vertical circulation within a small region intensified near 3 km AGL instead of at 5-6 km AGL found in tornado producing Great Plains storms.

d. Houston, Texas

A recent example of a TLTS occurred on November 21, 1992 near Houston, Texas (Guerrero and Reed 1993). A shallow warm front about 100 nm south of the Texas coast was moved northward over Corpus Christi by a strong short wave. The shallow layer of moisture associated with the warm front was capped at about 850 mb by strong subsidence noted between 00z and 12z observation times. It appeared the short wave and the shallow warm front produced strong cyclonic shearing between the surface and 3 km at 12z which deepened to 6 km by 22z. At 22z, storm motion was indicated 203/26. The EL was near 31,000 ft. The helicity and CAPE had been increasing with time during the event. Estimations of Storm Relative Helicity (SRH) for the time frame of the tornado was strong at 437 m^2 s^2. There was also a huge increase in calculated SRH between 12z and 00z observations.

e. Atlanta, Georgia

Another TLTS event occurred on October 1, 1989 producing three tornadoes rated F2 just east of Atlanta, GA (Murphy and Woods 1992). The maximum top reported was 29,000 ft. The synoptic setting consisted of an upper level cold core low with a nearly closed circulation that was being propagated east-northeast by a deeper upstream trough. A cold front associated with a filling occlusion over Memphis, TN extended southward to the Gulf of Mexico. A slowly moving east-west oriented warm front over GA intersected the cold front. A surface low formed at the intersection just west of Atlanta. A north-south line of showers with isolated thunderstorms developed behind the cold front and beneath the cold pool aloft. Tops were reported between 27,000 and 29,000 ft.

A sounding taken 50 miles from Atlanta indicated a strong subsidence cap at about 770 mb. CAPE was calculated to be 196 $m^2 s^2$, with a Bulk Richardson Number of 1. The equilibrium level (EL) was 27,000 ft. Wind direction veered 180° from the surface to 6 km and speed varied from 5 m s^{-1} at the surface to 30 m s^{-1} at 6 km. Murphy and Woods hypothesize that an increase of buoyancy occurred only in the lower levels of the system since storm tops were at 27,000 ft. Murphy and Woods believe warm air advection played little role in tornadogenesis. They note, however, streamlines indicated an axis of convergence along the cold front. As the tornado parent cell crossed the front, it may have encountered a local maximum of convergence.

A cursory review of the nearby environments for some of these cases indicates these storms may share strongly sheared winds within the lower levels of the troposphere in addition to low equilibrium levels. Severe weather potential from low-topped convection may be due to steeper lapse rates over a shallower depth, thus CAPE for these cases should be considered with reference to its vertical distribution (Davies 1993a).

2. Observations of Tornadic Low-Topped Non-Supercellular Convection

Low-topped non-supercell storms under a variety of meteorological conditions can also produce tornadoes. These include frontal thunderstorms, cold core lows, cold air outbreaks, thermal/moisture boundaries, land-falling hurricanes, and topographically forced convection.

a. Storms similar to land spouts in Alberta, Canada

Vickers (1990) documented two non-supercell cases in Alberta Canada that were difficult to characterize but had many similarities to landspouts. They occurred on August 1, 1988 at Airdrie, Alberta, and on June 27, 1989 at Edmonton, Alberta.

The first case, at Airdrie, began as a stationary cold low over southern British Columbia with 100 kt jet and an associated cold trough extending into eastern Oregon with weak positive vorticity advection (PVA) across southern Alberta and southern B.C.. A thermal ridge extended over Edmonton. This systems high-level diffluent flow indicated divergence aloft over southern Alberta. The airmass had low-level moisture and was dry above 700 mb at the time of the tornado. It rained all morning over southern Alberta in the vicinity of the trowal. The cold trough in the system rotated NE and cooled the mid-levels thus increasing potential instability. The small tornado formed during a break in the rain near Airdrie.

The second case, at Edmonton, was characterized by a cold low over southwestern B.C. with an 80 kt jet and an associated cold trough extending to eastern Oregon with weak PVA over southern Alberta. An 850 mb thermal ridge extended over Calgary, and a 500 mb thermal ridge extended over Lloydminster. This produced diffluent flow between trough and ridge with a trowal and a low-level moisture axis over Edmonton. Moderate to strong winds in the vicinity of the trowal caused convergence along the moisture axis. A sounding

at Stoney Plain for 12z indicated a conditionally unstable airmass to 14,000 ft with dryer and more stable air above. The low-level wind shear was $9.9x10^{-5}$ s^{-1}. It rained during the morning. After the rain ended, surface heating and surface dew points (10 °C) contributed to the low-level instability. By this time, CAPE was 400 J kg^{-1} near Jasper. The tornado occurred at Edmonton under a rapidly developing TCu which was part of a feeder line to a well developed afternoon CB to its east.

These cases were similar to each other in many respects. Both were associated with a cold low with significant jet winds circulating around it. Tornadoes occurred in the left exit regions of the jet. Both had a 500 mb cold trough extending into Oregon and a thermal ridge extending eastward which provided some upper level cooling. Both had polar waves with a trowal hanging back. The low-level moisture axis and convergence zones were collocated with the trowels and both had conditionally unstable air masses. Both had significant low-level wind shear. Additionally, both occurred after rain events in high low-level moisture and rapidly developing convection.

These cases had characteristics that were similar and dissimilar to landspout characteristics described by Brady and Szoke (1988). The similar characteristics include: weak short lived tornadogenesis, development under rapid convective growth, rapid dissipation, and they had a weak short wave trough present. However, these cases were dissimilar to landspouts in that the synoptic scale situation was not in line with a severe thunderstorm environment, and the airmass was not very unstable.

b. Storms from cold core outbreaks throughout the U. S.

Another common mechanism for low-topped tornadogenesis is from cold core outbreaks. Goetsch (1988) alerts forecasters to the significance of cold core outbreaks in his study of 25 cases. Goetsch defined a cold core severe weather outbreak by the following criteria:

a. The presence of a closed low pressure center at 500 mb with an associated core of cold air in the area.
b. The 500 mb low center stacked nearly vertical over the 850 mb and surface low centers.
c. The occurrence of reports defining the case as an "outbreak".
d. A low level moisture axis is usually found protruding toward the surface low through the threat area.

In 70% of the cases studied by Goetsch (his study included 25 cases during March through May between 1981 and 1987), satellite imagery indicated warm cloud tops never reaching the dark gray shade (tops were warmer than -52 °C: that translates to less than 33,000 ft on the standard atmospheric trace). Goetsch reported that 60 reports of funnel clouds and tornadoes occurred during the cases he studied. Goetsch calls for an extensive study of stability indices, temperature and moisture fields, and wind flow patterns. Thus further analysis of cold core outbreaks may shed light on the mechanisms of low-topped convection tornadogenesis. In the case of cold core outbreaks, operational forecasters may focus on severe weather potential in the area of the original cold front and either miss or underestimate convection near the upper low region that may develop potential for tornadogenesis.

c. Cold air funnel clouds in Michigan

In 1978, Cooley presented a study of 7 cases of cold air funnel clouds in Michigan between 1963 and 1972. The synoptic, radar, thermodynamic, and wind characteristics are summarized here from Cooley's study.

The synoptic situations were characterized with the main surface low always well to the east of any reported funnel clouds. In most cases, there was a secondary low in the vicinity of the cold funnel cloud activity. No fronts were associated with the secondary low and the

cold front associated with the main low had passed through 18-42 hours earlier. On the 500 mb chart, there was a major trough over MI in all cases. The funnels occurred when the 500 mb temperature was at or near minimum. The funnels usually accompanied light showers and virga in the vicinity.

Radar indicated most days had thunderstorms. Line activity occurred for less than half of the cases. Cell movement was 230°-280° at 10-25 knots. There were NO indications of the following: rapid cell movement or abrupt changes in cell movement; hooks, v-notches, fingers, or scalloped edges; vertical protrusions; echo-free vaults; rotating cells or clusters; merging or splitting cells; rapidly developing cells, fine lines, or line echo wave patterns (LEWP). Funnels were always reported in the vicinity of the maximum top. The height of the convective cloud tops ranged from 4500 m to 12,000 m and averaged 7300 m. In almost all cases, tops were more than 2500 m below tropopause.

Severe weather potential may have been thermodynamically driven. Dew points in the vicinity of the funnel cloud averaged 9.4 °F lower than Lake Michigan temperatures. Warm moist advection from the lake is assumed to be a source of low-level moisture and latent instability. All cold air funnels occurred when the lake temperature was warmer than the air temperature. SI varied +1 to +11. K-index varied 2 to 25. From sounding data, wind speeds in fall cases were less than 20 knots at all levels. In summer cases, there was a weak low-level jet (5-15 kt at surface, 25-30 kt at 900 mb, and 10-20 kt above 1500 m).

While all of the cases he studied produced no tornado, it is interesting to note the funnel clouds are associated with low-topped convection. The characteristics of these systems are included here because they may be a basis for tornadic low-topped convection less an additional forcing mechanism necessary for touchdown.

d. Storms along a thermal moisture boundary (TMB) in North Carolina

Maddox et al. (1980) hypothesized moisture convergence and enhanced cyclonic vorticity near TMB's can contribute to storm intensification and lead to tornadogenesis. The thermal gradient noted by Cooley (1978) in his study of Michigan cold air funnel clouds may be similar to the forcing mechanism of the TMB discussed by Vescio et al. (1993) that produced an outbreak of eleven (F0-F1) tornadoes in eastern North Carolina on November 4, 1992.

On that date, an outbreak of eleven weak (F0-F1) tornadoes and one damaging microburst occurred along a TMB in eastern North Carolina. Storm tops were generally less than 30,000 ft. Maximum reflectivities were DVIP (Digital Video Integrator and Processor) level 3. Radar echo patterns were similar to HP (Heavy Precipitation) supercells. The synoptic pattern included a quasi-stationary TMB established in eastern North Carolina. Three boundaries were depicted on the 20z surface analysis. The first was a cold front over the western slopes of the Appalachians well west of developing severe weather. The second was a TMB defined in the temperature and dew point data over eastern North Carolina. The third was an outflow boundary that extended through western South Carolina into central Georgia.

The thermodynamic and wind situation showed evidence of dry air intrusion and a low-level wind maximum contributing to severe storm development. The 00z sounding at CHS indicated relatively dry air from 850-500 mb. A 20 m s^{-1} wind maximum near 850 mb was upstream of the severe weather area with moderate vertical wind shear. At Cape Hatteras (HAT) the 0-3 km SRH was 198 $m^2 s^2$. The surface wind was 5 m s^{-1}, but increased to 20 m s^{-1} from just above the surface to 850 mb. Convection was limited to the TMB suggesting that it provided the forcing for convective initiation. The increased shear near the TMB may have also locally raised the SRH. Even if the large scale environmental

helicity is not favorable for tornadoes, these mesoscale boundaries may locally increase the helicity to a level where tornadogenesis can occur.

Vescio et al. (1993) noted subtle severe weather signatures on radar may help identify tornadic potential such as weak inflow notches, kidney bean shapes, and broad hook similar to high precipitation supercells. They stated further that regionalized composite reflectivity has captured these subtle severe weather signatures and that systems such as WSR-88D will prove useful in detecting them in low topped reflectivity events.

f. Storms forced by topography in the Los Angeles Basin

Another factor that may contribute to local maximums of convergence that can encourage tornadogenesis in low topped convection is topography. Hales (1993) presented a study of such a mechanism to explain the locally high number of tornadoes that occur in the Los Angeles Basin. The L.A. basin has an atypically high incidence of tornado occurrence that is comparable to that of the Great Plains. Enhanced veering in the boundary layer is due to the blocking influence of the east-west San Gabriel mountains. Helicity is markedly increased and becomes available to enhance storm rotation. Storms are typically low topped with a lack of strong reflectivity. Hook echoes and bounded weak echo regions (BWER) are difficult to observe.

The shear characteristics within the inflow region of the updraft are important in determining potential for storms to develop supercell characteristics and tornadic low-level circulation. Lazarus and Droegemeier (1990) suggest that intense rotating updrafts can form with relatively weak instability if high values of helicity are supported by strong inflow. The tornado cases in the L. A. basin have two interesting characteristics. First, low-level helicity is enhanced by the forced backing of boundary layer winds. Second, there is strong storm relative inflow in the sub-cloud layer.

As an example, Hales noted a case on November 9, 1982 which produced 7 tornadoes (2 rated F2) over a 6-hr period. The synoptic situation included low pressure centers located off the central California coast from the surface to 500 mb, with a strong polar jet across San Diego. The cold front associated with the system was already in Arizona with a well defined surface trough approaching the coast. The 13z sounding at NTD indicated a lifted index (LI) of -2, and the CAPE was a marginal 450 J kg^{-1}. A Subsidence cap at about 800 mb provided dry air at mid-levels favorable for down draft enhancement. Modified hodograph data for 18z at L.A. revealed storm relative helicity (SRH) for 0-3 km was 327 $m^2 s^2$. The mean wind for 0-3 km was 102/25, the mean inflow for 0-3 km was 107/23, and the surface inflow was 060/04. Storm motion was 060/40.

f. Summary

High helicity may be confined to the 0-3 km layer instead of the 0-6 km layer, thus moderate to strong low level winds in the storm relative inflow should be carefully observed. The Alberta Canada tornadoes described by Vickers (1990) point out the synoptic scale situation need not always be typical for a severe weather environment to produce tornadoes, and that precipitation may be the only mechanism hindering tornadogenesis in some cases of rapidly developing convection. The speed of convective development may have been the key player in those cases. The radar analysis by Kennedy, Wescott, and Scott (1990) point out the need to focus on smaller radar signatures over a shallower depth. A possible solution is relying heavily on spotter reports and magnifying radar display capabilities to detect smaller tornado potential signatures. For the case of cold core outbreaks, Goetsch (1988) feels that forecasters can miss or underestimate severe weather potential in the vicinity of the upper low. Thus further training and research is necessary on cold core outbreaks to help forecasters identify the likelihood of tornadoes from these low-topped convective events. Steep thermal/moisture gradients such as in the

cases of Michigan cold air funnel clouds (Cooley 1978), and North Carolina TMBs (Vescio et al. 1993) may provide a local convergence mechanism necessary to produce tornadoes even though convective heights remain low. Hales (1993) noted the influence of topography can act to enhance low level helicity and storm relative inflow. Given a synoptic environment encouraged by orography and sufficient airmass instability, tornadoes do occur.

APPENDIX C

FORMULATION OF IDEALIZED THERMODYNAMIC PROFILES

1. The Original Function

The functions defining the potential temperature and moisture profiles were designed to produce smooth vertical distributions of these parameters. The surface temperature, relative humidity profile, and tropopause values of height, temperature and potential temperature are kept constant. The relative humidity profile is moist and varies almost linearly from the maximum at the lifted condensation level (LCL) to 25% at the tropopause. It is constant at 25% above the tropopause. The functions produce a temperature profile that is nearly dry adiabatic near the surface which becomes increasingly sub-dry adiabatic with height. The following are the original Weisman and Klemp (1982) functions for potential temperature and relative humidity.

$$\overline{\theta}(z) = \begin{cases} \theta_0 + (\theta_{tr} - \theta_0)\left(\dfrac{z}{Z_{tr}}\right)^a, & z \le Z_{tr} \\ \theta_{tr} \exp\left[\dfrac{g}{c_p T_{tr}}(z - Z_{tr})\right], & z > Z_{tr} \end{cases} \qquad \text{(C-1)}$$

$$H(z) = \begin{cases} 1 - \dfrac{3}{4}\left(\dfrac{z}{Z_{tr}}\right)^{5/4}, & z \le Z_{tr} \\ 0.25, & z > Z_{tr} \end{cases} \qquad \text{(C-2)}$$

$\overline{\theta}(z)$ is the environmental potential temperature
$H(z)$ is the environmental relative humidity
θ_0 is the surface temperature set to 300° K
θ_{tr} is the tropopause potential temperature set to 343° K
Z_{tr} is the tropopause height set to 12 km
T_{tr} is the tropopause temperature set to 213° K
a is the lapse rate exponent coefficient set to 1.25
g is the gravitational constant 9.81 ms^{-2}
c_p is the specific heat of dry air at constant pressure 1004 J $(kg\ K)^{-1}$

To approximate a well mixed boundary layer, q_{v0}, the surface mixing ratio is kept constant at a maximum value. Weisman and Klemp (1982) varied the surface parcel's buoyancy by adjusting the value of q_{v0}. Specifically, they selected values of 11 g kg^{-1}, 14 g kg^{-1} and 16 g kg^{-1} to produce CAPE's ranging from about 1000 m^{2}s^{-2} to about 3500 m^2 s^{-2}. Fig. C-1. is a skew-T log-p diagram of the original functions. To obtain input sounding files for the 3-dimensional numerical cloud model, potential temperature and relative humidity are calculated first using these functions. Iterative methods are then used to compute pressure using the hydrostatic equation, and to compute temperature using the Poisson equation. Other equations are also used to relate relative humidity to $q_v(z)$.

2. Control of EL

The functions in Weisman and Klemp (1982) for the thermodynamic profile primarily control the total CAPE of a lifted parcel by adjusting q_{v0} (i.e., the relative humidity profile below the LCL). There is no control over the heights of the LCL, LFC, or EL. There is also no control over the convective inhibition (CIN) or the surface parcel's wet potential temperature θ_w. By adjusting the coefficients a, and θ_{tr}, the height of the EL can be controlled while keeping the CAPE constant. Increasing θ_{tr} results in decreasing the EL. However to keep the CAPE from decreasing by this change in tropopause potential temperature, the coefficient a must be increased. The coefficient a affects the "bowness" of the temperature profile. Increasing a results in an increased lapse rate in the lower levels of the sounding resulting in higher CAPE. In actuality, we are solving the non-linear relationship $CAPE_1 = CAPE_2$, or:

$$g \int_{LFC_1}^{EL_1} \frac{\overline{\theta}_1(z) - \theta_{p1}(z)}{\overline{\theta}_1(z)} dz = g \int_{LFC_2}^{EL_2} \frac{\overline{\theta}_2(z) - \theta_{p2}(z)}{\overline{\theta}_2(z)} dz \qquad \text{(C-3)}$$

where $EL, LFC, \overline{\theta}(z), \theta_p(z)$ are all functions of the coefficients a, and θ_{tr}. Time consuming iterative methods may be used to find exact values of the coefficients required for particular CAPE and EL settings; however, it is sufficient to obtain these coefficients through trial and error.

3. Control of LCL and LFC

The CAPE and EL controlling coefficients a and θ_{tr} are insufficient to control other aspects of the thermodynamic profile such as the lifted parcel temperature profile, CIN,

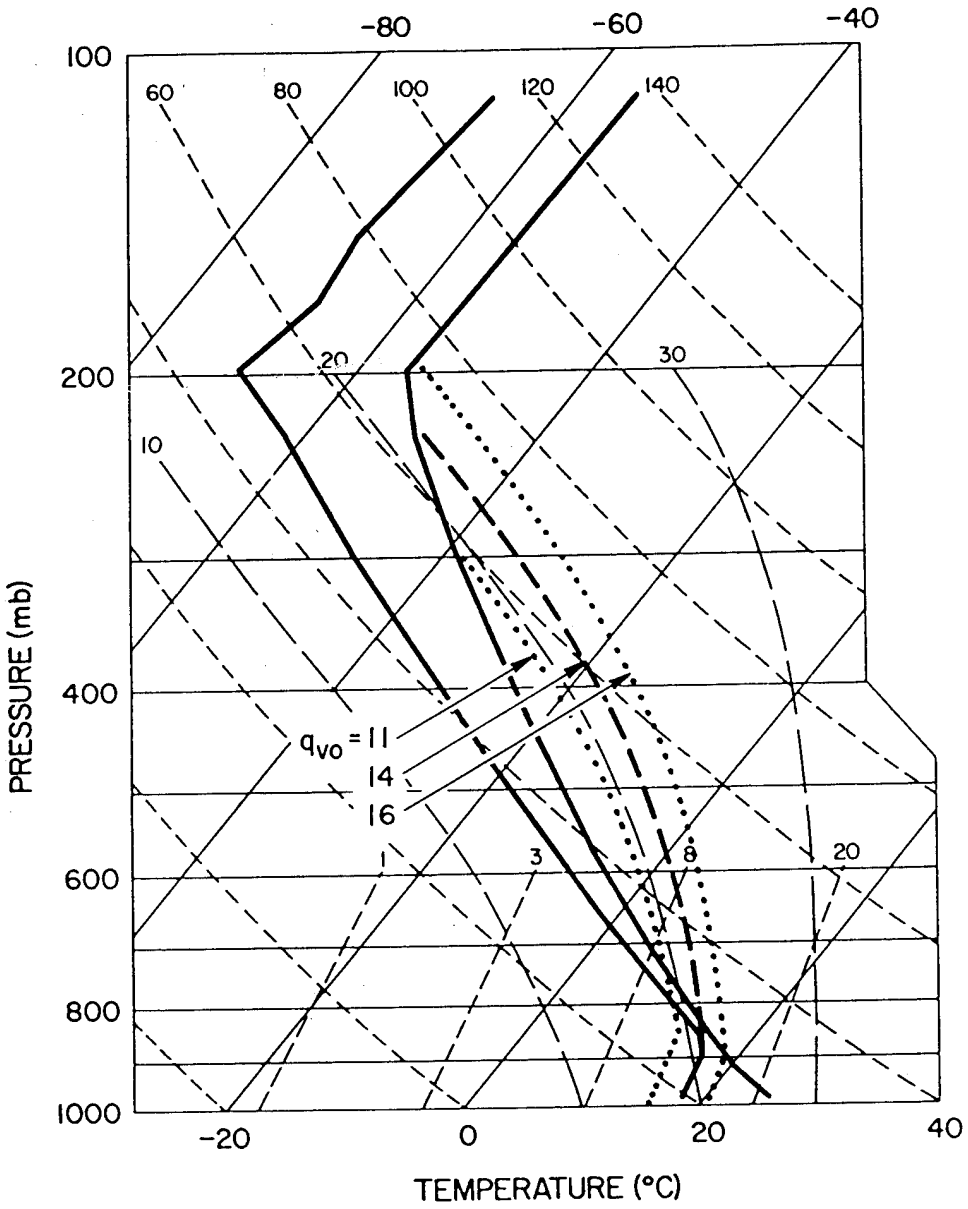

FIG. C-1. Skew T diagram depicting temperature and moisture profiles used in modeling experiments performed by Weisman and Klemp (1982) (heavy solid lines). Heavy dashed line represents a parcel ascent from the surface based on a surface mixing ratio of q_{vo} = 14 g kg^{-1}. Heavy dotted lines represent similar parcel ascents for q_{vo} = 11 g kg^{-1} and 16 g kg^{-1}. Tilted solid lines are isotherms, short dashed lines are dry adiabats, and long dashed lines are moist adiabats. (Reprinted from Weisman and Klemp 1982)

and the heights of the LCL and the LFC. To control these values as well, the temperature and relative humidity of each sounding must have equal profiles below the LFC. All that is required is that we select values of a and θ_{tr} to achieve the desired profiles below the level of the LFC. Once the required values of CIN, LCL, and LFC have been obtained, the remainder of the profile may be generated with other settings of a and θ_{tr} to obtain required values of CAPE and EL. Modifications to the functions for potential temperature below and above the LFC appear as follows.

$$\overline{\theta}(z) = \theta_0 + (\theta_{tr1} - \theta_0)\left(\frac{z}{Z_{tr}}\right)^{a1}, \quad z \le LFC \tag{C-4}$$

$$\overline{\theta}(z) = \begin{cases} \theta_{LFC} + (\theta_{tr2} - \theta_{LFC})\left(\dfrac{z - LFC}{Z_{tr} - LFC}\right)^{a2}, & LFC < z \le Z_{tr} \\ \theta_{tr2} \exp\left[\dfrac{g}{c_p T_{tr}}(z - Z_{tr})\right], & z > Z_{tr} \end{cases} \tag{C-5}$$

$$T_{tr} = \frac{\theta_{tr2}}{\left(\dfrac{p_0}{p_{tr}}\right)^{R_d/c_p}} \quad \text{The Poisson equation} \tag{C-6}$$

θ_{tr1} is the tropopause potential temperature for the function below the LFC
$a1$ is the lapse rate exponent coefficient for the function below the LFC
θ_{tr2} is the tropopause potential temperature for the function above the LFC
$a2$ is the lapse rate exponent coefficient for the function above the LFC
p_0 is the reference pressure (1000 mb)
p_{tr} is the tropopause pressure set to 188.869 mb

APPENDIX D

A DISCUSSION OF UPDRAFT FORCING

The dynamics of the updraft in a convective storm can be qualitatively represented with simplifications to the momentum equations. Following Klemp and Wilhelmson (1978), we begin with the equation of state for a moist parcel of air.

$$p = \rho R_d T_v \tag{D-1}$$

where p is the pressure

ρ is the density per unit mass

R_d is the gas constant for dry air

T_v is the virtual temperature defined by the function $T_v = T(1+0.61q_v)$

q_v is the mixing ratio of water vapor in the parcel.

For the purpose of simplification, we may define a non-dimensional pressure with respect to a reference pressure.

$$\Pi = \left(\frac{p}{p_0}\right)^{\frac{R_d}{c_p}} \tag{D-2}$$

where p_0 is the reference pressure. The function for the non-dimensional pressure has the property

$$\Pi = \frac{T}{\theta} = \frac{T_v}{\theta_v} \text{ where}$$

$$\theta = T\left(\frac{p_0}{p}\right)^{\frac{R_d}{c_p}} \tag{D-3}$$

$$\theta_v = T_v\left(\frac{p_0}{p}\right)^{\frac{R_d}{c_p}}$$

are the equations for the potential temperature and virtual potential temperature respectively, which is the adiabatic transformation of a dry or moist unsaturated air parcel to the reference pressure.

Using equations (D-1) through (D-3), a more useful expression for the non-dimensional pressure may be derived as follows:

$$\Pi = \left(\frac{p}{p_0}\right)^{\frac{R_d}{c_p}}$$

$$\Pi^{\frac{c_p}{R_d}} p_0 = p$$

$$\Pi^{\frac{c_p}{R_d}} p_0 = \rho R_d T_v$$

$$\theta_v = T_v \left(\frac{p_0}{p}\right)^{\frac{R_d}{c_p}}$$

$$\theta_v \left(\frac{p}{p_0}\right)^{\frac{R_d}{c_p}} = T_v$$

$$\Pi^{\frac{c_p}{R_d}} p_0 = \rho R_d \theta_v \left(\frac{p}{p_0}\right)^{\frac{R_d}{c_p}} = \rho R_d \Pi$$

$$\frac{\Pi^{\frac{c_p}{R_d}}}{\Pi} = \Pi^{\left(\frac{c_p}{R_d} - 1\right)} = \frac{\rho R_d \theta_v}{p_0}$$

$$c_p - R_d = c_v$$

$$\Pi^{\left(\frac{c_v}{R_d}\right)} = \frac{\rho R_d \theta_v}{p_0}$$

$$\therefore \Pi = \left(\frac{\rho R_d \theta_v}{p_0}\right)^{\frac{R_d}{c_v}} \qquad \text{(D-4)}$$

To obtain the momentum equations relevant to convection, we first use the Boussinesq approximation of the Navier-Stokes equations in the form:

$$\frac{D\vec{V}}{Dt} = -\frac{1}{\rho}\vec{\nabla}p - 2\vec{\Omega} \times \vec{V} + \vec{F} \qquad \text{(D-5)}$$

The terms on the right hand side represent pressure gradient forcing, including the effects of buoyancy and gravity forcing, Coriolis force, and turbulence. For the purpose of analyzing the gross scales of motion within storm type convection, turbulence is ignored. Additionally, since storm motions to be studied are small compared to planetary time scales, the Coriolis force is omitted as well. The result is the simplified equation:

$$\frac{D\vec{V}}{Dt} = -\frac{1}{\rho}\vec{\nabla}p \tag{D-6}$$

In order to represent the pressure in non-dimensional terms, we substitute pressure p on the right hand side of (D-6) using equations (D-2) and (D-4) as follows.

$$-\frac{1}{\rho}\vec{\nabla}p = -\frac{1}{\rho}\vec{\nabla}\left(\Pi^{\frac{c_p}{R_d}}p_0\right) = -\frac{p_0}{\rho}\frac{c_p}{R_d}\Pi^{\frac{c_v}{R_d}}\vec{\nabla}\Pi$$

$$\Pi^{\left(\frac{c_v}{R_d}\right)} = \frac{\rho R_d \theta_v}{p_0}$$

$$\therefore -\frac{1}{\rho}\vec{\nabla}p = -c_p\theta_v\vec{\nabla}\Pi \tag{D-7}$$

This pressure term may be expressed as the sum of the base state in hydrostatic equilibrium and a perturbation.

$\Pi = \overline{\pi} + \pi', \theta_v = \overline{\theta}_v + \theta_v'$: thus equation (D-7) becomes

$$-\frac{1}{\rho}\vec{\nabla}p = -c_p\left(\overline{\theta}_v + \theta_v'\right)\vec{\nabla}\left(\overline{\pi} + \pi'\right) \tag{D-8}$$

The right hand side of (D-8) may be expressed as four terms:

$$-c_p\left[\overline{\theta}_v\vec{\nabla}\overline{\pi} + \theta_v'\vec{\nabla}\overline{\pi} + \overline{\theta}_v\vec{\nabla}\pi' + \theta_v'\vec{\nabla}\pi'\right]$$

The first and second terms are assumed to have pressure in hydrostatic balance with no variation of pressure in the horizontal. The last term is simply discarded because it is small in comparison to the other terms. These terms then become

$$-c_p\left[\overline{\theta}_v\frac{\partial\overline{\pi}}{\partial z} + \theta_v'\frac{\partial\overline{\pi}}{\partial z} + \overline{\theta}_v\vec{\nabla}\pi'\right]$$

From the hydrostatic assumption of the base state pressure, equation (D-8) can be rewritten as:

$$-\frac{1}{\rho}\vec{\nabla}p = \vec{g} - c_p\overline{\theta}_v\vec{\nabla}\pi' \qquad \text{(D-9)}$$

The gravitational forcing term on the right hand side of (D-9) includes the effects of planetary gravity, centrifugal force due to the rotation of the earth, and the specific weights of the moist parcel, cloud water and rain water. As a simplifying assumption it is further given that the total gravitational force or buoyancy force has negligible components in the horizontal directions. To represent fully the influence of the parcel buoyancy, $\vec{g}$ is identified as $B\hat{k}$ where the total buoyancy B is defined as

$$B = g\left[\frac{\theta'}{\overline{\theta}} + 0.61q_v' - q_c - q_r\right] \qquad \text{(D-10)}$$

where g is the gravitational constant

θ' is the difference between the parcel and environmental potential temperatures

$\overline{\theta}$ is the base state profile of potential temperature as a function of height only

q_v' is the difference between the parcel and environmental water vapor mixing ratios

q_c is the parcel's cloud water mixing ratio

q_r is the parcel's rain water mixing ratio.

Allowing the left hand side of equation (D-6) to represent the perturbation momentum per unit mass and substituting with equations (D-9) and (D-10), equation (D6) becomes:

$$\frac{D\vec{V}}{Dt} = -c_p\overline{\theta}_v\vec{\nabla}\pi' + B\hat{k} \qquad \text{(D-11)}$$

To determine what factors influence the persistence and the propagation of the updraft, we evaluate equation (D-11) further. Using the anelastic continuity equation $\vec{\nabla}\bullet\overline{\rho}\vec{V} = 0$, we are encouraged to equalize (D-11) with $\overline{\rho}$ and take the divergence of the function.

$$\overline{\rho}\frac{D\vec{V}}{Dt} = -c_p\overline{\rho}\overline{\theta}_v\vec{\nabla}\pi' + \overline{\rho}B\hat{k}$$

$$\vec{\nabla}\bullet\overline{\rho}\frac{D\vec{V}}{Dt} = -\vec{\nabla}\bullet c_p\overline{\rho}\overline{\theta}_v\vec{\nabla}\pi' + \vec{\nabla}\bullet\overline{\rho}B\hat{k}$$

$$\vec{\nabla}\bullet\overline{\rho}\frac{\partial\vec{V}}{\partial t} + \vec{\nabla}\bullet\left(\overline{\rho}\vec{V}\bullet\vec{\nabla}\vec{V}\right) = -\vec{\nabla}\bullet c_p\overline{\rho}\overline{\theta}_v\vec{\nabla}\pi' + \frac{\partial\overline{\rho}B}{\partial z}$$

Solving for the diagnostic pressure term:

$$\vec{\nabla} \bullet c_p \overline{\rho} \overline{\theta}_v \vec{\nabla} \pi' = -\vec{\nabla} \bullet \overline{\rho} \frac{\partial \vec{V}}{\partial t} - \vec{\nabla} \bullet \left(\overline{\rho} \vec{V} \bullet \vec{\nabla} \vec{V} \right) + \frac{\partial \overline{\rho} B}{\partial z}$$

The first term on the right hand side is eliminated by the anelastic continuity assumption.

$$-\vec{\nabla} \bullet \overline{\rho} \frac{\partial \vec{V}}{\partial t} = -\vec{\nabla} \bullet \frac{\partial \left(\overline{\rho} \vec{V} \right)}{\partial t} = -\frac{\partial}{\partial t} \left(\vec{\nabla} \bullet \overline{\rho} \vec{V} \right) = 0$$

This results in the diagnostic pressure equation:

$$\vec{\nabla} \bullet c_p \overline{\rho} \overline{\theta}_v \vec{\nabla} \pi' = -\vec{\nabla} \bullet \left(\overline{\rho} \vec{V} \bullet \vec{\nabla} \vec{V} \right) + \frac{\partial \overline{\rho} B}{\partial z} \qquad \text{(D-12)}$$

Following the method of Rotunno and Klemp (1982), the diagnostic pressure may be represented in two components: pressure due to dynamics and pressure due to buoyancy gradients. Letting $\pi' = \pi_d + \pi_b$, we obtain the two equations

$$\begin{aligned} \vec{\nabla} \bullet c_p \overline{\rho} \overline{\theta}_v \vec{\nabla} \pi_d &= -\vec{\nabla} \bullet \left(\overline{\rho} \vec{V} \bullet \vec{\nabla} \vec{V} \right) \\ \vec{\nabla} \bullet c_p \overline{\rho} \overline{\theta}_v \vec{\nabla} \pi_b &= \frac{\partial \overline{\rho} B}{\partial z} \end{aligned} \qquad \text{(D-13)}$$

Equation (D-11)'s pressure term may also be similarly represented.

$$\frac{D\vec{V}}{Dt} = -c_p \overline{\theta}_v \vec{\nabla} \pi_d - c_p \overline{\theta}_v \vec{\nabla} \pi_b + B\hat{k}$$

Solving for the vertical component of the momentum equation and grouping buoyancy terms together, we obtain an equation which represents vertical wind component forcing due to a dynamic term and due to a buoyancy term.

$$\frac{dw}{dt} = -c_p \overline{\theta}_v \frac{\partial \pi_d}{\partial z} - \left(c_p \overline{\theta}_v \frac{\partial \pi_b}{\partial z} - B \right) \qquad \text{(D-14)}$$

Volume fields of the forcing terms were calculated using the method of Rotunno and Klemp (1982) by solving equations (D-13) using a fast Fourier transformation of the model pressure fields with periodic horizontal boundary conditions. The derivative on the lhs of (D-14) represents the Lagrangian, or parcel-following, development of the vertical wind component. To get a qualitative picture of how each term on the rhs of (D-14) contributes to updraft intensity, parcel trajectories were calculated within the updraft. The terms on the rhs of (D-14) were then integrated in time along each trajectory. It is assumed that the vertical wind component anywhere in the model domain can be represented by the time

integrated quantities of the forcing terms in (D-14) along the trajectory to the point being analyzed. The initial vertical wind speed for a parcel entering an updraft is assumed to be zero. The end result is the following equation:

$$w \approx \underbrace{-\int_{path} c_p \overline{\theta}_v \frac{\partial \pi_d}{\partial z} Dt}_{dynamic} \underbrace{-\int_{path} \left(c_p \overline{\theta}_v \frac{\partial \pi_b}{\partial z} - B \right) Dt}_{buoyancy} \qquad \text{(D-15)}$$

APPENDIX E

DISCUSSION OF THE PRODUCTION OF LOW-LEVEL ROTATION

To understand how horizontal vorticity is generated, we start with the equation of motion for an inviscid flow without planetary scale forcing.

$$\frac{d\vec{V}}{dt} = \frac{\partial \vec{V}}{\partial t} + \vec{V} \bullet \vec{\nabla}\vec{V} = -\frac{1}{\rho}\vec{\nabla}p \tag{E-1}$$

Following Dutton (1976), solve for the local tendency and take the curl of the function.

$$\vec{\nabla} \times \frac{\partial \vec{V}}{\partial t} = -\vec{\nabla} \times \left(\vec{V} \bullet \vec{\nabla}\vec{V}\right) - \vec{\nabla} \times \left(\frac{1}{\rho}\vec{\nabla}p\right) \tag{E-2}$$

Using the vector identity: $\vec{\nabla}\left(\vec{V} \bullet \vec{V}\right) = \left(\vec{V} \bullet \vec{\nabla}\right)\vec{V} + \left(\vec{V} \bullet \vec{\nabla}\right)\vec{V} + \vec{V} \times \left(\vec{\nabla} \times \vec{V}\right) + \vec{V} \times \left(\vec{\nabla} \times \vec{V}\right)$,

we find that $\vec{V} \bullet \vec{\nabla}\vec{V} = \vec{\nabla}\left(\frac{\left|\vec{V}\right|^2}{2}\right) - \vec{V} \times \left(\vec{\nabla} \times \vec{V}\right)$.

Since the vorticity vector $\vec{\omega}$ is defined by $\vec{\omega} = \vec{\nabla} \times \vec{V}$, equation (E-2) becomes:

$$\frac{\partial \vec{\omega}}{\partial t} = -\vec{\nabla} \times \left[\vec{\nabla}\left(\frac{\left|\vec{V}\right|^2}{2}\right)\right] - \vec{\nabla} \times \left(\vec{V} \times \vec{\omega}\right) - \vec{\nabla} \times \left(\frac{1}{\rho}\vec{\nabla}p\right) \tag{E-3}$$

The first term on the right hand side of (E-3) vanishes due to the identity $\vec{\nabla} \times \vec{\nabla}\Theta = 0$ whenever Θ is a scalar variable.

$$\frac{\partial \vec{\omega}}{\partial t} = -\vec{\nabla} \times \left(\vec{V} \times \vec{\omega}\right) - \vec{\nabla} \times \left(\frac{1}{\rho}\vec{\nabla}p\right) \tag{E-4}$$

Using the same identity, we find that

$$\begin{aligned} -\vec{\nabla} \times \left(\frac{1}{\rho}\vec{\nabla}p\right) &= -\frac{1}{\rho}\vec{\nabla} \times \vec{\nabla}p - \vec{\nabla}\frac{1}{\rho} \times \vec{\nabla}p \\ -\vec{\nabla} \times \left(\frac{1}{\rho}\vec{\nabla}p\right) &= -\vec{\nabla}\frac{1}{\rho} \times \vec{\nabla}p \end{aligned} \tag{E-5}$$

Substituting (E-5) into (E-4) yields:

$$\frac{\partial \vec{\omega}}{\partial t} = -\vec{\nabla} \times \left(\vec{V} \times \vec{\omega}\right) - \vec{\nabla}\frac{1}{\rho} \times \vec{\nabla}p \tag{E-6}$$

We next apply the vector identity:

$$\vec{\nabla}\times\left(\vec{V}\times\vec{\omega}\right)=\vec{V}\left(\vec{\nabla}\bullet\vec{\omega}\right)+\left(\vec{\omega}\bullet\vec{\nabla}\right)\vec{V}-\vec{\omega}\left(\vec{\nabla}\bullet\vec{V}\right)-\left(\vec{V}\bullet\vec{\nabla}\right)\vec{\omega} \qquad \text{(E-7)}$$

The first term on the right hand side of (E-7) vanishes because $\vec{\nabla}\bullet\vec{\omega}=\vec{\nabla}\bullet\left(\vec{\nabla}\times V\right)=0$.

Substituting (E-7) into (E-6) yields:

$$\frac{d\vec{\omega}}{dt}=\left(\vec{\omega}\bullet\vec{\nabla}\right)\vec{V}-\vec{\omega}\left(\vec{\nabla}\bullet\vec{V}\right)-\vec{\nabla}\frac{1}{\rho}\times\vec{\nabla}p \qquad \text{(E-8)}$$

Equation (E-8) indicates that vorticity is changed by 3 forcing terms:

1. stretching and tilting of preexisting vorticity
2. convergence or divergence of preexisting vorticity, and
3. baroclinicity.

If we assume anelastic continuity, $\vec{\nabla}\bullet\bar{\rho}\vec{V}=0$, the second term on the right hand side of (E-8) vanishes and the equation may be rewritten.

$$\frac{1}{\alpha}\frac{d(\alpha\vec{\omega})}{dt}=\left(\vec{\omega}\bullet\vec{\nabla}\right)\vec{V}+\vec{\nabla}p\times\vec{\nabla}\alpha \qquad \text{where} \quad \alpha=\frac{1}{\rho}. \qquad \text{(E-9)}$$

Next, we have the identity:

$$\vec{\omega}\bullet\frac{d}{dt}\vec{\nabla}\Theta=\vec{\omega}\bullet\vec{\nabla}\frac{d\Theta}{dt}-\vec{\nabla}\Theta\bullet\left[\left(\vec{\omega}\bullet\vec{\nabla}\right)\vec{V}\right] \qquad \text{(E-10)}$$

Where Θ is any useful scalar variable. This encourages multiplying (E-9) by $\alpha\vec{\nabla}\Theta$

$$\alpha\vec{\nabla}\Theta\bullet\left(\frac{1}{\alpha}\frac{d(\alpha\vec{\omega})}{dt}\right)-\alpha\vec{\nabla}\Theta\bullet\left[\left(\vec{\omega}\bullet\vec{\nabla}\right)\vec{V}\right]=\alpha\vec{\nabla}\Theta\bullet\left(\vec{\nabla}p\times\vec{\nabla}\alpha\right) \qquad \text{(E-11)}$$

Using the identity in (E-10), equation (E-11) may be rewritten as:

$$\vec{\nabla}\Theta\bullet\left(\frac{d(\alpha\vec{\omega})}{dt}\right)+\alpha\vec{\omega}\bullet\frac{d}{dt}\vec{\nabla}\Theta-\alpha\vec{\omega}\bullet\vec{\nabla}\frac{d\Theta}{dt}=\alpha\vec{\nabla}\Theta\bullet\left(\vec{\nabla}p\times\vec{\nabla}\alpha\right) \text{ or}$$

$$\frac{d}{dt}\left(\vec{\nabla}\Theta\alpha\vec{\omega}\right)-\alpha\vec{\omega}\bullet\vec{\nabla}\frac{d\Theta}{dt}=\alpha\vec{\nabla}\Theta\bullet\left(\vec{\nabla}p\times\vec{\nabla}\alpha\right)$$

To simplify the analysis, Θ is selected such that it is conserved. The scalar field chosen for this is equivalent potential temperature θ_e because it is a quantity which is conserved in both dry adiabatic and moist adiabatic processes. The equivalent potential temperature is the temperature a parcel would have if it were expanded and allowed to cool dry adiabatically until saturation, then cool moist adiabatically until all of the water vapor

has condensed and "fallen" out of the parcel, then compressed dry adiabatically to a reference pressure (Hess 1959).

$$\frac{d}{dt}\left(\vec{\nabla}\theta_e \alpha\vec{\omega}\right) - \alpha\vec{\omega} \bullet \vec{\nabla}\frac{d\theta_e}{dt} = \alpha\vec{\nabla}\theta_e \bullet \left(\vec{\nabla}p \times \vec{\nabla}\alpha\right) \tag{E-12}$$

If it is assumed that θ_e is conserved, the second term on the left hand side of (E-12) vanishes.

$$\frac{d}{dt}\left(\vec{\nabla}\theta_e \alpha\vec{\omega}\right) = \alpha\vec{\nabla}\theta_e \bullet \left(\vec{\nabla}p \times \vec{\nabla}\alpha\right) \tag{E-13}$$

The term $\vec{\nabla}p \times \vec{\nabla}\alpha$ may be approximated to $\vec{\nabla} \times B\hat{k}$ (as in the work of Rotunno and Klemp 1985) by the following method:

$$\vec{\nabla}p \times \vec{\nabla}\alpha = \begin{bmatrix} \hat{i}\left(\frac{\partial p}{\partial y}\frac{\partial \alpha}{\partial z} - \frac{\partial p}{\partial z}\frac{\partial \alpha}{\partial y}\right) + \\ \hat{j}\left(\frac{\partial p}{\partial z}\frac{\partial \alpha}{\partial x} - \frac{\partial p}{\partial x}\frac{\partial \alpha}{\partial z}\right) + \\ \hat{k}\left(\frac{\partial p}{\partial x}\frac{\partial \alpha}{\partial y} - \frac{\partial p}{\partial y}\frac{\partial \alpha}{\partial x}\right) \end{bmatrix} \tag{E-14}$$

If it is assumed that the gradient of the basic state pressure is hydrostatic then

$$\vec{\nabla}_h p = 0$$

$$\frac{\partial p}{\partial z} = -\frac{g}{\overline{\alpha}}$$

This simplifies equation (E-14) to

$$\vec{\nabla}p \times \vec{\nabla}\alpha = \begin{bmatrix} \hat{i}\left(\frac{g}{\overline{\alpha}}\frac{\partial \alpha}{\partial y}\right) + \\ \hat{j}\left(-\frac{g}{\overline{\alpha}}\frac{\partial \alpha}{\partial x}\right) + \\ \hat{k}(0) \end{bmatrix}$$

Ignoring the effects of water vapor and liquid water loading in the buoyancy function as we do in our consideration of the equivalent potential temperature, buoyancy may be expressed as: $B\hat{k} = \frac{g\alpha'}{\overline{\alpha}}$ resulting in

$$\vec{\nabla}p \times \vec{\nabla}\alpha = \begin{bmatrix} \hat{i}\left(\frac{\partial B}{\partial y}\right) + \\ \hat{j}\left(-\frac{\partial B}{\partial x}\right) + \\ \hat{k}(0) \end{bmatrix} = \vec{\nabla} \times B\hat{k} \qquad \text{(E-15)}$$

If it is assumed that θ_e depends only on the thermodynamic properties of the flow (ignoring supersaturation, turbulence, and water loading from cloud water and rain water), then $\theta_e = \theta_e(\alpha, p)$, or $\theta_e = \theta_e(B)$. This implies the following:

$$\vec{\nabla}\theta_e = \frac{\partial \theta_e}{\partial \alpha}\vec{\nabla}\alpha + \frac{\partial \theta_e}{\partial p}\vec{\nabla}p \text{ or } \vec{\nabla}\theta_e = \frac{d\theta_e}{dB}\vec{\nabla}B$$

and $$\overline{\alpha}\vec{\nabla}\theta_e \bullet \left(\vec{\nabla}p \times \vec{\nabla}\overline{\alpha}\right) = 0 \text{ or } \overline{\alpha}\vec{\nabla}\theta_e \bullet \left(\vec{\nabla} \times B\hat{k}\right) = 0$$

resulting in Ertel's Theorem for the conservation of equivalent potential vorticity.

$$\frac{d}{dt}\left(\vec{\nabla}\theta_e \overline{\alpha}\vec{\omega}\right) = 0 \qquad \text{(E-16)}$$

This theorem states that the horizontal vorticity on surfaces of constant θ_e will be conserved. Thus baroclinically generated horizontal vorticity arising as a result of horizontal density gradients such as between the cold pool beneath the downdraft of a storm and the warmer inflowing air will remain nearly confined to surfaces of constant θ_e even as those surfaces are being tilted by the updraft. Rotunno and Klemp (1985) indicated this is the mechanism through which strong low-level rotations develop near the updraft in mature supercells.

VITA

Louis Edward Cantrell, Jr. is a career military officer in the United States Air Force. He began his military career in 1986 as an enlisted Engineering Assistant Specialist with the 820th REDHORSE Civil Engineering Squadron at Nellis AFB, NV. He was subsequently awarded a full active duty scholarship through the Airman Education and Commissioning Program (AECP) to complete his undergraduate degree at Texas A&M University in 1988. He graduated Cum Laude in December 1990 with a Bachelor of Science degree in Meteorology, and was inducted into the Meteorological National Honor Society.

Capt Cantrell was subsequently commissioned as a reserve officer following Officer Training School at Lackland AFB, TX in June 1991. As a weather officer, Capt Cantrell supported the headquarters, Special Operations Command, and the 54th Wing at MacDill AFB, FL by providing flight weather briefings and operations planning support until June 1992. He then provided staff level weather support to 7 AF, Osan AB, Republic of Korea through 1993.

In 1993, Capt Cantrell was accepted again for another full active duty scholarship to obtain his graduate degree at Texas A&M University. While a student at Texas A&M, he participated in the VORTEX '94 Field Experiment in Norman, OK in conjunction with the National Severe Storms Laboratory and other universities as part of a camera team tasked with obtaining film footage of tornadoes for photo-stereogrametry analysis. He also assisted Dr. Louis J. Wicker, Associate Professor of Meteorology at Texas A&M, in preparing a conference paper on a low-topped tornadic supercell event for the *18th Conference on Severe Local Storms.* Capt Cantrell graduated from Texas A&M in August 1995 with a Master of Science degree in Meteorology and was assigned to Air Force Global Weather Central at Offutt AFB, NE at the time of this publication.

Capt Cantrell's permanent address is 4233 11th Avenue North, St. Petersburg, Florida 33713. (813) 323-7433.